70-14,596

McMASTER, Ronald Ashley, 1939-
LOCAL HEAT TRANSFER FOR FLOW IN A RADIAL DIFFUSER.

The University of Michigan, Ph.D., 1969
Engineering, mechanical

University Microfilms, Inc., Ann Arbor, Michigan

THIS DISSERTATION HAS BEEN MICROFILMED EXACTLY AS RECEIVED

LOCAL HEAT TRANSFER FOR FLOW IN A RADIAL DIFFUSER

Ronald Ashley McMaster

A dissertation submitted in partial fulfillment
of the requirements for the degree of
Doctor of Philosophy in
The University of Michigan
1969

Doctoral Committee:

Associate Professor Paul S. Larsen, Chairman
Professor Vedat S. Arpaci
Professor John A. Clark
Professor Walter R. Debler
Associate Professor Robert B. Keller
Associate Professor George S. Springer

To my Father and Mother

ACKNOWLEDGMENTS

I wish to express my sincere gratitude to Professor Paul S. Larsen for his guidance and encouragement during this research. I also wish to thank Professors V. S. Arpaci, J. A. Clark, W. R. Debler, R. B. Keller, and G. S. Springer for their interest and cooperation at various stages of the research.

The support of Permaglass, Inc., Millbury, Ohio during the experimental research is gratefully acknowledged.

Finally, I wish to thank my wife for her patience, sacrifices, and encouragement.

TABLE OF CONTENTS

	Page
LIST OF FIGURES	vi
LIST OF TABLES	viii
LIST OF APPENDICES	ix
NOMENCLATURE	x
ABSTRACT	xiv
I INTRODUCTION AND LITERATURE SURVEY	1
A. Introduction	1
B. Literature Survey	4
1. Flow Investigations	4
2. Heat Transfer Investigations	12
II THEORETICAL ANALYSIS	15
A. Problem Statement	15
B. Velocity Field	16
1. Introduction	16
2. General Differential Formulation	18
3. One-Parameter Case	20
a. Formulation	20
i. Approximating Function	20
ii. Governing Equation	21
iii. Boundary Conditions	24
b. Perturbation Solution	25
c. Numerical Solution	26
d. Pressure Field	28
e. Discussion of Results	29
4. Two-Parameter Case	34
a. Formulation	36
i. Approximating Function	36
ii. Governing Equation	40
iii. Boundary Conditions	40
b. Numerical Solution and Discussion of Results.	41
C. Thermal Field	45
1. Introduction	45

TABLE OF CONTENTS (CONT'D)

		Page
2.	General Differential Formulation	47
3.	Stagnation Point	47
a.	Formulation	47
i.	Governing Equation and Boundary Conditions	47
ii.	Approximating Function	48
b.	Solution and Discussion of Results	49
4.	Stagnation Region	51
5.	Diffuser Region	52
a.	Formulation	52
i.	Governing Equations and Boundary Conditions	52
ii.	Approximating Functions	53
b.	Solution and Discussion of Results	53
III	EXPERIMENTAL INVESTIGATION	59
A.	Introduction	59
B.	Flow	59
1.	Apparatus	59
2.	Procedure	62
3.	Property Evaluation and Data Reduction	62
4.	Results and Comparison with Theoretical Analysis	63
5.	Experimental Uncertainty	66
C.	Heat Transfer	67
1.	Apparatus	67
2.	Procedure	74
3.	Property Evaluation and Data Reduction	75
4.	Results and Comparison with Analysis	76
a.	Stagnation Point	76
b.	Stagnation Region	83
c.	Diffuser Region	86
d.	Average	91
5.	Experimental Uncertainty	98
IV	SUMMARY OF RESULTS	100
APPENDICES		104
BIBLIOGRAPHY		122

LIST OF FIGURES

Figure		Page
1-1	Geometric Configuration of Radial Diffuser.....	2
1-2	Flow Field in Radial Diffuser.....	5
1-3	Heat Transfer Distributions in Two-Dimensional Stagnation Region.....	14
2-1	Analytical Model of Flow Field in Radial Diffuser.....	17
2-2	One-Parameter Velocity Distributions.....	22
2-3	Radial Variation of Free Parameter.....	27
2-4	Radial Variation of Average Primary Flow Rate.....	32
2-5	Radial Variation of Ratio of Average Primary Flow Rate to Average Flow Rate.....	33
2-6	Radial Pressure Distributions.....	35
2-7	Function H_1 (η).....	37
2-8	Function H_2 (η).....	37
2-9	Separation Velocity Profiles, Two-Parameter Case.....	39
2-10	Symmetric Velocity Profiles, Two-Parameter Case.....	39
2-11	Two Parameter Coordinate System.....	42
2-12	Two Parameter Flow Map.....	44
2-13	Configuration of Thermal Field.....	46
2-14	Thermal Boundary Layer Growth.....	56
2-15	Thermal Boundary Layer Growth.....	57
3-1	Schematic of Flow Apparatus.....	60
3-2	Schematic of Smoke Generator.....	61
3-3	Primary Reattachment Radius vs Diffuser Reynolds Number.	64
3-4	Primary Vortex Thickness vs Diffuser Reynolds Number....	65

LIST OF FIGURES (CONT'D)

Figure		Page
3-5	Schematic of Heat Transfer Apparatus.....	68
3-6	Photograph of Heat Transfer Apparatus.....	69
3-7	Detail Drawing of Test Section.....	70
3-8	Photograph of Test Section.....	72
3-9	Heat Flux Distributions.....	77
3-10	Heat Flux Distributions.....	78
3-11	Heat Flux Distributions.....	79
3-12	Stagnation Point Heat Transfer Rate vs Inlet Reynolds Number.....	81
3-13	Stagnation Point Heat Transfer Rate vs Centerline Inlet Reynolds Number.....	84
3-14	Stagnation Point Heat Transfer Rate vs Area Ratio.....	85
3-15	Heat Flux Distributions.....	88
3-16	Position of Local Minimum in Heat Transfer Rate vs Inlet Reynolds Number.....	89
3-17	Heat Transfer Rate Distributions.....	90
3-18	Average Heat Transfer Rate vs Inlet Reynolds Number.....	92
3-19	Average Heat Transfer Rate vs Diffuser Reynolds Number..	96
3-20	Average Heat Transfer Rate vs Centerline Diffuser Reynolds Number.....	97
A-1	Derivatives of Free Parameter at Inlet Radius.....	109
A-2	Physical and Conformal Mapping Planes.....	116
A-3	Free Stream Velocity Distribution in Stagnation Region..	119
A-4	Stagnation Point Velocity Gradient vs Area Ratio.....	120
A-5	Ratio G/σ vs Area Ratio.....	120

LIST OF TABLES

Table		Page
1-1	Summary of Experimentally Observed Flow Regimes.....	9
1-2	Asymptotic Solutions for Radial Pressure Distribution...	10
3-1	Test Section Components.....	71
3-2	Experimental Data.....	80

LIST OF APPENDICES

Appendix		Page
I	COORDINATE PERTURBATION SOLUTION OF EQUATION (2-2-a) FAR DOWNSTREAM.....	105
II	COORDINATE PERTURBATION SOLUTION OF EQUATION (2-6-a) NEAR THE INLET RADIUS.....	107
III	RELATIONSHIP BETWEEN SEPARATION STREAMLINE AND FREE PARAMETERS.....	110
IV	INVICID FLOW IN A TWO-DIMENSIONAL ENCLOSED CORNER..	112

NOMENCLATURE

The following list of symbols defines all terms used in this thesis except for APPENDIX IV which has its own nomenclature. This method ensures the simplicity and clarity of the symbology because the symbols used in APPENDIX IV usually have a different meaning from those used elsewhere in the report.

Roman

c	specific heat of fluid
$\mathcal{B}$	boundary layer thickness ratio, δ/δ_T
e	heat flux transducer voltage
E	free parameter defined in Equation (2-43)
F	free parameter defined in Equation (2-4)
F_n	free parameters defined in Equations (2-18)
g	stagnation point velocity gradient
G	dimensionless stagnation point velocity gradient, $gR_o/\overline{U}_{R_o}$
h	heat transfer coefficient, q/T
H_n	functions defined in Equations (2-4) and (2-18)
k	thermal conductivity
K	constant, Equation (1-4)
L	side dimension, Equation (3-4)
M	constant, Equation (1-4)
N	constant, Equation (1-4)
Nu	Nusselt number, $\dot{q}^2 R_o/k\,\Delta T$
Nu_{Z_o}	Nusselt number, $\dot{q}Z_o/k\,\Delta T$
p	pressure

p_o	atmospheric pressure
P	length of primary vortex, Figure I-2
Pe	Péclèt number, $R_{R_o}Pr$
Pr	Prandtl number, $\mu c/k$
$\mathcal{P}$	dimensionless pressure, $p/\rho \bar{U}_{R_o}^2$
$\dot{q}$	heat transfer rate, $-k\left(\frac{\partial T}{\partial z}\right)_{z=0}$
r	radial position
R_o	inside radius
R_1	outside radius
R_{PR}	primary reattachment radius
R_{R_o}	diffuser Reynolds number, $\rho \bar{U}_{R_o} Z_o \sigma/\mu$
$R_{R_o,\ell}$	centerline diffuser Reynolds number, $Re_\ell \sigma/4$
Re	inlet Reynolds number, $\rho \bar{U}_{Z_o} 2R_o/\mu$
Re_ℓ	centerline inlet Reynolds number, $\rho v_\ell 2R_o/\mu$
Re_r	local Reynolds number, $\rho \dot{V}/\pi \mu r$
Re_T	transition Reynolds number, Equation (I-2)
S	length of secondary vortex, Figure I-2
t	thickness of primary vortex, $1-z_p$
T	temperature
T_o	temperature of inflowing fluid
T_1	temperature of lower surface
T_f	film temperature, $T_o+T_1/2$
ΔT	temperature difference, T_1-T_o
u	radial velocity
U	free stream velocity
$\bar{U}_p$	average velocity of primary flow
$\bar{U}_{R_o}$	average flow rate at entrance to diffuser region, $\dot{V}/2\pi R_o Z_o$

$\bar{U}_{Z_o}$	average inlet flow rate, $\dot{V}/\pi R_o^2$
u	dimensionless radial velocity, $u/\bar{U}_{R_o}$
U	dimensionless free stream velocity, $U/\bar{U}_{R_o}$
v	axial velocity
v_c	centerline velocity
$\dot{V}$	volume flow rate
z	axial coordinate
z_p	axial position of separation streamline
Z_o	separation between surfaces

Greek

α	thermal diffusivity, $k/\rho c$
Γ	dimensionless primary vortex thickness, t/Z_o
δ	viscous boundary layer thickness
δ_T	thermal boundary layer thickness
ϵ	perturbation parameter
ξ	transformed dimensionless radius, ξ^2
η	dimensionless axial position, Z/Z_o
η_T	dimensionless thermal boundary layer thickness, δ_T/Z_o
η_v	dimensionless viscous boundary layer thickness, δ/Z_o
θ	dimensionless temperature, $T-T_o/T_i-T_o$
Λ	shape parameter, $\frac{1}{2} R_{R_o} \eta_v^2 \frac{dU}{d\xi}$
μ	viscosity
ξ	dimensionless radius, r/R_o
ρ	density
σ	area ratio, $2Z_o/R_o$
τ	axial position ratio, Z/δ_T
ν	axial position ratio, Z/δ

ϕ	function defined in Equation (2-11-b)
Ψ	dimensionless stream function, $2\pi\psi/\dot{V}$
ψ	stream function

Subscripts

$( )_s$	stagnation point value

Superscripts

$\bar{( )}$	average value

ABSTRACT

Flow and heat transfer characteristics of an incompressible fluid in a radial diffuser are investigated analytically and experimentally. A steady, axisymmetric, swirl-free flow is considered which issues axially from a circular hole in one of two closely spaced stationary surfaces, impinges upon the other surface and flows radially outward. The latter surface is maintained at a uniform temperature above that of the incoming fluid while the former surface is insulated. The pertinent dimensionless parameters are the inlet Reynolds number, $Re = \rho \bar{u}_{z_o} 2R_o/\mu$, the ratio of the stagnation region exit to inlet area or area ratio, $\sigma = 2z_o/R_o$, the diffuser Reynolds number, $R_{R_o} = \sigma Re/4$, and the Prandtl number, $Pr = \mu c/k$.

The analysis is confined to laminar flow and area ratios less than 1, for which velocity and temperature fields are derived by integral techniques. The flow field includes a primary vortex which extends downstream from the sharp inlet corner. The minimum diffuser Reynolds number required for a primary vortex to exist is predicted along with the subsequent growth in length and thickness of the vortex as the diffuser Reynolds number increases. The radial pressure distribution is derived and is an improvement over similar distributions which do not consider the effect of the primary vortex. The heat transfer from the lower surface at the stagnation point and in the diffuser region is predicted. The latter, however, is based on an experimentally determined value at the entrance to the diffusor region since the solution in the stagnation region was not considered.

The flow field is investigated experimentally using air as the fluid. Inlet Reynolds numbers ranged from 193 to 1422 and area ratios from .75 to 1.88. The inception and subsequent growth of the primary vortex with increasing diffuser Reynolds number is determined by flow visualization using smoke filaments and substantially agrees with the analytical solution for the flow field.

The experimental heat transfer investigation is carried out with air as the fluid. Inlet Reynolds numbers ranged from 15 to 53,500 and area ratios from .245 to 2.04. The outside diameter was 8.7 times the inside diameter. Measured heat transfer rates at the stagnation point for laminar and turbulent flows and in the diffuser region for laminar flow are adequately described analytically. Experimental heat transfer rate distributions are presented for both laminar and turbulent flows over an inlet Reynolds number range of 115 to 7700. Correlations for the average heat transfer rates determined from experimental heat transfer distributions are presented for inlet Reynolds numbers from 115 to 53,000.

CHAPTER I

INTRODUCTION AND LITERATURE SURVEY

A. Introduction

The objective of the present study is the analysis of the convective heat transfer associated with the steady laminar axisymmetric swirlfree flow of an incompressible fluid in a radial diffuser. The geometric configuration of the radial diffuser is shown in Figure I-1. It consists of two flat coaxial disk shaped surfaces of radius R_I separated by a distance Z_O. The flow is introduced by an inlet tube of radius R_O which is coaxial with and joined to the upper surface forming a well defined sharp edged corner. The lower surface is maintained at a temperature which exceeds that of the incoming fluid. The upper surface is insulated. The main interest is the determination of the velocity field and the local convective heat transfer rate from the lower surface. Knowledge of the latter has important applications in heating and tempering glass, hydrostatic bearing design, and heat exchanger design. Both experimental and theoretical analyses are performed.

In subsequent discussions it is convenient to consider the radial diffuser shown in Figure I-1 to consist of three regions: I - inlet, II - stagnation, and III - diffuser. The flow in the inlet region is an axisymmetric pipe flow which may be laminar, transitional, or turbulent. The flow is turned to the radial direction in the stagnation region. An axisymmetric stagnation point occurs at the center of the lower surface. The flow and heat transfer in the diffuser

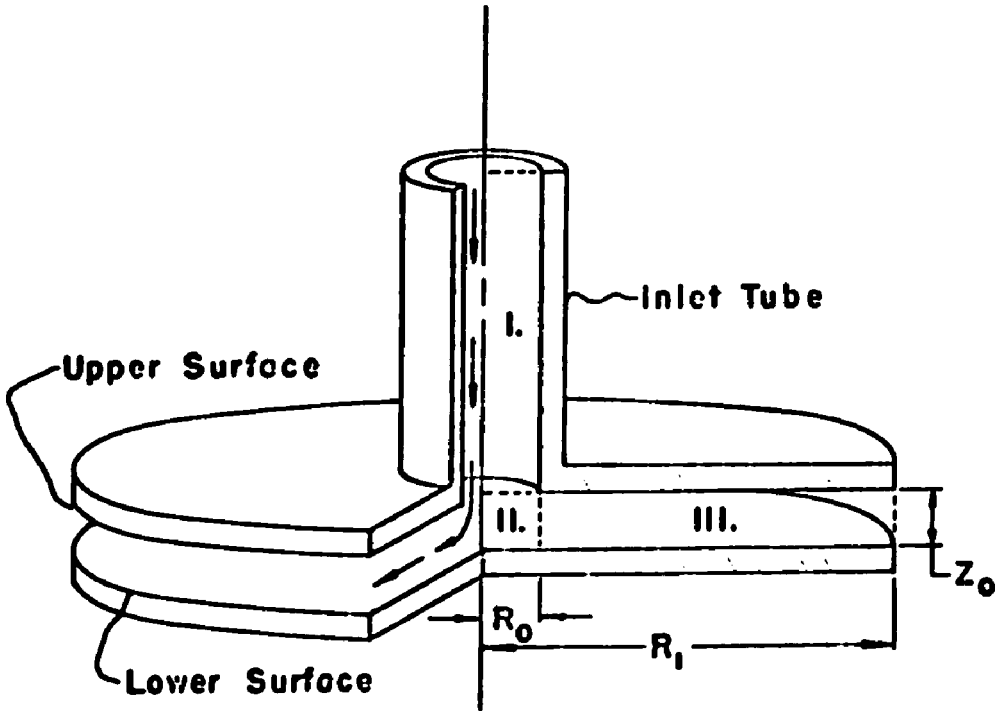


Figure I-1. Geometric Configuration of Radial Diffuser.

region near the inlet radius are influenced considerably by the preceding inlet and stagnation regions. The inertia of the incoming flow, being axially directed, causes the flow entering the stagnation region to continue in an axial direction thus promoting separation at the inlet corner when the flow rate is sufficiently high. The flow subsequently reattaches to the upper surface downstream in the diffuser region because the close spacing of the surfaces causes the flow to become predominantly radially directed. An annular secondary flow of recirculating fluid, hereafter referred to as a primary vortex, forms between the separation and reattachment points. The formation of the primary vortex profoundly affects the flow field in the diffuser region and, consequently, the convective heat transfer from the lower surface. The velocity and temperature fields in the stagnation region, while outwardly similar to those for an axisymmetric Hiemenz flow, are significantly dependent on the ratio of the stagnation region outflow and inflow areas, hereafter referred to as the area ratio. The free stream velocity along the lower surface accelerates or decelerates from the stagnation point when the area ratio is less or greater than unity, respectively. Consequently, the associated viscous and thermal boundary layers diminish and grow in thickness from the stagnation point, respectively.

In the stagnation region the dimensionless flow parameter is the inlet Reynolds number, $Re = \rho \bar{u}_{z_o} 2R_o/\mu$, based on the average inlet flow rate, $\bar{u}_{z_o} = \dot{V}/\pi R_o^2$, and the inlet diameter, $2R_o$. The dimensionless geometric parameter is the area ratio, σ = (outflow area/inflow area)$_{\text{stagnation region}} = 2Z_o/R_o$ In the diffuser region the dimensionless flow and geometric parameters are combined in the diffuser Reynolds number, $R_{R_o} = \rho \bar{u}_{R_o} Z_o \sigma/\mu$, based on the average

diffuser inlet flow rate, $\bar{u}_{R_o} = \dot{V}/2\pi R_o Z_o$, and the surface separation, Z_o. The diffuser Reynolds number is conveniently expressed in terms of the inlet Reynolds number as $R_{R_o} = \sigma Re/4$. The area ratio is of secondary importance in the diffuser region. The dimensionless parameters associated with the heat transfer are the Prandtl number, $Pr = \mu c/k$, and the Nusselt number based on the inlet diameter, $Nu = 2R_o\dot{q}/k\Delta T$, where $\dot{q}$ is the heat transfer rate and ΔT is the temperature difference between the lower surface and the incoming fluid.

B. Literature Survey

The local heat transfer rate from a surface by forced convection depends on the neighboring velocity field, consequently, a survey of the literature concerned with the fluid mechanics of the flow in a radial diffuser is presented first. A conceptual idea of the physics of the flow is drawn from several experimental studies. A survey of the heat transfer literature then follows.

1. Flow Investigations

The flow characteristics in the diffuser region as the flow rate increases are shown in Figure 1-2 from McGinn [33] for a constant area ratio using water as the fluid. These drawings were made from photographs. The nature of the flow field was made visible by introducing dye filaments along the upper and lower surfaces and in the main stream. Except for very low flow rates, the boundary filaments thicken over the distances P and S on the upper and lower surfaces respectively and the free stream filament deflects considerably. As the flow rate increases the boundary filaments indicate that separated regions consisting of annular vortices of trapped fluid form near both surfaces. The primary vortex extends from the inlet corner, where flow

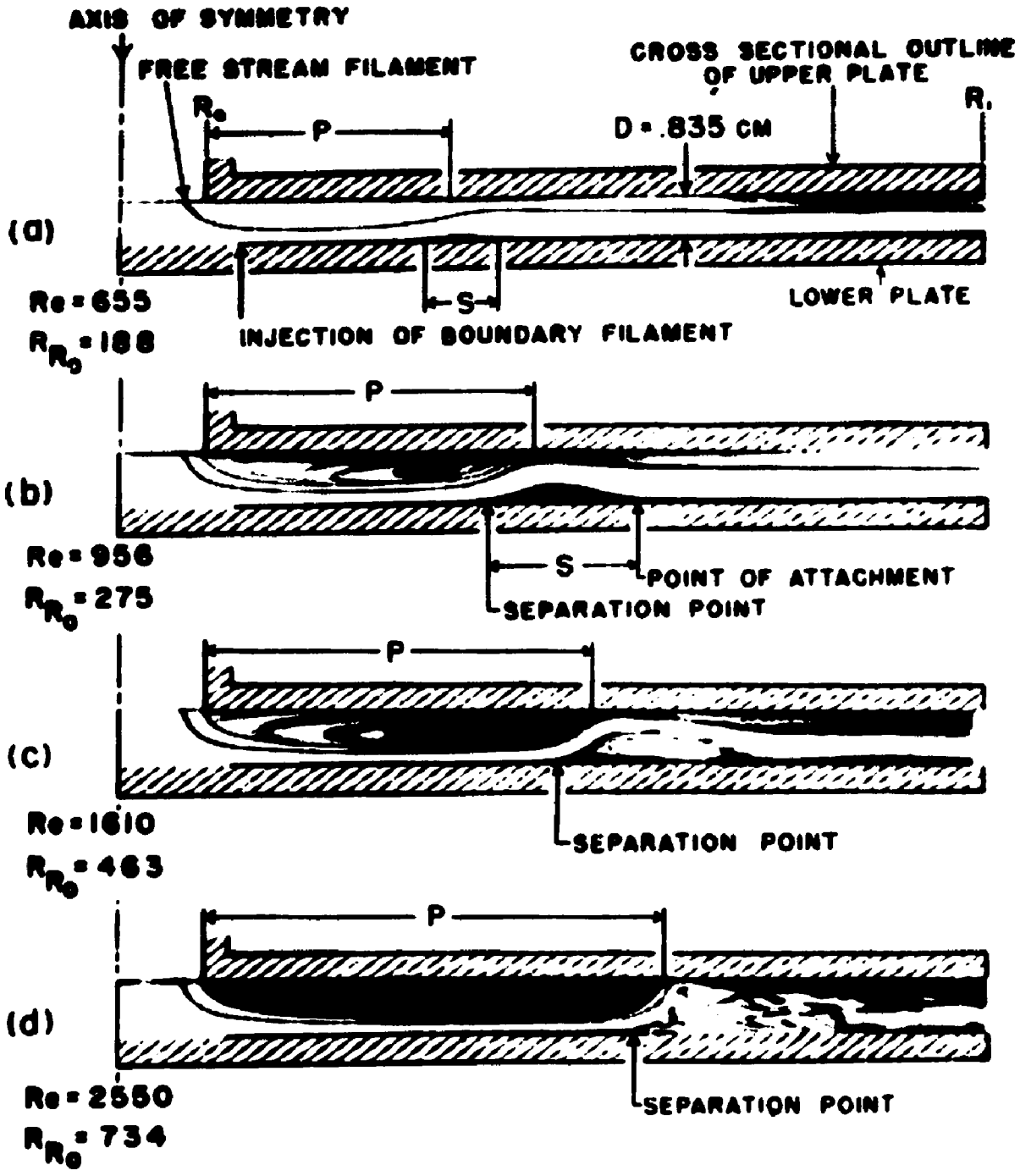


Figure -2. Flow Field in Radial Diffuser.

separation occurs, a distance P, whereupon the flow reattaches. Slightly upstream of the primary reattachment point the flow separates from the lower surface and a secondary vortex forms which extends a distance S downstream whereupon the flow reattaches. As the flow rate increases both vortices grow in length and thickness. The secondary vortex moves downstream with the primary reattachment point. At a flow rate intermediate to those of Figures I-2-b and I-2-c disturbances develop which propagate downstream over the vortices. These disturbances tend to damp out until, as shown in Figure I-2-c, the secondary vortex fails to reattach. The flow downstream of the secondary separation point remains laminar, however, until the flow rate reaches the level shown in Figure I-2-d. At this point the flow downstream of the secondary separation point becomes turbulent. Thus, even though the flow upstream of the secondary separation point is laminar the flow downstream is turbulent. As the flow rate is increased further the incoming flow becomes turbulent and the primary vortex diminishes considerably in length. Retransition should occur if the outside radius is large enough because the average flow rate decreases with increasing radius.

The minimum diffuser Reynolds number required to produce a primary vortex has been investigated theoretically by McGinn [33] based on the compatibility condition that no flow separation should occur as long as the radial pressure distribution monotonically decreases. Using this criterion and the pressure distribution from Equation (I-4) and Table I-2 given below, McGinn predicts that a primary vortex exists when

$$R_{R_o} \geq 15.5 \qquad \text{(I-1-a)}$$

which was experimented verified with a limited amount of data from a radial diffuser with a sharp inlet corner. Pressure distribution data taken by Hagiwara [18] with a sharp inlet corner agreed with theory for a diffuser Reynolds number of 15.8 but not for 94.2. With a rounded inlet corner his experimental data agreed with the theoretical distribution for diffuser Reynolds number up to at least 129. No data was presented for higher flow rates. The primary vortex evidently forms for a diffuser Reynolds number in the range

$$15.8 < R_{R_o} < 94.2 \qquad (1\text{-}1\text{-}b)$$

Similarly, a comparison of Moller's [35] experimental pressure distributions with sharp and rounded inlet corners indicates that a primary vortex occurs when

$$R_{R_o} \geq 21.6 \qquad (1\text{-}1\text{-}c)$$

McGinn [32] found empirically that the inlet Reynolds number required for transition to turbulent flow in the diffuser region is linearly related to the area ratio according to the equation

$$Re_T = 2000(1 - .424\sigma) \qquad (1\text{-}2)$$

The phenomenon of reverse transition has been investigated by Moller [35], Comolet [7], Peube [40], Chen and Peube [5], and Kreith [27]. Moller and Comolet experimentally determined that reverse transition occurred when the local Reynolds number

$$Re_r = \frac{\rho \dot{V}}{\pi \mu r}$$

reaches a critical value of 2000 and 1100, respectively. The discrepancy between the two values is probably a result of experimental conditions

which are known to strongly affect retransition. The local Reynolds number corresponds to a pipe Reynolds number based on the hydraulic diameter. The observed retransition Reynolds numbers compare favorably with those for pipe flows. For a retransition local Reynolds number of 2000 the diffuser Reynolds number required for no retransition is

$$R_{R_e} = 1000\sigma\left(\frac{R_i}{R_e}\right) \qquad (1\text{-}3)$$

Table I-1 sums up the different flow regimes which have been experimentally observed for incompressible flow in a radial diffuser. The diffuser Reynolds number range associated with each flow regime is listed although this correlation is necessarily sketchy because of insufficient data.

The preceding studies reveal a great deal about the qualitative nature of the flow in a radial diffuser. Quantitative information about the velocity field in the diffuser region is very difficult to determine experimentally because of the low flow rates associated with laminar flow and the small spacings commonly employed between the surfaces - typically 0.010 inch to 0.250 inch in most cases. Consequently most studies have dealt with the radial pressure distribution instead. The pressure is usually considered to be a function of the radial coordinate only since the axial pressure variation is negligible.

Most analytical studies of the radial pressure distribution are concerned with asymptotic solutions far downstream from the inlet radius since entrance conditions are ignored or considered to be negligible. The literature concerned with this area is voluminous and is summarized in Table I-2. Only studies concerned with the effect of inertia as well as viscosity are listed. Integral and perturbation

TABLE 1-1

SUMMARY OF EXPERIMENTALLY
OBSERVED FLOW REGIMES

References	Approximate Diffuser Reynold's Number Range	Flow Character	Laminar Vortices?		Reattachment?	
			Primary	Secondary	Primary	Secondary
1,8,2	$R_{R_e} < 15.5\text{-}60.0$	Laminar throughout	None	None	-	-
1	$15.5\text{-}60.0 < R_{R_e} < 500(1-.424\sigma)$	Laminar throughout	Yes	Yes	Yes	Yes
1	$R_{R_e} = 500(1-.424\sigma)$	Transition to turbulent flow downstream of secondary separation point	Yes	No	Yes	No
2,3,4,5,6	$500(1-.424\sigma) < R_{R_e} < 1000\left(\frac{R_i}{R_o}\right)\sigma$	Turbulent inflow, laminar outflow	No	*	*	*
1,2	$1000\left(\frac{R_i}{R_o}\right)\sigma \leq R_{R_e}$	Turbulent throughout	No	*	*	*

*No information available.

TABLE 1-2

ASYMPTOTIC SOLUTIONS FOR RADIAL PRESSURE DISTRIBUTION

Ref. No.	Nature of Laminar Flow: Incompressible	Nature of Laminar Flow: Compressible	Nature of Laminar Flow: Undeveloped	Nature of Laminar Flow: Developed	Assumed Velocity Field: Uniform	Assumed Velocity Field: Parabolic	Assumed Velocity Field: Power Series	Assumed ψ: Power Series	N-S Eq'n: Navier-Stokes type	N-S Eq'n: Complete	Constants in Eq. (1-4): K	Constants in Eq. (1-4): Z	Constants in Eq. (1-4): Z'	Experimental Results	Remarks
32	X			X		X			X		.500			X	Added individual solutions for vicid and invicid flows.
33	X			X		X			X		.772			X	Added individual solutions for vicid and invicid flows. Assumed parabolic profile in latter.
7		X		X		X			X		.600			X	Momentum integral solution.
30	X			X		X			X		.600				Momentum integral solution.
36														X	Attempt to verify Livesey [30] experimentally.
2	X		X					X			.671	1.42	.368		Perturbation solution of complete r-direction N-S equation in terms of r^{-2}. Third approximation.
19	X		X				X			X					Perturbation solution in terms of r^{-1}. Inertia effects found to be negligible in experimental work done on hydrostatic bearings.
37		X	X						X						Solution by separation of variables. Velocity distribution is in terms of elliptic functions.
8		X		X	X						.500				Complete r-direction N-S equation solved in terms of stream function.
		X		X		X					.600				
		X	X					X			.772				Perturbation solution of complete r-direction N-S equation in terms of r^{-2}. First approximation.
35	X		X						X		.720			X	Perturbed parabolic profile used for momentum integral solution.
40	X		X				X			X	.772	2.86	.904		Perturbation solution in terms of r^{-1}. Fifth order approximation.
15	X		X					X		X					Perturbation solution in terms of r^{-2}. Pressure distribution not found.
42	X		X					X		X	.772				Perturbation of viscous solution in terms of r^{-2}. First order approximation.
47	X		X					X		X	.772	2.86	.904	X	Perturbation solution in terms of r^{-2}.
22	X		X						X		.772	.00	.870	X	Solution by method of successive substitutions. Summarizes (30), (35), (42), and (23).
23	X		X				X		X		.772				Collocation solution at surface.
24											.772				Completion of analysis started by Hunt and Torbe [19].
19														X	Summarizes (33), (30), (35), and (40).
10	X			X		X			X		.772				Energy integral solution.

techniques are applied in a majority of the solutions. The resulting radial distributions have the general form

$$\bar{P}(\xi) - P_0 = \frac{24}{R_{R_0}} \ln\left(\frac{\xi_1}{\xi}\right) - K\left(\frac{1}{\xi^2} - \frac{1}{\xi_1^2}\right) - 10^{-3}(M\sigma^2 + NR_{R_0})\left(\frac{1}{\xi^4} - \frac{1}{\xi_1^4}\right) + \cdots \qquad (I\text{-}4)$$

where P and ξ are the dimensionless pressure and radial position, respectively, and K, M, and N are constants whose value depends on the solution technique. The first term on the right of Equation (I-4) represents the contribution of viscosity to the pressure drop while the other terms represent the effect of inertia.

Woolard [49], Benenson [3], Hagiwara [17], and Ishizawa [20,21] treat the flow in the diffuser region in terms of boundary layer theory. Assumptions common to all of these analyses are that the velocity profile is uniform at the entrance to the diffuser region and that boundary layers develop simultaneously on both surfaces which are symmetric relative to a plane midway between the surfaces. Hagiwara [18] found that the theoretical pressure distributions correspond well with experimental ones as long as primary separation does not occur. The assumed velocity profile of Ishizawa has enough flexibility that a mathematically non-singular separation point is predicted for the first time. This is possible because the flow is confined within the diffuser region, therefore the flows inside and outside of the separation region are necessarily related by continuity. The vortices predicted by Ishizawa form simultaneously on both the upper and lower surfaces downstream of the inlet radius. These studies do not reflect the experimentally observed behavior discussed previously. In actuality a boundary layer exists on the lower surface at the diffuser entrance, having developed in the stagnation region. The velocity

distribution at the diffuser entrance will be influenced by this boundary layer as well as the transition from axial to radial flow near the inlet corner which produces the primary vortex as described earlier. Under these circumstances the developing velocity field is most likely asymmetric.

In all of the above theoretical investigations the parabolic profile characteristic of a laminar two-dimensional flow between parallel flat walls is either assumed a priori or represents the asymptotic solution for the velocity field far downstream. For low flow rates Moller [35] experimentally measured parabolic velocity distributions at the exit radius, R_1.

The only study encompassing the whole radial diffuser was made by Parmet and Saibel [38,39], who solved the invicid flow specifying a uniform inlet velocity in the inlet tube and a uniform exit velocity at the outside radius of the diffuser. They found that the resulting free stream velocity above the lower surface to be imposed on a boundary layer solution is not linearly related to the radius throughout the stagnation region as for an axisymmetric Hiemenz flow. Thus, the thickness of the velocity and temperature boundary layers cannot be expected to be constant there.

2. Heat Transfer Investigations

The literature concerned with convective heat transfer in a radial diffuser is very limited. Thomas and Cobble [48] and Kreith [26,28] have experimentally and theoretically investigated the average heat transfer rate with both surfaces at the same temperature. The present thermal configuration is treated analytically for the average heat transfer rate by Kreith, who also simulates the problem with a mass transfer experiment [28]. Both investigators consider the flow to be

invicid and therefore the velocity distribution is uniform. Kreith also treats the case of a parabolic profile. Kreith [28] purposely minimized entrance effects in his experimental investigations by using a rounded inlet corner and applying an impervious coating on the mass transfer surface over a circular area beneath the inlet tube with a radius 3 times the inlet radius.

No literature was found concerning the local heat transfer rate in a radial diffuser. However, Akfirat [1] has experimentally determined the local heat transfer rate for a two-dimensional confined jet impinging upon an isothermal surface. Typical results are shown in Figure I-3 and exhibit several characteristics which may be common to the present investigation even though the possibility of vortex formations similar to those discussed above has been eliminated by the use of a rounded inlet corner. Firstly, the heat transfer distribution is not constant in the stagnation region but rises from the stagnation point to a maximum beneath the inlet corner. No region of Hiemenz flow is discernible. Secondly, the length of the downstream channel has virtually no effect on the stagnation region heat transfer distribution. Finally, for the highest flow rate of Figure I-3-b the heat transfer distribution begins to rise again because the laminar boundary layer, which has developed from the stagnation region, becomes turbulent.

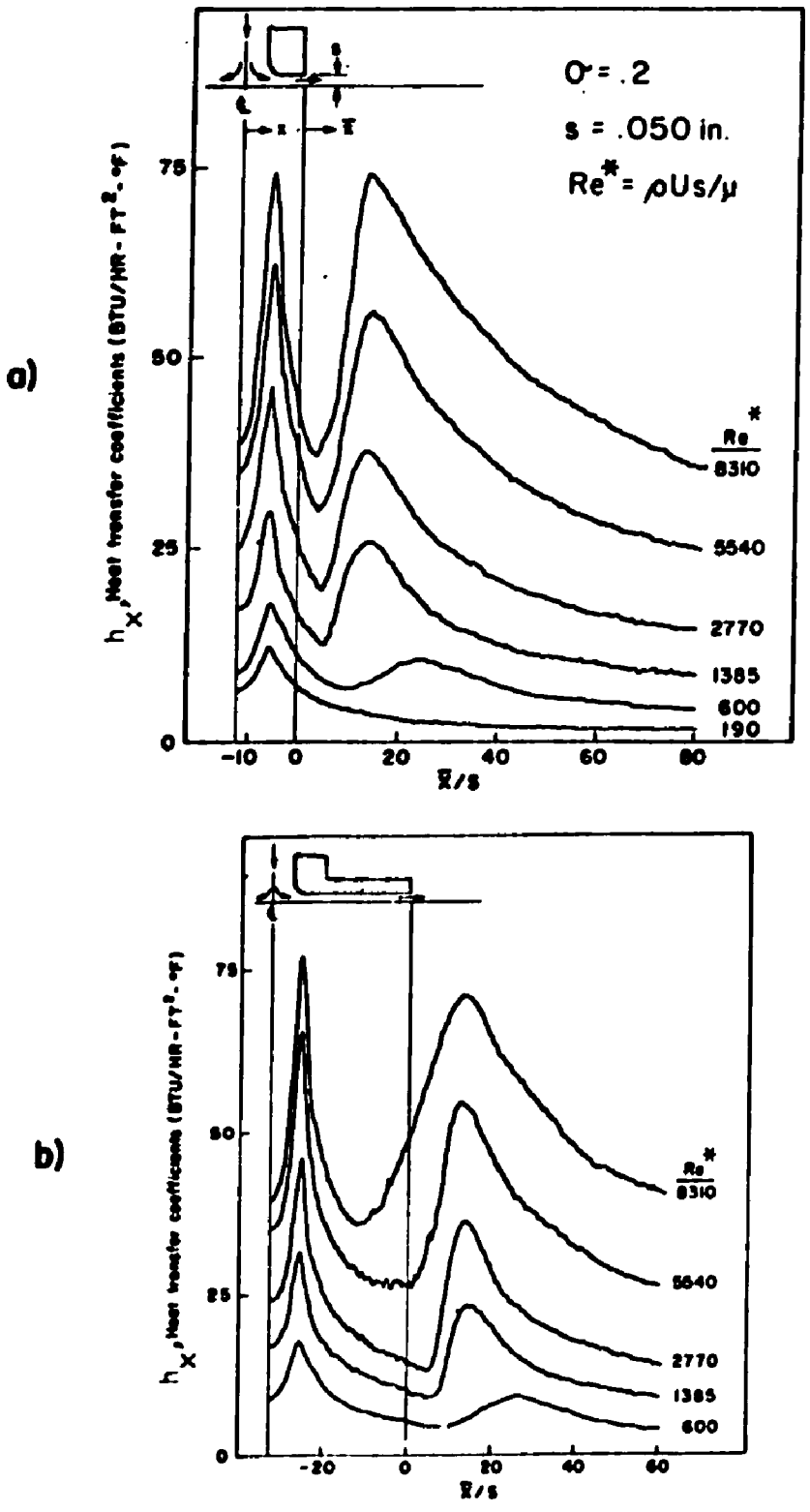


Figure 1-3. Heat Transfer Distributions in Two-Dimensional Stagnation Region.

CHAPTER II

THEORETICAL ANALYSIS

A. Problem Statement

The geometric configuration of the radial diffuser is shown in Figure I-1. It consists of two flat coaxial disk shaped surfaces of radius R_1 separated by an axial distance Z_o. The flow is introduced by an inlet tube of radius R_o which is coaxial with and joined to the upper surface. The incoming flow is at a uniform temperature T_o. The lower surface is maintained at temperature T_1, while the upper surface is insulated. It is desired to determine analytical expressions for the velocity and temperature fields and to determine the local heat transfer rate from the lower surface.

In the theoretical analysis the following general assumptions are made:

1) The fluid is incompressible.
2) The flow is steady, laminar, axisymmetric and swirlfree.
3) The properties of the fluid are constant.
4) Viscous dissipation is negligible.

In view of assumptions 1) and 3) the momentum and energy equations are decoupled, allowing the velocity field to be sought independently of the temperature field. Accordingly, the theoretical analysis for the velocity field is presented first and, for convenience, that for the temperature field is presented separately.

B. Velocity Field

1. Introduction

The flow in the diffuser region is depicted in Figure 2-1. The flow separates from the upper surface at the well defined sharp inlet corner and reattaches at radius R_{PR}. A primary vortex is formed by the recirculating fluid trapped between the separation streamline and the upper surface. This phenomenon occurs when the diffuser Reynolds number exceeds a critical value according to the experimental results listed in Table 1-1. In the theoretical analysis it is assumed that separation always exists at the inlet corner, hence a primary vortex exists whenever the primary reattachment radius is greater than the inlet radius, i.e. $R_{PR} > R_o$.

Approximate solutions are found for the velocity field in the diffuser region utilizing the Galerkin method of weighted residuals. The first solution employs an assumed velocity profile having one r-dependent free parameter. A closed form approximate solution is found from the second order volume perturbation of the governing equation. This solution is compared to the numerical solution of the governing equation by the Runge-Kutta integration technique. An integral equation is presented for the average radial pressure distribution in the diffuser region. The second solution for the velocity field utilizes an assumed velocity profile having two r-dependent free parameters. The resulting velocity distribution is more flexible than that with only one parameter. A numerical solution by the Runge-Kutta integration technique is found from the zeroth order volume perturbation of the governing equations.

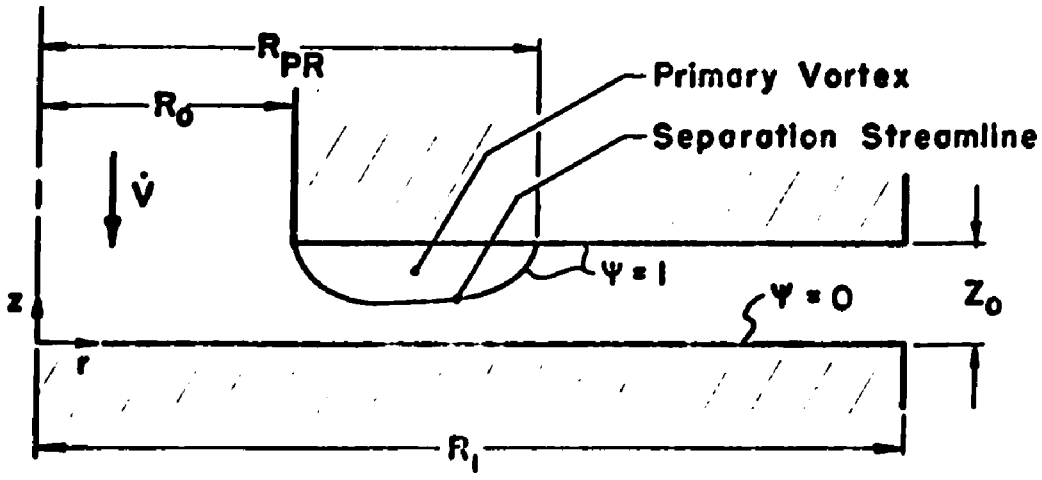


Figure 2-1. Analytical Model of Flow Field in Radial Diffuser.

2. General Differential Formulation

Under assumptions 1) through 4) listed in Section A. the continuity and momentum equations for flow in the diffuser region are

$$\frac{\partial}{\partial r}(ru) + \frac{\partial}{\partial z}(rv) = 0$$

$$\rho\left(u\frac{\partial u}{\partial r} + v\frac{\partial u}{\partial z}\right) = -\frac{\partial p}{\partial r} + \mu\left[\frac{\partial}{\partial r}\left(\frac{1}{r}\frac{\partial}{\partial r}(ru)\right) + \frac{\partial^2 u}{\partial z^2}\right]$$

$$\rho\left(u\frac{\partial v}{\partial r} + v\frac{\partial v}{\partial z}\right) = -\frac{\partial p}{\partial z} + \mu\left[\frac{\partial^2 v}{\partial r^2} + \frac{1}{r}\frac{\partial v}{\partial r} + \frac{\partial^2 v}{\partial z^2}\right]$$

subject to the boundary conditions

$$u(r,0) = 0; \quad u(r,Z_o) = 0$$

$$v(r,0) = 0; \quad v(r,Z_o) = 0$$

and conservation of mass

$$\dot{V} = 2\pi\int_0^{Z_o} ur\,dz$$

The continuity equation is satisfied identically by introducing the stream function ψ, where

$$ru = \frac{\partial \psi}{\partial z}; \quad rv = -\frac{\partial \psi}{\partial r}$$

Utilizing ψ and the dimensionless variables

$$\xi = \frac{r}{R_o}; \quad \eta = \frac{z}{Z_o}$$

$$\Psi = \frac{2\pi}{\dot{V}}\psi; \quad \mathcal{P} = \frac{p}{\rho U_{R_o}^2}$$

the momentum equations become

$$\psi_\eta\left(\psi_{\eta\xi}-\frac{1}{\xi}\psi_\eta\right)-\psi_{\eta^2}\psi_\xi=-\xi^2\Omega_\xi+\frac{2}{R_{R_o}}\left[\xi\psi_{\eta^3}+\frac{\sigma^2}{4}\left(\xi\psi_{\eta\xi^2}-\psi_{\eta\xi}\right)\right]$$

$$\psi_\eta\left(-\psi_{\xi^2}+\frac{1}{\xi}\psi_\xi\right)+\psi_\xi\psi_{\eta\xi}=-\frac{4\xi^2}{\sigma^2}\Omega_\eta+\frac{2}{R_{R_o}}\left[-\xi\psi_{\eta^2\xi}-\frac{\sigma^2}{4}\left(\xi\psi_{\xi^3}-\psi_{\xi^2}+\frac{1}{\xi}\psi_\xi\right)\right]$$

where $\psi_\eta=\frac{\partial\psi}{\partial\eta}$, $\psi_{\eta^2}=\frac{\partial^2\psi}{\partial\eta^2}$, $\psi_{\eta\xi}=\frac{\partial^2\psi}{\partial\xi\partial\eta}$, etc. These equations bring out the basic dimensionless groups for the diffuser region as follows: $\sigma=2Z_o/R_o$, the ratio of the area at the inlet to the diffuser region to the area of the inlet tube; $R_{R_o}=\sigma Re/4$, the diffuser Reynolds number; and $Re=2\bar{v}/\nu R_o$ the inlet Reynolds number. The diffuser Reynolds number R_{R_o} is defined in terms of the inlet Reynolds number for convenience.

Introducing the coordinate transformation $s=\xi^2$ serves to reduce the momentum equations to

$$\psi_\eta\left(2\psi_{\eta s}-\frac{1}{s}\psi_\eta\right)-2\psi_s\psi_{\eta^2}=-2s\Omega_s+\frac{2}{R_{R_o}}\left(\psi_{\eta^3}+\sigma^2 s\psi_{\eta s^2}\right) \quad (2\text{-}1\text{-}a)$$

$$\psi_\eta\psi_{s^2}-\psi_s\psi_{\eta s}=\frac{1}{\sigma^2}\Omega_\eta+\frac{1}{R_{R_o}}\left[\psi_{\eta^2 s}+\sigma^2\left(\psi_{s^2}+s\psi_{s^3}\right)\right] \quad (2\text{-}1\text{-}b)$$

Equation (2-1-b) has also undergone a sign change.

Being primarily interested in the velocity field, the pressure terms are eliminated from the preceding equations in the usual way by the cross differentiation and addition of the two momentum equations. The resulting governing partial differential equation is

$$\psi_\eta\left(\frac{1}{s}\psi_{\eta^2}-\psi_{\eta^2 s}-\sigma^2 s\psi_{s^3}\right)+\psi_s\left(\psi_{\eta^3}+\sigma^2 s\psi_{\eta s^2}\right)=$$

$$-\frac{1}{R_{R_o}}\left[\psi_{\eta^4}+2\sigma^2 s\psi_{\eta^2 s^2}+\sigma^4 s\left(2\psi_{s^3}+s\psi_{s^4}\right)\right] \quad (2\text{-}2\text{-}a)$$

subject to the boundary conditions

$$\psi(\xi,0)=0 \;;\quad \psi_\eta(\xi,0)=0$$
$$\psi(\xi,1)=1 \;;\quad \psi_\eta(\xi,1)=1 \qquad \text{(2-2-b)}$$

3. One-Parameter Case

To obtain an approximate solution to Equation (2-2-a) an approximating function is assumed for the stream function which satisfies the boundary conditions given by Equation (2-2-b) while leaving one r-dependent parameter undetermined. By substituting the approximating function for the stream function into Equation (2-2-a) and applying the Galerkin method of weighted residuals, the governing equation is reduced to an ordinary differential equation in terms of the free parameter. Next, appropriate boundary conditions must be found for the free parameter based on the physics of the problem and asymptotic conditions generated from the governing equation. The reformulation being complete, solutions can now be sought using various techniques.

a. Formulation

1. Approximating Function

The stream function is approximated by a power series expansion in η of the form

$$\psi = \sum_{n=0}^{\infty} a_n \eta^n = a_0 + a_1\eta + a_2\eta^2 + a_3\eta^3 + \cdots \;;\quad a_n = a_n(\xi) \qquad \text{(2-3)}$$

Truncating the series at the fourth order term and applying the four boundary conditions of Equation (2-2-b) leaves one

parameter, F, free so that the stream function becomes

$$\Psi = (3\eta^2 - 2\eta^3) + (\eta^2 - 2\eta^3 + \eta^4)F; \quad F = F(\mathcal{Y}) \qquad (2\text{-}4\text{-}a)$$

$$= H_0 + H_1 F; \quad H_n = H_n(\eta) \qquad (2\text{-}4\text{-}b)$$

while the velocity field in the r-direction becomes

$$u = \frac{6}{\sqrt{5}}(\eta - \eta^2) + \frac{2}{\sqrt{5}}(\eta - 3\eta^2 + 2\eta^3)F \qquad (2\text{-}5\text{-}a)$$

$$= \frac{1}{\sqrt{5}}(H_0^I + H_1^I F) \qquad (2\text{-}5\text{-}b)$$

where the Roman numeral superscript denotes the order of derivatives of functions of a single independent variable. The function H_0^I is parabolic and is the well known asymptotic solution far downstream, as demonstrated below in APPENDIX I. The function H_1^I is odd with respect to the plane at $\eta = \frac{1}{2}$ and is shown in Figure 2-7. The velocity distributions for particular values of the free parameter are shown in Figure 2-2. It is evident that the reversed flow characteristic of a primary vortex can be obtained with the velocity field given by Equations (2-5) when F has a value greater than 3. Conversely when F is less than -3 a secondary vortex occurs, i.e., a reversed flow occurs near the lower surface.

II. Governing Equation

Having determined the approximating function for the stream function, the free parameter is found by requiring that the trial solution satisfy the governing partial differential equation in a specified integral sense, e.g.

$$\int_{\gamma_1}^{\gamma_2} DE(f)\, W(y)\, dy = 0$$

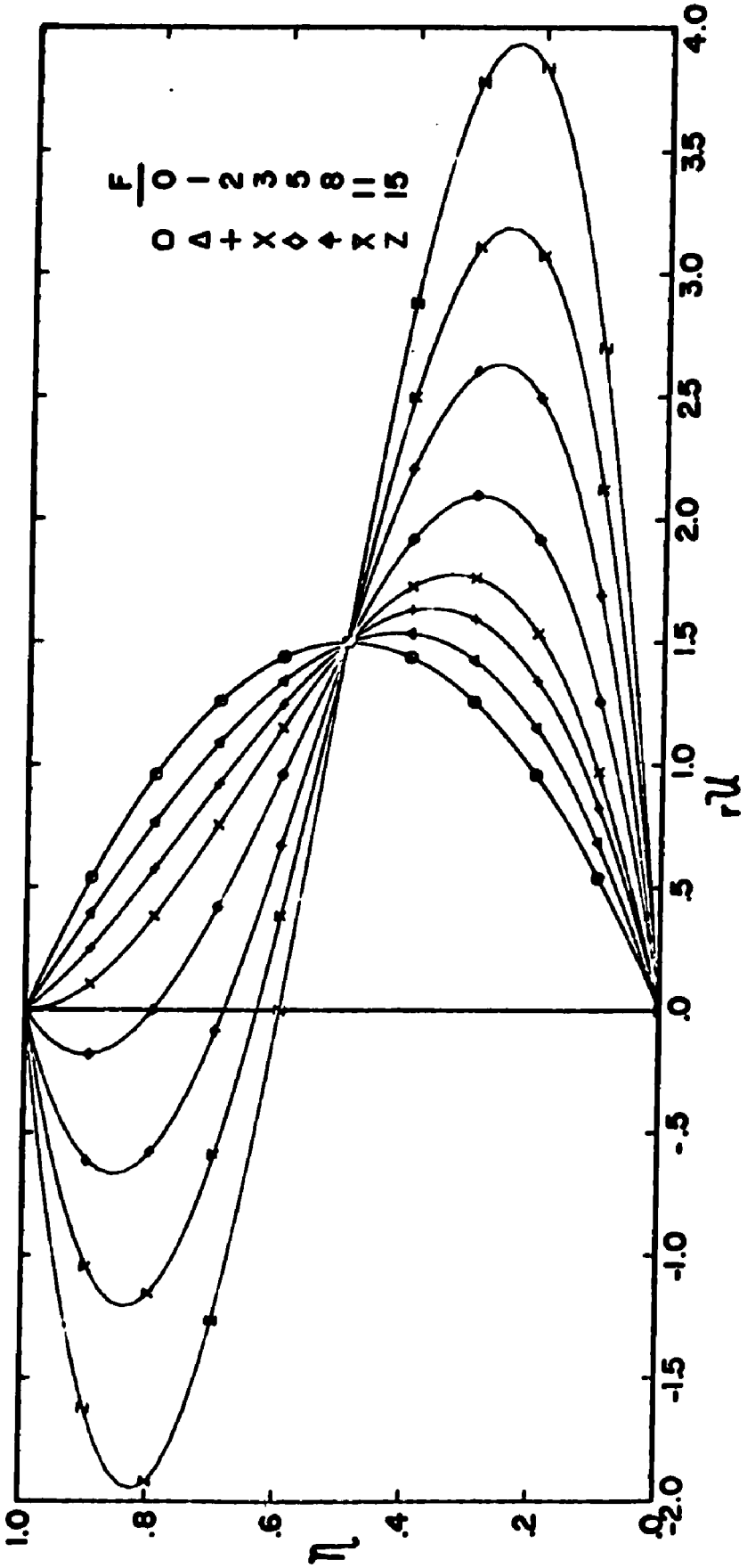


Figure 2-2. One-Parameter Velocity Distributions.

where $DE(f)$ is the partial differential equation for $f(x,y)$ and W (y) is a weighting function which depends on the coordinate y over which the integration is performed. The resulting equation is an ordinary differential equation with the orthogonal coordinate x as the independent variable. This approximation scheme is referred to as the method of weighted residuals in continuum field theory [11,12] and as the moment procedure in kinetic theory. Various techniques are used to specify the weighting function. For instance, the simplest weighting function is unity in which case the technique is known alternatively as the method of moments, the integral method, or the Karman-Pohlhausen method [11,12].

The technique utilized to determine the weighting function in this section is the Galerkin method. For a trial solution of the form

$$f(x,y) \cong \sum_{n=0}^{m} \chi_n(x)\, y_n(y)$$

where the functions $\chi_n(x)$ are the free parameters and the functions $y_n(y)$ are polynomials, the weighting functions determined according to the Galerkin method are

$$W_n = \frac{\partial f}{\partial \chi_n} = y_n$$

For the present case the weighting function from the approximating function of Equations (2-4) is the function H_1. Applying the Galerkin method of weighted residuals to Equation (2-2-a) over the interval $0 \le \eta \le 1$ reduces the governing fourth order partial differential equation to the ordinary fourth order differential equation

$$132\left(\frac{42}{R_{x_0}}\vartheta - 1\right)F + 663F^{I} - 264\frac{\sigma^2}{R_{R_0}}\vartheta^2 F^{II} - \sigma^2\left(15 - 22\frac{\sigma^2}{R_{R_0}}\right)\vartheta^2 F^{III} + 11\frac{\sigma^4}{R_{x_0}}\vartheta^3 F^{IV} = 0 \quad (2\text{-}6\text{-}a)$$

III. Boundary Conditions

The governing equation being of fourth order requires four boundary conditions if the solution is to be complete. The physics of the problem indicate that for a primary vortex to occur the flow must separate at the inlet corner, i.e.

$$\psi_{\eta\eta}(1,1) = 0 \tag{2-7}$$

which is satisfied, according to Equation (2-4-a), when

$$F(1) = 3 \tag{2-6-b}$$

Similarly, primary reattachment occurs at ξ_{PR} when

$$\psi_{\eta\eta}(\xi_{PR},1) = 0 \tag{2-8}$$

or

$$F(\xi_{PR}) = 3 \tag{2-9}$$

In the subsequent analysis it is assumed that separation always occurs at the inlet corner, hence Equation (2-6-b) becomes one of the required boundary conditions. From Equations (2-6-b) and (2-9) it is evident that a primary vortex will occur only when the reattachment distance, ξ_{PR}, is greater than unity.

In APPENDIX I another boundary condition is deduced based on the fact that the velocity distribution asymptotically approaches a parabolic profile far downstream, i.e.

$$F(\xi) = 0; \quad \xi \gg 1 \tag{2-6-c}$$

Since no other boundary conditions can be deduced based on physical reasoning, two additional boundary conditions are developed in APPENDIX II from a coordinate perturbation of Equation (2-6-a) near the inlet radius, thus bringing the total number of boundary conditions to 4 as required. To the first approximation the two additional boundary conditions are

$$F^{I}(1) = 6\left(1 - \frac{42}{R_{R_o}}\right) \qquad \text{(A-5-a)}$$

$$F^{II}(1) = 6\left(1 - \frac{168}{R_{R_o}} + \frac{3520}{R_{R_o}^2}\right) \qquad \text{(A-5-b)}$$

These boundary conditions are discussed further in APPENDIX II and in Section c of this chapter.

b. Perturbation Solution

Let the free parameter, F, be written as a power series expansion in the volume perturbation parameter $\epsilon = \sigma^2$:

$$F = \sum_{n=0}^{\infty} \epsilon^n F_n = F_0 + \epsilon F_1 + \epsilon^2 F_2 + \cdots \; ; \quad F_n = F_n(\eta) \qquad (2\text{-}10)$$

Substituting Equation (2-10) into Equation (2-6-a) and arranging in terms of ϵ^n, the first two approximations are

First Approximation, ϵ^0:

$$2\left(\frac{42}{R_{R_o}}\eta - 1\right)F_0 + \eta F_0^{I} = 0$$
$$F_0(1) = 3$$

Second Approximation, ϵ^1:

$$44\left(\frac{42}{R_{R_o}}\eta - 1\right)F_1 + 22\eta F_1^{I} - \frac{88}{R_{R_o}}\eta^2 F_0^{II} - 5\eta^2 F_0^{III} = 0$$
$$F_1(1) = 0$$

The solution of the first approximation is

$$F_0 = 3\eta^2 e^{-\frac{84}{R_{R_0}}(\eta-1)} \qquad (2\text{-}11\text{-}a)$$

while that of the second approximation is

$$F_1 = \phi F_0 \; ; \quad \phi = \phi(\eta)$$

where

$$\phi = -\frac{4}{11R_{R_0}}\left[293\ln\eta - \frac{22764}{R_{R_0}}(\eta-1) + \frac{146412}{R_{R_0}^2}(\eta^2-1)\right] \qquad (2\text{-}11\text{-}b)$$

Thus, the solution for F is, to the second approximation,

$$F = (1+\sigma^2\phi)F_0 \qquad (2\text{-}11\text{-}c)$$

The radial variation of F according to Equations (2-11) is shown in Figure 2-3 for various values of the area ratio, σ, and the diffuser Reynolds number, R_{R_0}. The results are expected to be valid as long as the area ratio is at least less than unity. Further discussion of the results is deferred to Section e of this chapter.

c. Numerical Solution

As a check on the range of the area ratio for which the perturbation solution given by Equations (2-11) is valid, Equation (2-6-a) was solved using the Runge-Kutta numerical integration technique. In APPENDIX II it is demonstrated that the first derivative of the free parameter, F, at the inlet corner is given by Equation (A-5-a) for an area ratio less than 0.1. In this light Equation (2-6-a) may be reduced to a third order equation by assuming that the ratio σ^2/R_{R_0} is much less than unity, whence the numerical formulation becomes

$$44\left(\frac{42}{R_{R_0}}\eta - 1\right) + 223F^{I} - 88\frac{\sigma^2}{R_{R_0}}\eta^2F^{II} - 50\sigma^2\eta^2F^{III} = 0 \qquad (2\text{-}12\text{-}a)$$

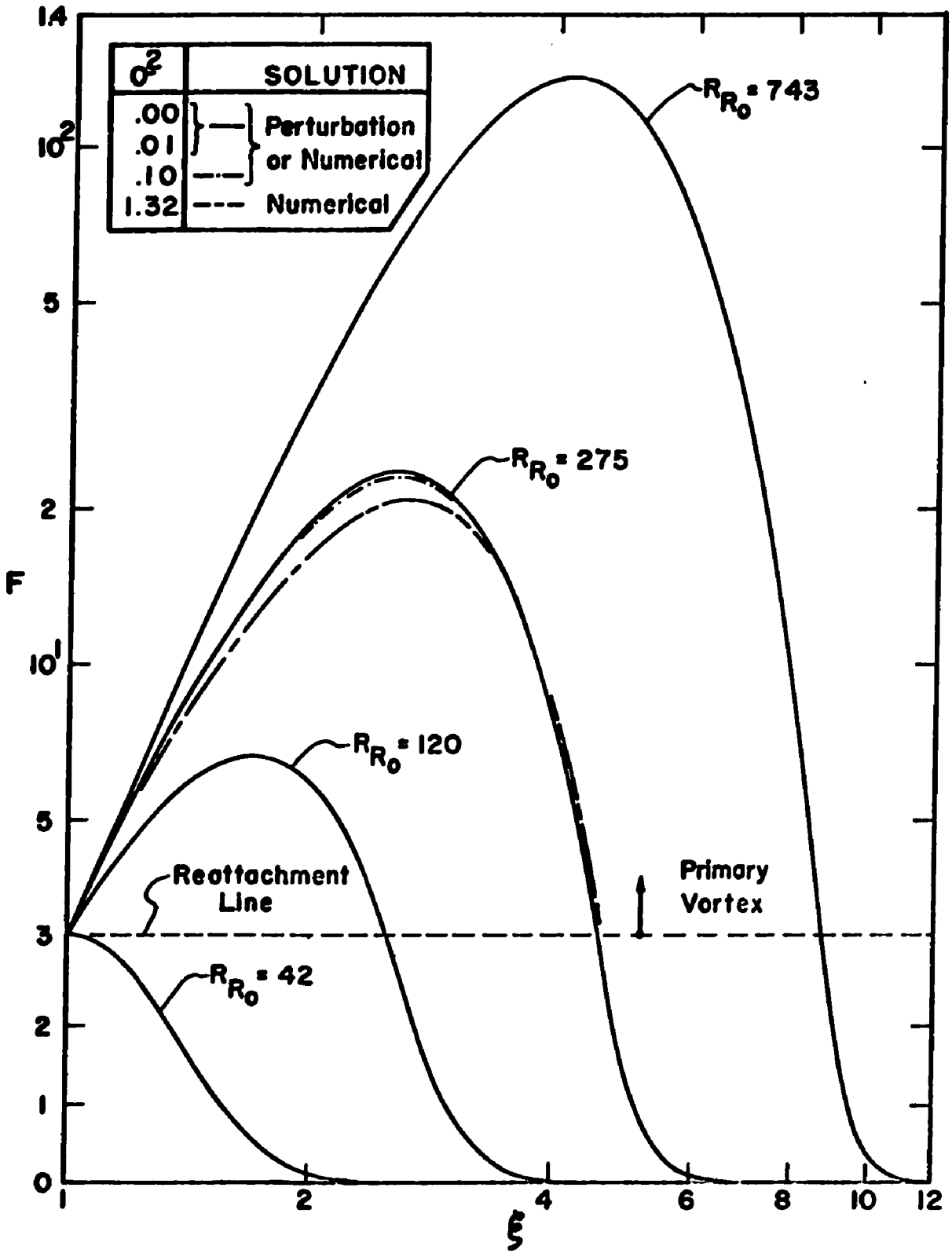


Figure 2-3. Radial Variation of Free Parameter.

subject to the boundary conditions

$$F(1) = 3 \; ; \; F(\infty) = 0$$
$$F'(1) = 6\left(1 - \frac{\sigma^2}{R_{R_o}}\right) \qquad (2\text{-}12\text{-}b)$$

The solution of Equation (2-12) for various values of area ratio, σ, and diffuser Reynolds number, R_{R_o}, is shown in Figure 2-3.

d. Pressure Field

Rearranging Equations (2-1) gives the pressure terms as

$$P_\xi = \frac{1}{\xi R_{R_o}}\left(\psi_{\eta\eta} + \sigma^2 \xi \psi_{\eta\xi^2}\right) - \frac{1}{2\xi}\psi_\eta\left(2\psi_{\eta\xi} - \frac{1}{\xi}\psi_\eta\right) + \frac{1}{\xi}\psi_\xi \psi_{\eta\xi}$$
$$P_\eta = -\frac{\sigma^2}{R_{R_o}}\left[\psi_{\eta\xi\xi} + \sigma^2\left(\psi_{\xi^3} + \xi\psi_{\xi^3}\right)\right] + \sigma^2\psi_\eta\psi_{\xi^2} - \sigma^2\psi_\xi\psi_{\eta\xi} \qquad (2\text{-}14\text{-}a)$$

subject to the boundary condition

$$P(\xi_1, \eta) = P_o \qquad (2\text{-}14\text{-}b)$$

If dP is an exact differential, $P_{\xi\eta} = P_{\eta\xi}$ and P can be evaluated by integrating the first-order differential equation $dP = P_\xi d\xi + P_\eta d\eta$ giving [29]

$$P(\xi,\eta) - P(\xi_*, \eta_*) = \int_{\xi_*}^{\xi} P_\xi(\xi, \eta)\, d\xi + \int_{\eta_*}^{\eta} P_\eta(\xi_*, \eta)\, d\eta \qquad (2\text{-}15)$$

where the subscript asterisk denotes a reference position which will be $(\xi_1, 0)$ in the following analysis.

Since the stream function is known only approximately according to Equations (2-4), evaluation of the pressure from Equations (2-14) can itself be only approximate. Consequently, in the following

analysis the solution of Equation (2-15) is sought on an integral basis in terms of the average pressure, $\bar{\theta}$, at any radius, i.e.

$$\bar{\theta}(\gamma)-\theta(\gamma_1)=\int_0^1\left\{\int_{\gamma_1}^{\gamma}\theta_\gamma(\gamma',\eta)\,d\gamma'+\int_0^{\eta''}\theta_\gamma(\gamma_1,\eta')\,d\eta'\right\}d\eta'' \qquad (2\text{-}16)$$

Substitution of Equations (2-4) and Equations (2-14) into Equation (2-16) gives the average pressure distribution for a one-parameter velocity field as

$$\bar{\theta}(\gamma)-\theta_0=-\frac{12}{R_{Re}}\ln\left(\frac{\gamma}{\gamma_1}\right)-\frac{3}{5}\left(\frac{1}{\gamma}-\frac{1}{\gamma_1}\right)+\frac{1}{105}\int_{\gamma_1}^{\gamma}\left(\frac{F}{\gamma}-4F^{-1}\right)\left(\frac{F}{\gamma}\right)d\gamma \qquad (2\text{-}17)$$

The first and second terms on the right hand side of Equation (2-17) correspond to the first two terms of Equation (1-4); the last term represents the effect of the primary vortex. The coefficient of the second term is the same as that found by other authors listed in Table 1-2 using the momentum integral technique with a parabolic velocity profile.

e. Discussion of Results

Figure 2-3 shows that the second perturbation approximation for the free parameter, given by Equation (2-11-a) agrees well with the numerical results for $\sigma^2 \leq .1$. The numerical results are very insensitive to small changes in the initial slope value, thus justifying the use of Equation (A-5-a) for this condition. Because of its closed form, the second perturbation approximation will be used to describe the flow field in the solution of the energy equation in Section c instead of the more involved numerical integration solution.

In Figure 2-2 above the reversed flow characteristic of a primary vortex occurs when the free parameter, F, exceeds a value of 3. Consequently, a primary vortex exists when the free parameter

exceeds this value in Figure 2-3.

It is possible to establish a criterion for the existence of a primary vortex. Since the flow must separate at the inlet corner when a primary vortex occurs, the separation streamline must leave the surface. The relationship between the free parameter, F, and the axial position of the separation streamline, η_p, derived in APPENDIX III indicates that a primary vortex exists when

$$\eta_p^I(1) = -F^I(1) < 0$$

or

$$F^I(1) > 0 \qquad \text{(A-8-c)}$$

thus, from Equation (A-5-a),

$$F^I(1) = 6\left(1 - \frac{42}{R_{R_o}}\right) > 0 \qquad \text{(2-13-a)}$$

whence

$$R_{R_o} > 42 \qquad \text{(2-13-b)}$$

Equations (2-13) show that the diffuser Reynolds number R_{R_o} must exceed a critical value of 42 for a primary vortex to occur when the area ratio is less than 0.1. The critical value of 42 is actually an upper bound because, as shown in Figure A-1, Equation (A-8-c) is satisfied at lower diffuser Reynolds numbers as the area ratio increases. Correspondingly, as the area ratio increases, the inlet Reynolds number at which a primary vortex exists decreases, e.g., for a constant inside radius R_o, the primary vortex will exist at lower inlet Reynolds numbers as the surface separation Z_o increases.

The flow reattaches when

$$F(\xi_{PR}) = 3 \qquad \text{(2-9)}$$

in Figure 2-3, where ξ_{PR} is the primary reattachment radius. The increase of ξ_{PR} with increasing diffuser Reynolds number is shown below in Figure 3-3 for squared area ratios of 0.01 and 1.322 based on the second perturbation and numerical solutions for the free parameter, respectively. The latter curve is presented because it indicates that the effect of the area ratio becomes important for small diffuser Reynolds numbers - below a value of 100, in this case. Although the theoretical results indicate that the primary vortex length grows without bound as the diffuser Reynolds number increases, experimental studies discussed in the literature survey indicate that a critical diffuser Reynolds number exists beyond which no further growth occurs as a result of the fact that the flow becomes turbulent.

The maximum thickness of the primary vortex, $T = 1-\eta_{p,min}$, is shown in Figure 3-4 for squared area ratios of .01 and 1.322 based on the second perturbation and numerical solutions for the free parameter, respectively. The latter curve is included because it indicates that T is theoretically largely independent of changes in area ratio.

The effect of the primary vortex on the average velocity of the primary flow, $\bar{u}_p$, i.e., the average flow between the separation streamline and the lower surface, is shown in Figures 2-4 and 2-5 based on the second perturbation solution for the free parameter with an area ratio much less than unity. Figure 2-4 shows that is an order of magnitude larger than the average velocity between the surfaces, $\bar{u}$, when the diffuser Reynolds number reaches a value of 734. Hence, while $\bar{u}$ is inversely proportional to the radius, the primary vortex may cause $\bar{u}_p$ to decrease less rapidly or even increase with increasing radius as shown in Figure 2-5. The primary vortex exerts

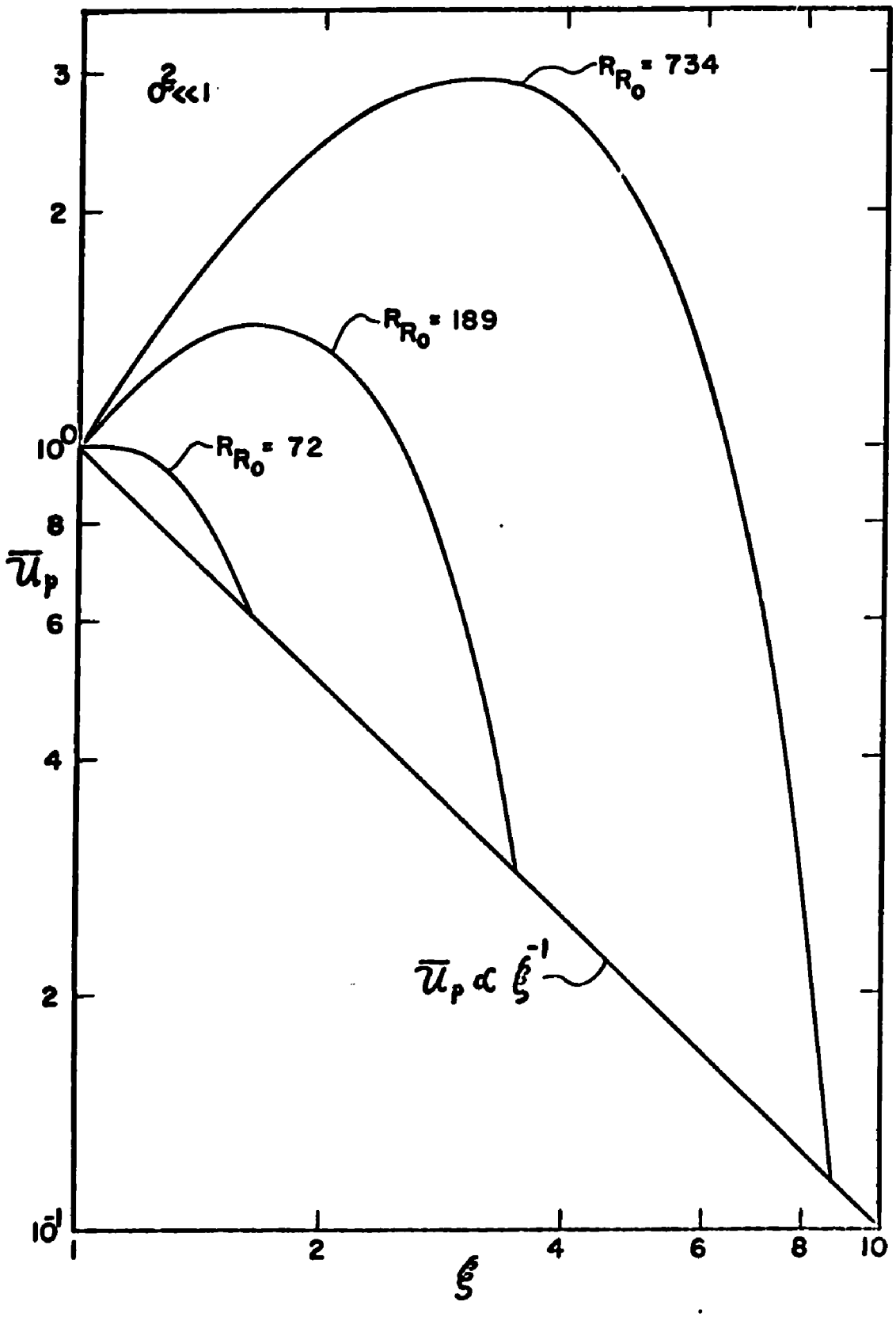


Figure 2-4. Radial Variation of Average Primary Flow Rate.

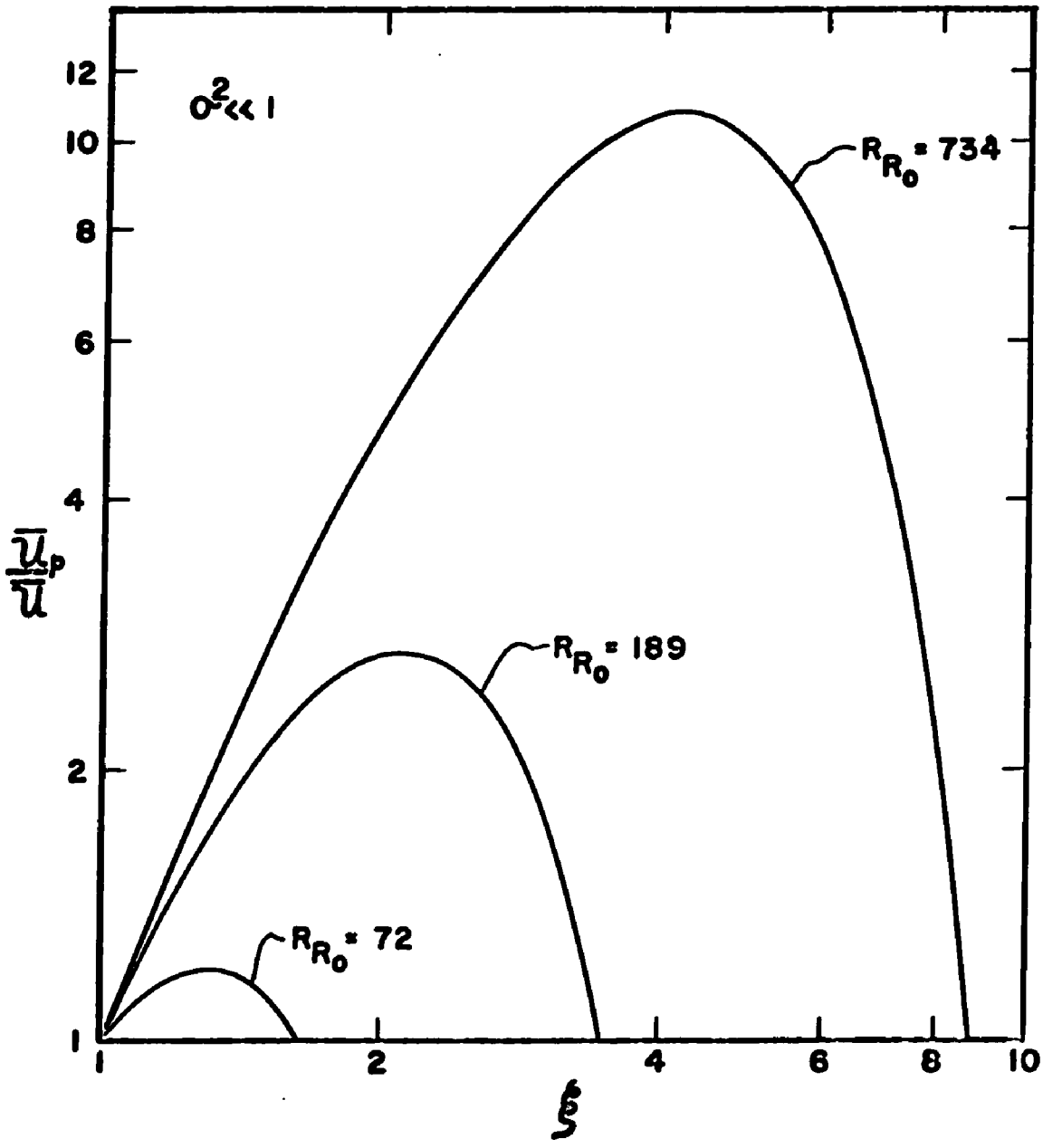


Figure 2-5. Radial Variation of Ratio of Average Primary Flow Rate to Average Flow Rate.

a considerable influence on the velocity field; consequently, it is expected to have a significant influence on the temperature field as well.

No secondary vortex results from any of the one-parameter solutions; a consequence of the fact that primary and secondary vortices cannot exist simultaneously with a one-parameter velocity profile. Experimental evidence discussed in the literature survey indicates that the secondary flow detaches before the primary flow reattaches.

Pressure distributions according to Equation (2-17) are shown in Figure 2-6 based on the second perturbation solution for the free parameter with an area ratio much less than unity. For comparison Equation (1-4) is also shown. No vortex exists for the two lower diffuser Reynolds numbers but the effect of the asymmetric flow is clearly evident near the inlet radius. For the two higher diffuser Reynolds numbers a primary vortex does exist and the pressure distributions are depressed further from the inlet radius, especially for the highest diffuser Reynolds number. The theoretical pressure distributions are in fair agreement with those measured experimentally by Moller [35] and Hagiwara [18].

4. Two-Parameter Case

In a manner analagous to that followed for one free parameter an approximate solution to Equation (2-2-a) may be found by assuming an approximating function for the stream function which leaves two r-dependent parameters undetermined. The increased flexibility imparted to the trial velocity profile by the additional parameter hopefully but not necessarily improves the approximation of the actual flow field, e.g., a secondary vortex may possibly be determined theoretically now. Usually as additional undetermined

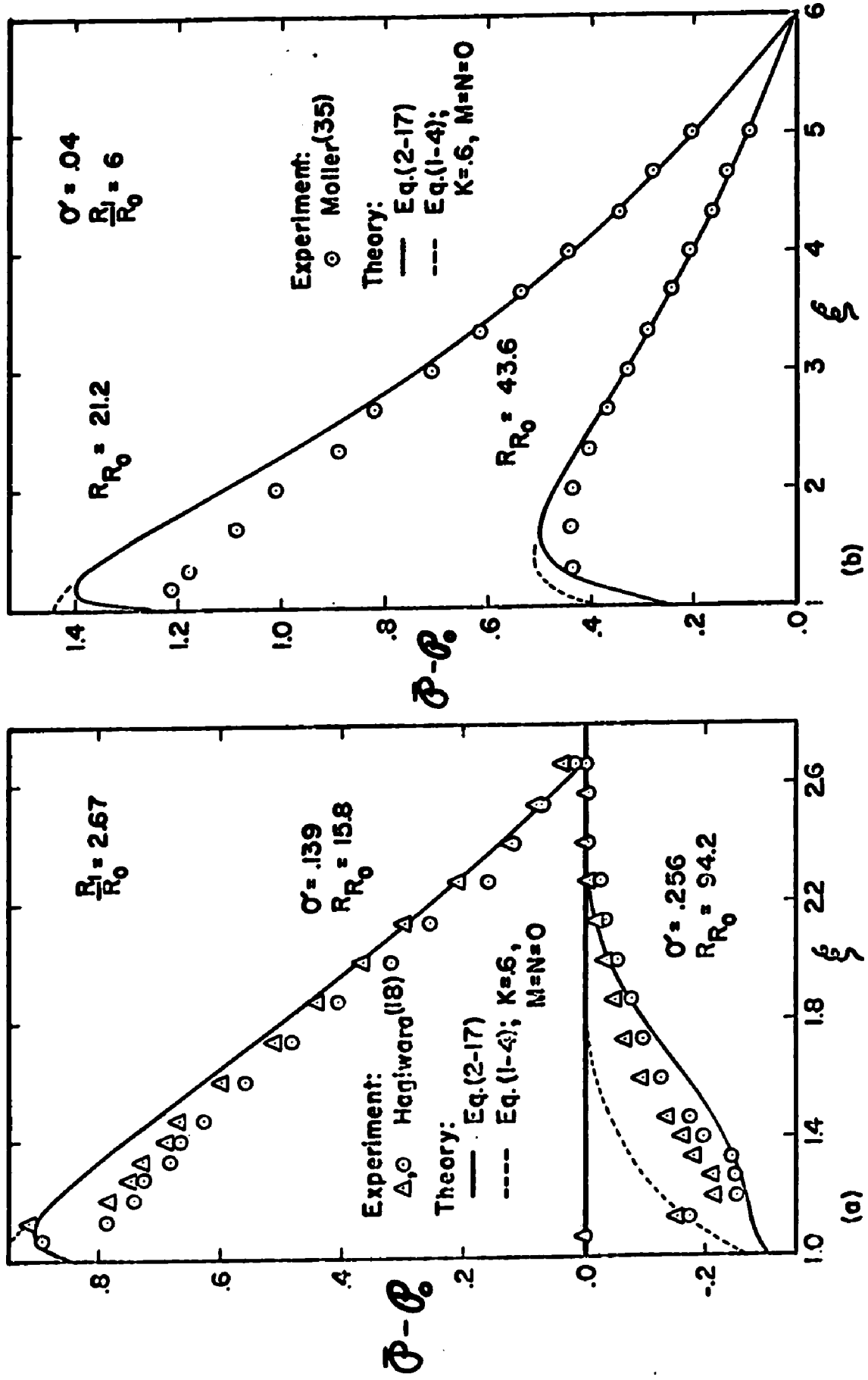


Figure 2-6. Radial Pressure Distributions.

parameters are introduced in the Galerkin method of weighted residuals the solutions converge but there is no way to ascertain whether the convergence is toward the exact solution [11,12].

a. Formulation

1. Approximating Function

Truncating the stream function approximation of Equation (2-3) at the fifth order term and applying the four boundary conditions of Equation (1-b) leaves two parameters, F_1 and F_2, free so that the stream function becomes

$$\Psi = (3\eta^2-2\eta^3)+(\eta^3-2\eta^4+\eta^5)F_1+(2\eta^2-3\eta^3+\eta^5)F_2 \; ; \quad F_n = F_n(S) \qquad (2\text{-}18\text{-}a)$$

$$= H_0 + H_1F_1 + H_2F_2 \; ; \quad H_n = H_n(\eta) \qquad (2\text{-}18\text{-}b)$$

while the velocity field in the r-direction becomes

$$u = \frac{6}{\sqrt{5}}(\eta-\eta^2)+\frac{2}{\sqrt{5}}(\eta-3\eta^2+2\eta^3)F_1+\frac{1}{\sqrt{5}}(4\eta-9\eta^2+5\eta^4)F_2 \qquad (2\text{-}19\text{-}a)$$

$$= \frac{1}{\sqrt{5}}(H_0^I + H_1^IF_1 + H_2^IF_2) \qquad (2\text{-}19\text{-}b)$$

where the functions H_0^I, H_1^I, and H_2^I are conveniently factored as

$$H_0^I = \eta(1-\eta)$$
$$H_1^I = \eta(1-\eta)(1-2\eta)$$
$$H_2^I = \eta(1-\eta)(4-5\eta-5\eta^2)$$

It is evident that the functions H_0^I, H_1^I, and H_2^I are merely weighted parabolic functions. Functions H_1^I and H_2^I are shown in Figures 2-7 and 2-8. The functions H_0^I and H_1^I are the same functions previously used in Equation (2-5) to describe the one-parameter radial velocity field, i.e., the two-parameter stream function is reduced to the

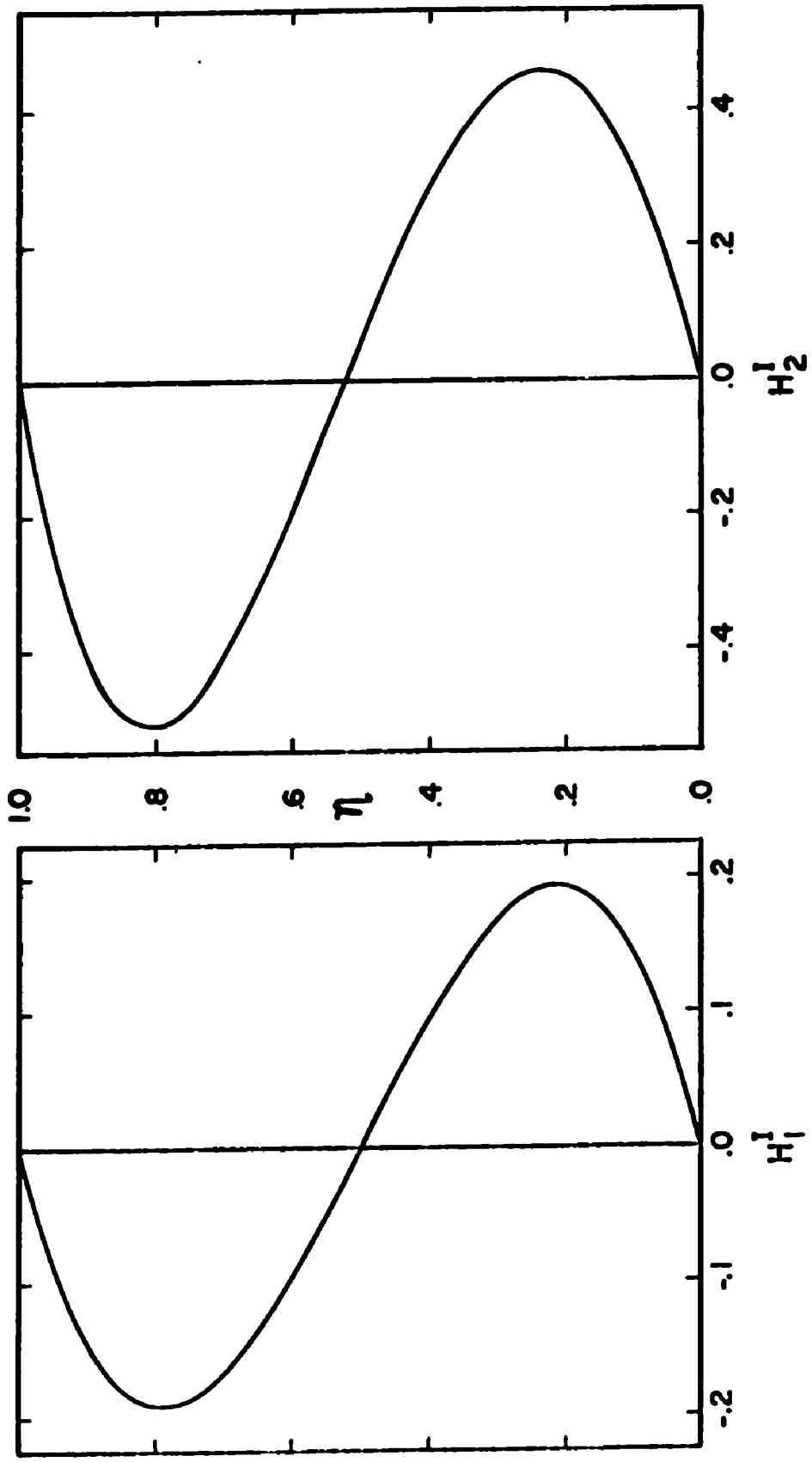


Figure 2-8. Function H_2 (η).

Figure 2-7. Function H_1 (η).

one-parameter form when the second parameter is zero. The function H_2^I resembles the function H_1^I except that it is not quite an odd function with respect to the plane at $\eta = \frac{1}{2}$.

Representative velocity profiles at a separation or reattachment point are shown in Figure 2-9 for various combinations of the free parameters F_1 and F_2 as related by Equation (2-24) which is discussed below. Seven profiles out of an infinite set are shown. In the one-parameter case only one existed. When the curvature of the axial velocity distribution at the separation or reattachment point becomes negative physically unrealizable flows are predicted, thus limiting the second free parameter, F_2, to values of at least -4.

Velocity profiles symmetric with respect to the plane at $\eta = \frac{1}{2}$ occur when the derivative of the radial velocity with respect to the axial coordinate is zero at the centerline, i.e.

$$V_{\xi^2}(\xi, \tfrac{1}{2}) = 0$$

This necessary and, for the present case, sufficient condition is satisfied, according to Equation (2-18-a), when the two free parameters are related by

$$F_1 = -2.5\, F_2 \qquad (2\text{-}20)$$

Several symmetric velocity profiles are shown in Figure 2-10 with the free parameters evaluated according to Equation (2-20). Physically meaningful flows, i.e. flows where the maximum velocity occurs at the centerline, exist in this case only when the second free parameter, F_2, has a value of at least -4. Symmetric profiles other than a parabola were not possible in the one-parameter case.

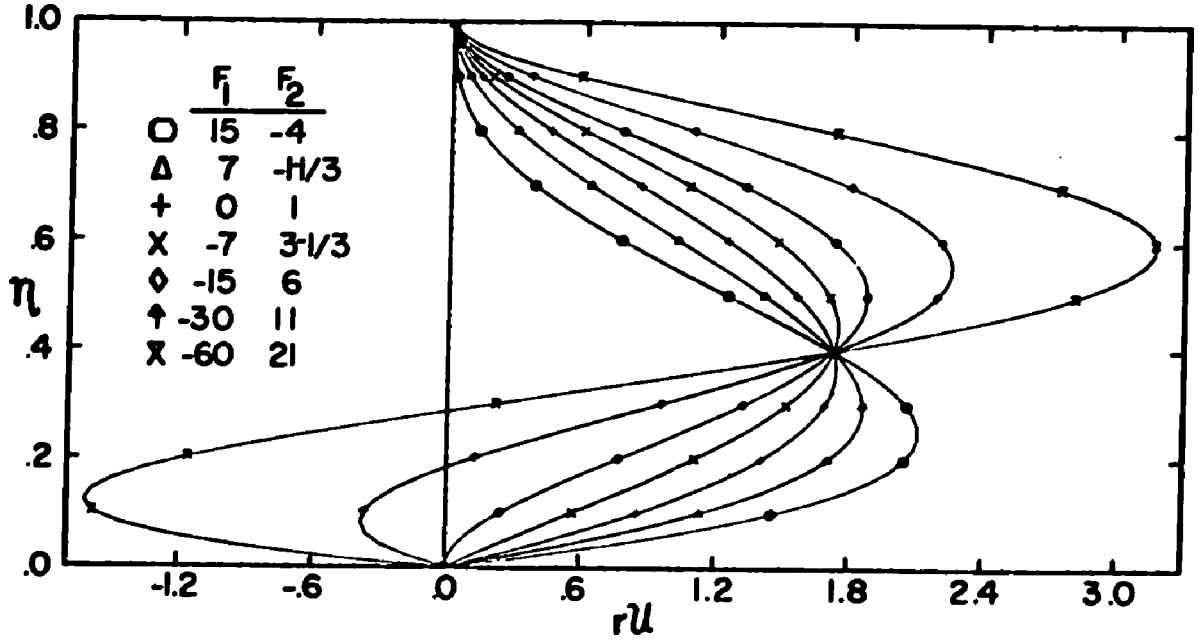


Figure 2-9. Separation Velocity Profiles, Two-Parameter Case.

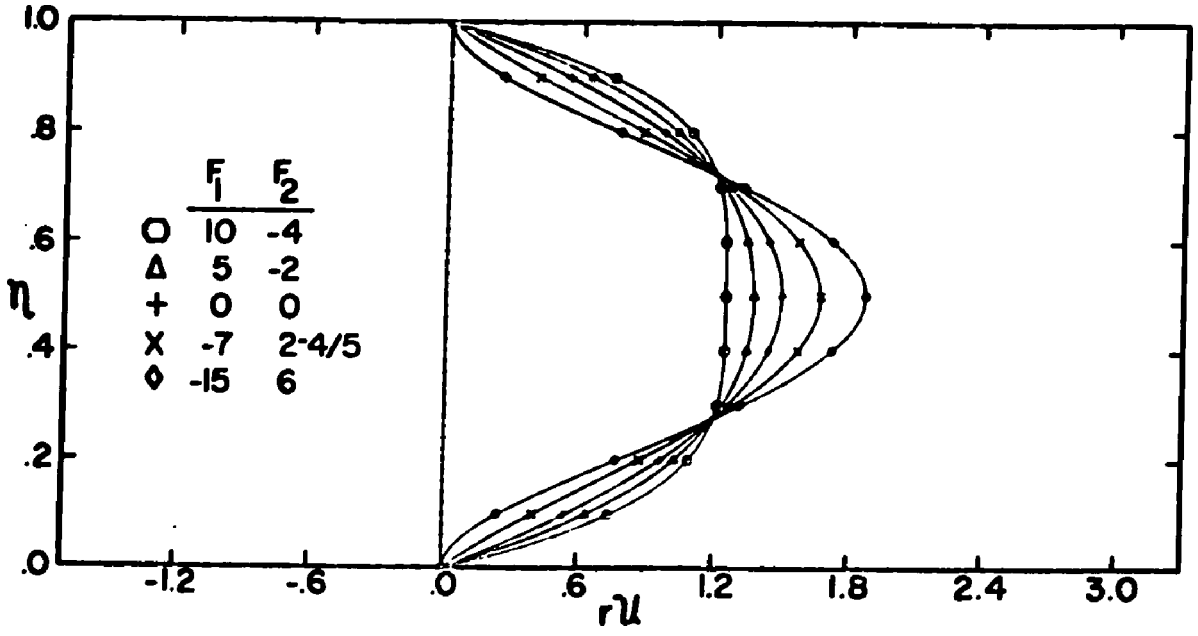


Figure 2-10. Symmetric Velocity Profiles, Two-Parameter Case.

II. Governing Equation

As in the one-parameter case, the Galerkin method of weighted residuals is used to approximate Equation (2-2-a). For the trial solution of Equations (2-18) the weighting functions are H_1 and H_2. To make the governing equation more managable it is assumed that the area ratio is much less than unity, whence Equation (2-2-a) is reduced to

$$\Psi_\eta\left(\frac{1}{\zeta}\Psi_{\eta\zeta}-\Psi_{\eta^2\zeta}\right)+\Psi_\zeta\Psi_{\eta^2}=-\frac{1}{R_{R_0}}\Psi_{\eta^4} \tag{2-21}$$

This result is the same as that found from the first approximation of the perturbation solution of Equation (2-2-a) in terms of the volume perturbation parameter $\epsilon=\sigma^2$. Applying the Galerkin method of weighted residuals to Equation (2-21) over the interval $0\le\eta\le 1$ reduces the first order partial differential equation to the following set of ordinary first order differential equations

$$132F_1+330F_2-2F_1F_2-5F_2^2-\zeta\left[11(6-F_2)F_1^I+(165-3F_1-35F_2)F_2^I\right]=\frac{2772}{R_{R_0}}\zeta(2F_1+5F_2) \tag{2-22-a}$$

$$99+330F_1+837F_2-10F_1F_2-F_1^2-\frac{243}{13}F_2^2-\zeta\left[5(33+F_1-3F_2)F_1^I-(423-5F_1+\frac{729}{13}F_2)F_2^I\right]=\frac{60}{R_{R_0}}\zeta(231F_1+604F_2) \tag{2-22-b}$$

III. Boundary Conditions

The governing equations being of first order require only one boundary condition for a solution. As in the one-parameter case it is assumed that separation always exists at the inlet corner and the reattachment point, i.e.

$$\Psi_{\eta^2}(1,1)=0;\quad \Psi_{\eta^2}(\zeta_{PR},1)=1 \tag{2-23}$$

which is satisfied, according to Equation (2-18-a), if the two free parameters are related by

$$F_1 = 3(1-F_2) \qquad (2\text{-}24)$$

Applying Equation (2-6-b) to the first free parameter, the boundary conditions at the inlet corner are

$$F_1(1) = 3; \quad F_2(1) = 0 \qquad (2\text{-}22\text{-}c)$$

b. Numerical Solution and Discussion of Results

The solution of Equations (2-22) is conveniently presented using the free parameters for the coordinate axes as shown in Figure 2-11. Several lines and points are associated with each particular flow phenomenon:

1) Primary separation point: $F_1 = 3$, $F_2 = 0$
2) Primary reattachment line: $F_1 = 3\,(1-F_2)$
3) Secondary separation line: $F_1 = -(3 + 2\,F_2)$; $F_2 \geq 6$
4) Secondary reattachment line: $F_1 = -(3 + 2\,F_2)$; $F_2 \leq 6$
5) Symmetric velocity profile line: $F_1 = -\frac{5}{2} F_2$
6) Parabolic velocity profile point: $F_1 = 0$, $F_2 = 0$
7) Physically meaningful flows: $F_2 \geq -4$

The flow regimes in the regions between these lines are identified in Figure 2-11. All flows start at the primary separation point (0, 3) characteristic of the flow at the inlet corner and end at the parabolic velocity profile point (0, 0) characteristic of the flow far downstream. The path followed in describing the flow regimes which occur between these limits depends on the diffuser Reynolds number and is referred to as the flow line. The flow line for the one-parameter case lies on the ordinate axis.

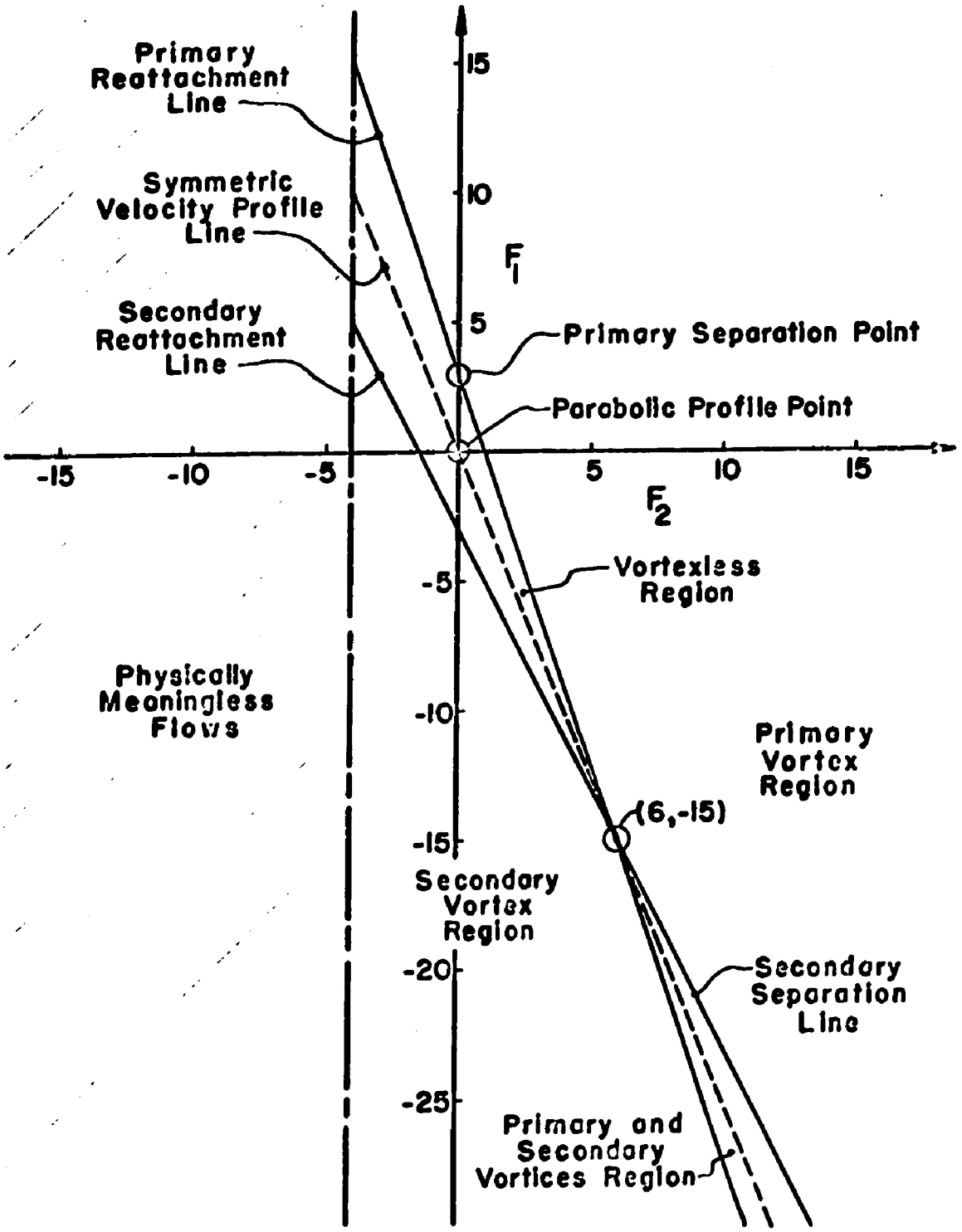


Figure 2-11. Two Parameter Coordinate System.

With two free parameters it is possible for the secondary vortex to form before primary reattachment occurs, in agreement with experimental evidence discussed in the literature survey. If a primary vortex exists the flow line in Figure 2-11 will lie in the primary vortex region after starting at the primary separation point (0,3). The flow reattaches when the flow line intersects the primary reattachment line. However, if the flow line encloses the point (6, - 15), the secondary separation line will be intersected before the primary reattachment line and a secondary vortex will occur upstream of the primary reattachment radius.

Equations (2-22) are solved using the Runge-Kutta numerical integration technique. Results for several different diffuser Reynolds numbers are shown in Figure 2-12. When the diffuser Reynolds number exceeds a value of 246.2 the results become very erratic in the neighborhood of the maximum value of the first free parameter, F_1. This breakdown is thought to be numerical in nature. Several interesting observations can be drawn from Figure 2-12: firstly, the primary reattachment distances are identical with those shown in Figure 2-3 for the second perturbation approximation with an area ratio much less than unity; secondly, the flows downstream of the primary reattachment point become symmetric, asymptotically approaching a parabolic profile far downstream; and finally, no secondary vortex occurs. The second result is also indicated in the literature survey and by the analysis of APPENDIX I. The first and last results are thought to be a consequence of the fact that the form of the general governing differential equation, Equation (2-21), is identical to that used in the one parameter case when the area ratio is much less than unity. The main difference between the results of the one- and two-parameter approaches as presently formulated, then,

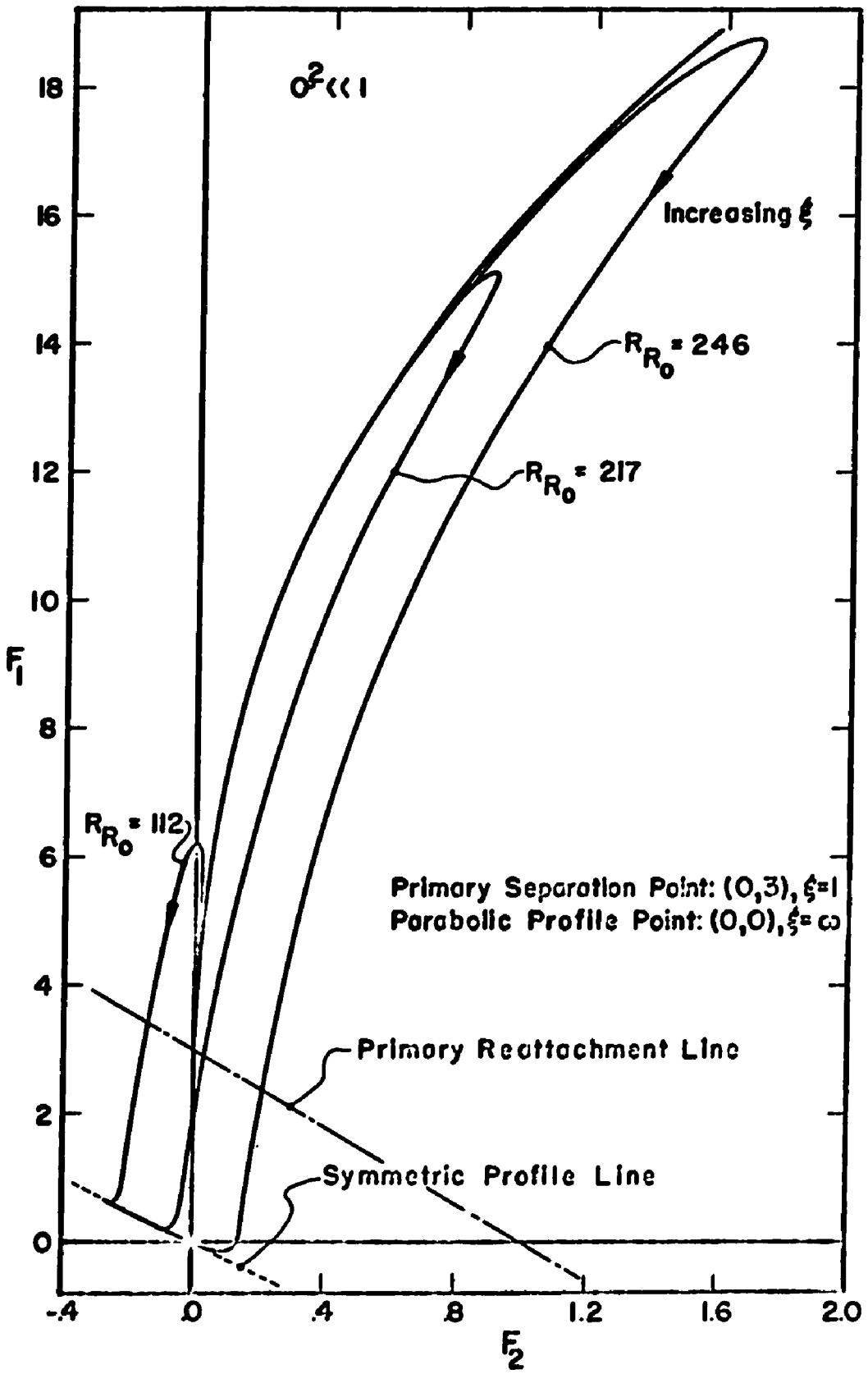


Figure 2-12. Two Parameter Flow Map.

is that the latter can produce non-parabolic symmetric velocity profiles. Evidently, a higher order governing differential equation is required in the two-parameter case if significant departures from the one-parameter approximate solution are desired. This question is open to further investigation.

C. Thermal Field

1. Introduction

The configuration of the thermal field in the radial diffuser is shown in Figure 2-13. The lower surface is maintained at temperature T_1, which is higher than the incoming fluid temperature, T_0. The upper surface is insulated. A thermal boundary layer, δ_T, originates at the stagnation point and develops in the stagnation region. Assuming that $\delta_T < Z_0$, further development occurs in the diffuser region. After δ_T reaches the upper surface the shape of the temperature distribution asymptotically approaches a fully developed profile characterized by a uniform temperature T_1.

In the following analysis the thermal field is approximated using the integral formulation of the energy equation for a thermal boundary layer in the stagnation and development regions and for a developed profile in the downstream region. At the stagnation point the fourth order Kármán-Pohlhausen velocity profile is used. Unfortunately, the stagnation region, other than the stagnation point, is not amenable to analysis because the free stream velocity field is not describable analytically. In the diffuser region, however, the one-parameter profile of Equation (2-5-a) is used to describe the velocity field. The free parameter is evaluated utilizing the second perturbation approximation of Equation (2-11). The thermal boundary layer thickness at the inlet radius is determined experimentally.

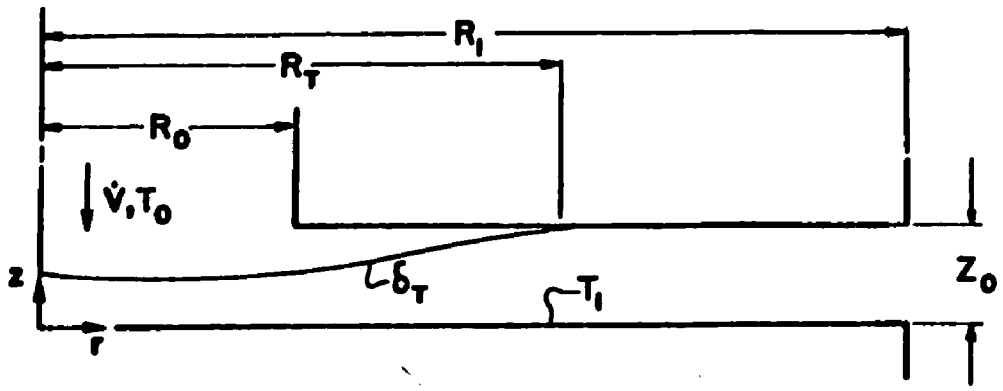


Figure 2-13. Configuration of Thermal Field.

2. General Differential Formulation

Under the assumptions set forth in Section A, the energy equation is

$$u\frac{\partial T}{\partial r} + v\frac{\partial T}{\partial z} = \alpha\left[\frac{1}{r}\frac{\partial}{\partial r}\left(r\frac{\partial T}{\partial r}\right) + \frac{\partial^2 T}{\partial z^2}\right] \qquad (2\text{-}25\text{-}a)$$

where α is the thermal diffusivity. The associated boundary conditions are

$$T(r,0) = T_i\ ; \quad \frac{\partial T}{\partial z}(r, Z_o) = 0 \qquad (2\text{-}25\text{-}b)$$

From Equation (2-25-a) a compatibility condition is found at the lower surface where

$$\frac{\partial^2 T}{\partial z^2}(r,0) = 0 \qquad (2\text{-}25\text{-}c)$$

Substituting for u and v in terms of the stream function, nondimensionalizing, neglecting radial conduction, and setting $\xi = \xi^2$ reduces Equations (2-25) to

$$\psi_\eta \theta_\xi - \psi_\xi \theta_\eta = \frac{1}{Pe}\theta_\eta^2 \qquad (2\text{-}26\text{-}a)$$

$$\theta(\xi,0) = 1\ ; \quad \theta_\eta(\xi,1) = 0\ ; \quad \theta_{\eta^2}(\xi,0) = 0 \qquad (2\text{-}26\text{-}b)$$

where $\theta = (T-T_o)/(T_i-T_o)$ is the dimensionless temperature and $Pe = R_{R_o}P_r$ is the Péclèt modulus.

3. Stagnation Point

a. Formulation

i. Governing Equation and Boundary Conditions

The integral formulation of Equation (2-25-a) for a

boundary layer flow is

$$\frac{1}{r}\frac{\partial}{\partial r}\int_0^{\delta_T} u(T-T_0)r\,dz = -\alpha\left[\frac{\partial T}{\partial z}\right]_{z=0} \qquad (2\text{-}27\text{-}a)$$

with associated boundary and compatibility conditions

$$\begin{aligned} &T(r,0)=T_1\ ;\quad \frac{\partial^2 T}{\partial z^2}(r,0)=0\ ; \\ &T(r,\delta_T)=T_0\ ;\quad \frac{\partial T}{\partial z}(r,\delta_T)=0 \end{aligned} \qquad (2\text{-}27\text{-}b)$$

In dimensionless form Equations (2-27) become

$$\frac{1}{\xi}\frac{\partial}{\partial \xi}\int_0^{\eta_T} u\,\theta\,\xi\,d\eta = -\frac{2}{Pe}\left[\frac{\partial \theta}{\partial \eta}\right]_{\eta=0} \qquad (2\text{-}28\text{-}a)$$

$$\begin{aligned} &\theta(\xi,0)=1;\quad \theta_{\eta^2}(\xi,0)=0\ ; \\ &\theta(\xi,\eta_T)=0\ ;\quad \theta_\eta(\xi,\eta_T)=0 \end{aligned} \qquad (2\text{-}28\text{-}b)$$

where $\eta_T = \delta_T/Z_0$ is the dimensionless thermal boundary layer thickness.

ii. Approximating Function

The temperature field is approximated by a power series expansion in η of the form

$$\theta = \sum_{n=0}^{\infty} b_n \eta^n = b_0 + b_1\eta + b_2\eta^2 + b_3\eta^3 + \cdots\ ;\quad b_i = b_i(\xi) \qquad (2\text{-}29)$$

Truncating the series at the third order term and applying the boundary conditions of Equation (2-28-b) leaves the thermal boundary layer thickness as the only free parameter so that the approximating function for the temperature field becomes

$$\theta = 1 - \frac{3}{2}\tau + \frac{1}{2}\tau^3 \qquad (2\text{-}30)$$

where $\tau = \eta/\eta_T$.

The Nusselt number based on the inlet tube diameter is

$$Nu = \frac{h 2R_0}{k} \tag{2-31}$$

where $h = \dot{q}/(T_i - T_0)$ is the heat transfer coefficient and $\dot{q} = -k\left[\frac{\partial T}{\partial z}\right]_{z=0}$ is the local heat transfer rate per unit area. Substituting h and $\dot{q}$ into equation (2-31) and nondimensionalizing, the Nusselt number becomes

$$Nu = \frac{6}{\sigma \eta_T} \tag{2-32}$$

b. Solution and Discussion of Results

In order to solve Equation (2-28-a) the velocity profile at the stagnation point and its variation near the stagnation point must be approximated. For an invicid axisymmetric stagnation flow the radial variation in the free stream velocity near the stagnation point is given by [43]

$$u = g r \tag{2-33}$$

where g is a constant representing the stagnation point velocity gradient. In dimensionless terms Equation (2-33) becomes

$$U = G\xi \tag{2-34}$$

where $G = g R_0/\bar{u}_{R_0}$ is the dimensionless velocity gradient. The velocity profile is approximated by the fourth order Karman-Pohlhausen distribution [43]

$$\frac{u}{U} = 2v - 2v^3 + v^4 + \frac{\Lambda}{6}(v - 3v^2 + 3v^3 - v^4) \tag{2-35}$$

where $\Lambda = \frac{1}{2} R_{R_0} \eta_v^2 \frac{dU}{d\xi}$ is the shape parameter, $\eta_v = \delta/Z_0$ is the dimensionless viscous boundary layer thickness, and $v = \eta/\eta_v$. At the

stagnation point the shape parameter becomes [43]

$$\Lambda_s = \frac{G}{2} R_{R_\theta} \eta_{v,s}^2 = 4.716 \qquad (2\text{-}36)$$

where the subscript s denotes the stagnation value. The stagnation point boundary layer thickness is then

$$\eta_{v,s} = \frac{3.071}{\sqrt{G R_{R_\theta}}} \qquad (2\text{-}37)$$

Assuming that G and $\eta_{v,s}$ are constant near the stagnation point, a solution for Equation (2-28-a) is found in terms of the boundary layer thickness ratio, $\mathcal{D} = \eta_{v,s}/\eta_{T,s}$. When $\mathcal{D} \geq 1$, the viscous boundary layer is thicker than the thermal one. Thus, Equation (2-28-a) is solved using Equations (2-30), (2-34), (2-35), and (2-36), which gives

$$\mathcal{D}^2 = 4.65 P_r (\mathcal{D} - .906 \mathcal{D}^2 + .164 \mathcal{D}^4) \qquad (2\text{-}38\text{-}a)$$

When $\mathcal{D} < 1$, the viscous boundary layer is thinner than the thermal one. The velocity profile is then described by Equations (2-34), (2-35), and (2-36) for $\eta < \eta_{v,s}$ and by Equation (2-34) alone for $\eta_{v,s} \leq \eta \leq \eta_{T,s}$. Using these equations and Equation (2-30) in Equation (2-28-a) gives

$$\mathcal{D}^2 = 4.65 P_r \left\{ \mathcal{D} - .906 \mathcal{D}^2 + .164 \mathcal{D}^4 + 1.35 \left[1 - \mathcal{D} - .75 (1 - \mathcal{D}^2) + .125 (1 - \mathcal{D}^4) \right] \right\} \qquad (2\text{-}38\text{-}b)$$

From Equations (2-38) it is evident that $\mathcal{D}$ depends on the Prandtl number. For boundary layer flows with no pressure gradients $\mathcal{D}$ is inversely proportional to the Prandtl number [43]. In the present case, however, a pressure gradient does exist and the application of the inverse relationship is questionable. Thus for each particular Prandtl number the appropriate solution equation, Equation (2-38-a)

or (2-38-b), must be determined by trial and error, e.g., for air at 100°F the Prandtl number is .71 and $\mathcal{G}$ is .935 from Equation (2-38-b). The corresponding thermal boundary layer thickness is, from Equation (2-37),

$$\eta_{T,s} = \frac{\eta_{v,s}}{\mathcal{D}} = \frac{3.286}{\sqrt{G R_n}} \qquad (2\text{-}39)$$

and the Nusselt number is, from Equations (2-32) and (2-39),

$$Nu_s = .913\sqrt{\frac{G}{\sigma} Re} \qquad (2\text{-}40)$$

As noted in APPENDIX D, the ratio $\frac{G}{\sigma}$ asymptotically approaches a value of $1/2$ for σ much less than unity for a two-dimensional stagnation flow. Assuming that the same limiting value exists for axisymmetric stagnation flow, Equation (2-40) becomes

$$Nu_s = 1.143\sqrt{Re} \qquad (2\text{-}41)$$

This expression is independent of how the inlet Reynolds number is evaluated because it is based on a uniform invicid velocity distribution where the mean and centerline velocities are identical.

4. Stagnation Region

Within the boundary layer approximation, the energy equation and boundary conditions for the stagnation region are the same as those given by Equations (2-28) for the stagnation point. The temperature and velocity profiles are also the same, being given by Equations (2-30) and (2-35) respectively. The difficulty lies in the fact that the free stream velocity distribution is now a function of the area ratio in a manner similar to the two-dimensional analysis of Appendix D. This analysis cannot be extended to the axisymmetric stagnation region because conformal mapping methods cannot be applied [41].

Other solution techniques exist which could be applied such as graphical and finite difference techniques but neither has an analytical form. Parmet and Saibel [38,39] have found an invicid flow solution for a radial diffuser but the velocity profile in the inlet tube is uniform and the velocity at the inlet corner is infinite.

In order to gain some insight into the flow in the stagnation region, the stagnation region flow of an invicid two-dimensional confined jet is analyzed in APPENDIX D. Similar results should obtain for the axisymmetric stagnation region. The main results are that the free stream velocity along the lower surface is proportional to the radius only near the stagnation point and that the free stream velocity distribution depends on the area ratio, accelerating towards the inlet radius for area ratios less than unity and decelerating otherwise. Correspondingly, the velocity and temperature boundary layer thicknesses must increase or decrease away from the stagnation point, while the Nusselt number must perform in the opposite sense. The latter is important because the Nusselt number at the inlet radius must be known as an initial condition for the solution of the energy equation in the diffuser region, which is considered in the next section.

5. Diffuser Region

a. Formulation

1. Governing Equations and Boundary Conditions

As shown in Figure 2-13, the temperature field in the diffuser region consists of development and downstream regions. To the boundary layer approximation, the governing equation and boundary

conditions for the development region are identical with those of Equations (2-28) for the stagnation point. For the downstream region the governing equation and boundary and compatibility conditions are

$$\frac{1}{\xi}\frac{\partial}{\partial \xi}\int_0^1 u\theta\xi\, d\eta = -\frac{2}{Pe}\left[\frac{\partial\theta}{\partial\eta}\right]_{\eta=0} \qquad (2\text{-}42\text{-}a)$$

$$\theta(\xi,0) = 1;\quad \theta_\eta(\xi,1) = 0;\quad \theta_{\eta^2}(\xi,0) = 0 \qquad (2\text{-}42\text{-}b)$$

II. Approximating Functions

The approximating function for the temperature field in the development region is given by Equation (2-30). The development region ends when the thermal boundary layer thickness reaches the upper surface, which occurs at radius R_T. The temperature profiles of the development and downstream regions must coincide at this point. Truncating the approximating function of Equation (2-29) at the third order term and applying the preceding condition and the boundary conditions of Equations (2-42-b) leaves one free parameter, E, so that the approximating function for the downstream temperature field becomes

$$\theta = 1 - \tfrac{1}{2}(3\eta - \eta^3)E;\quad E = E(\xi);\quad E(\xi_T) = 1 \qquad (2\text{-}43)$$

The Nusselt number based on the inlet tube diameter is given by Equation (2-32) for the development region and by

$$Nu = \frac{6}{\sigma}E \qquad (2\text{-}44)$$

for the downstream region.

b. Solution and Discussion of Results

In the diffuser region the effect of viscosity is

felt everywhere so the velocity field cannot be treated as a boundary layer phenomenon. Instead, the one-parameter velocity field of Equation (2-5-a) is used. Substitution of this equation and Equation (2-30) into Equation (2-28-a) and transforming the radial coordinate to $\xi = \xi^2$ gives the governing energy equation for the development region as

$$\eta_T^I = \frac{\frac{210}{Pe} - (28 - 35\eta_T + 12\eta_T^2)\eta_T^3 F^I}{\left[168 - 105\eta_T + (56 - 105\eta_T + 48\eta_T^2)F\right]\eta_T^2} \qquad (2\text{-}44\text{-a})$$

subject to the condition that the initial value $\eta_T(1)$ is known. Substitution of Equations (2-5-a) and (2-43) into Equation (2-42-a) gives the governing energy equation for the downstream region as

$$E = exp\left\{\int_{\xi_T}^{\xi} \frac{\frac{210}{Pe} - 5F^I}{5F - 91}\, d\xi\right\} \qquad (2\text{-}44\text{-b})$$

where ξ_T follows from the solution of Equation (2-44-a) as the radial position where η_T reaches a value of unity in the development region.

The solution of Equations (2-44) requires that the initial thermal boundary layer thickness, η_1, have a known value. Since a theoretical value is unattainable, the only alternative is to use an experimentally determined value. This is done in Figure 3-16, which is presented later, for an area ratio of 0.245 and air as the fluid with the free parameter evaluated using Equations (2-11). Equations (2-44) are solved using a simple numerical integration. The solutions are discussed further in Section c of CHAPTER III.

According to Equation (2-43), the free parameter E must approach a value of zero far downstream because the temperature profile asymptotically becomes uniform. Consequently, the Nusselt number must approach zero far downstream from Equation (2-44). Actually, the possibility exists that natural convection effects not included in the theoretical analysis may interfere with the establishment of the uniform asymptotic temperature distribution because the average flow rate in the diffuser region is inversely proportional to the radius. This effect should appear only at very low inlet flow rates and/or for diffusers with a large exit to inlet radius ratio.

The effect of the primary vortex on the thermal boundary layer development is shown in Figures 2-14 and 2-15 for the two higher flow rates considered in Figure 3-16. The one-parameter approximation of the flow field given by Equations (2-4) is used with the free parameter evaluated according to the second perturbation approximation of Equations (2-11). For comparison, the growth of the thermal boundary layer thickness, η_T, for a parabolic velocity profile is also shown. The free boundary of the primary vortex is defined by the separation streamline, $\psi=1$, as in Figure 2-1 above. The axial position of the separation streamline, η_p, is a function of the free parameter and is evaluated from Equation (A-6) with F_2 set equal to zero. The thermal boundary layer growth with a primary vortex present differs significantly from that with a parabolic velocity profile: the initial growth of the thermal boundary layer thickness is slower but the thermal boundary layer reaches the upper surface sooner.

The primary vortex, in the above cases, always lies in the isothermal region outside of the thermal boundary layer. It is

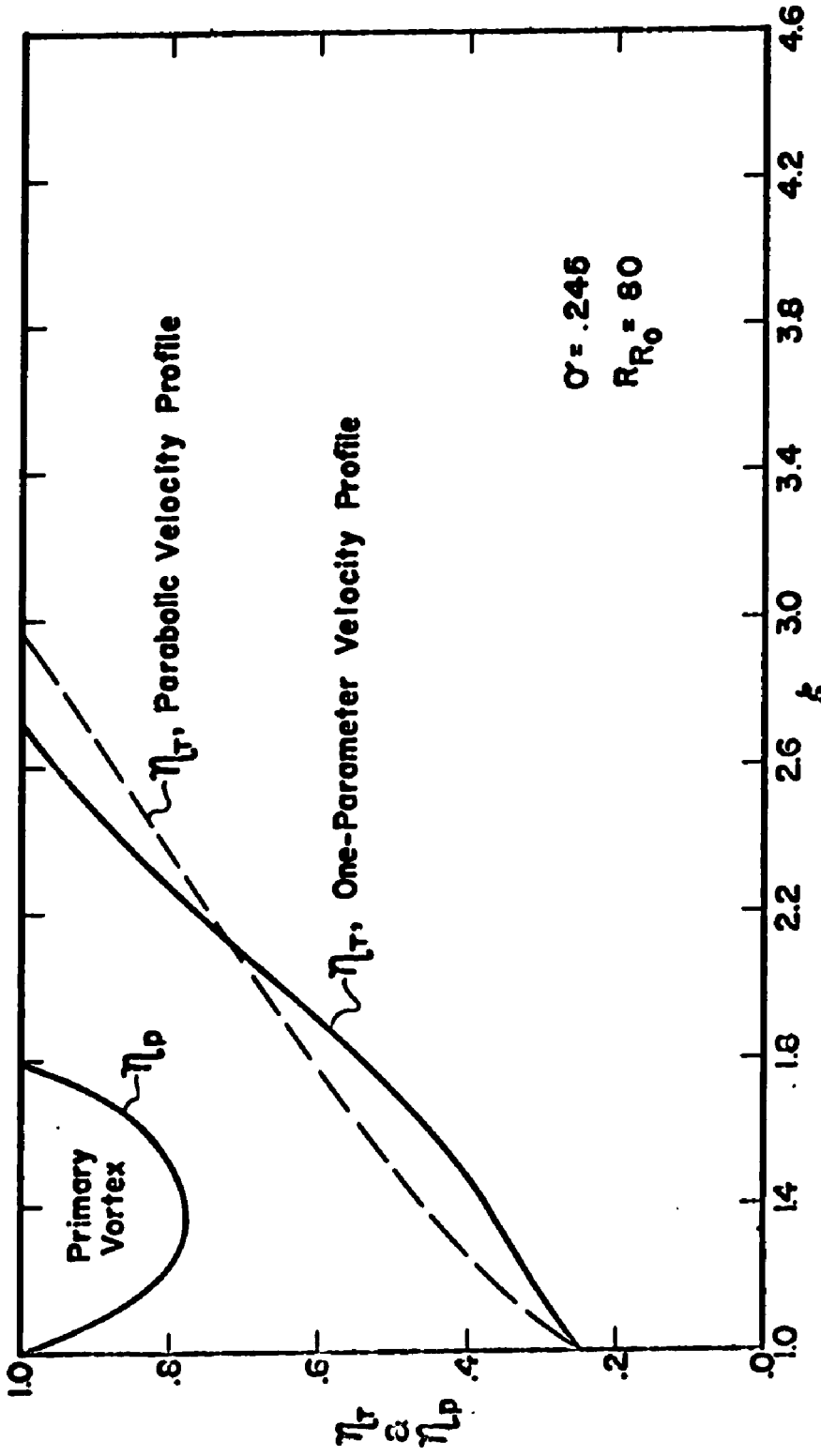


Figure 2-14. Thermal Boundary Layer Growth.

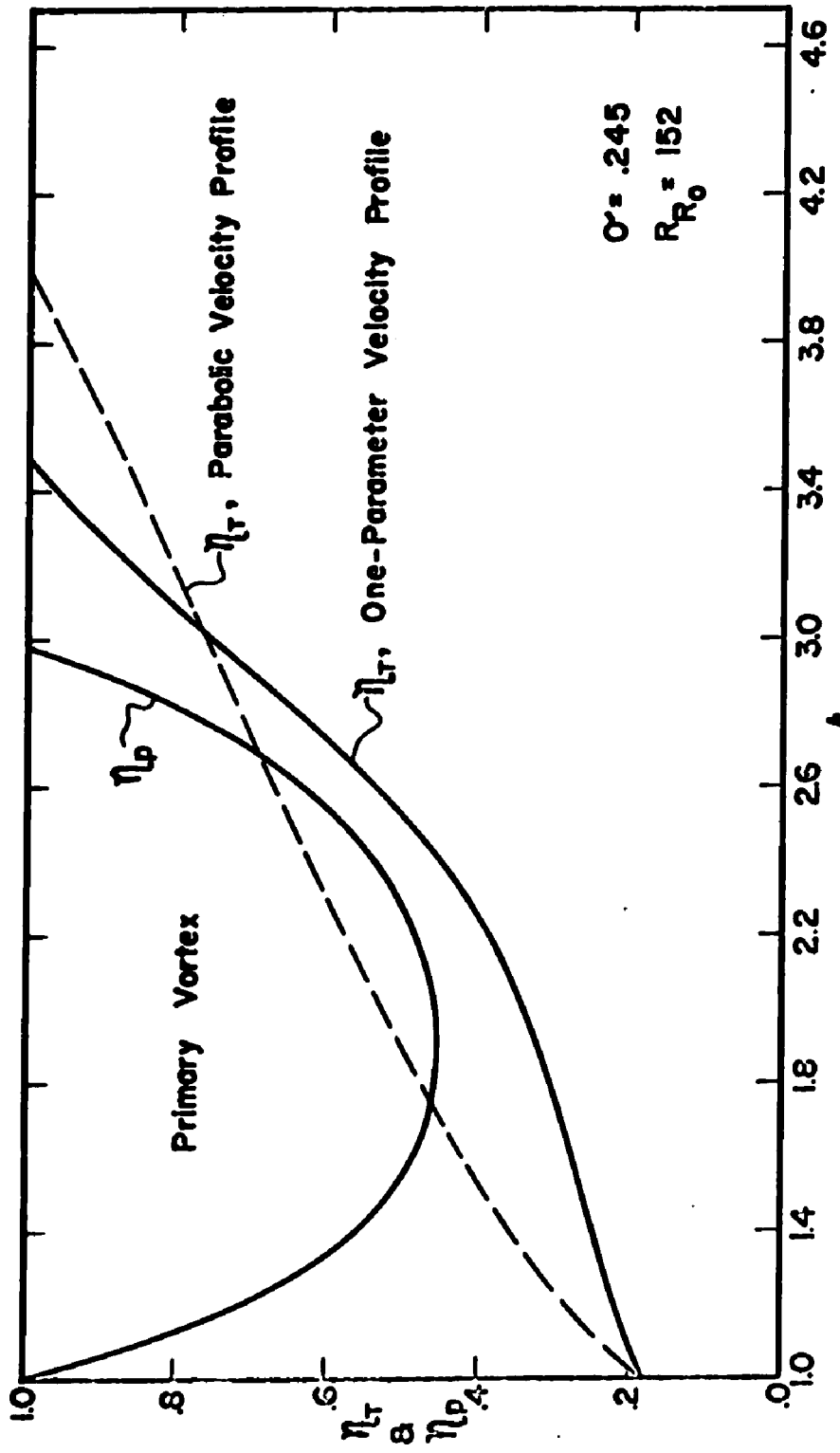


Figure 2-15. Thermal Boundary Layer Growth.

conceivable that, if the Prandtl number became much smaller than the value for air used in this study, the thermal boundary layer could enter the primary vortex. In such an event the present analysis would no longer be applicable because no provision has been made to accommodate the convective heat transfer which would occur in the vortex and between the vortex and the incoming flow. This analysis is therefore limited to fluids having a Prandtl number of the order of unity or greater for the range of geometric parameters investigated.

CHAPTER III

EXPERIMENTAL INVESTIGATION

A. Introduction

Separate experimental investigations were conducted for the flow and heat transfer phenomena in a radial diffuser. Consequently, the following sections deal with each investigation individually. In both cases air was the working fluid and was considered to be incompressible because the Mach number of the inlet flow never exceeded a value of 0.07.

B. Flow

The flow investigation involved applying flow visualization techniques to reveal the nature of the flow field in the diffuser region. This study was accomplished in part by Sherba [45].

1. Apparatus

A schematic diagram of the flow apparatus is shown in Figure 3-1. The rectangular upper and lower plates and the inlet tube are made of Plexiglass. The gap between the surfaces is adjusted using the adjustment screws. A ruler was used to set the gap and check parallelism. The flow rate is measured using a Brooks rotameter. The smoke generator used for the flow visualization is similar to that built by Blankenship [4] and is shown schematically in Figure 3-2. The smoke is introduced through the

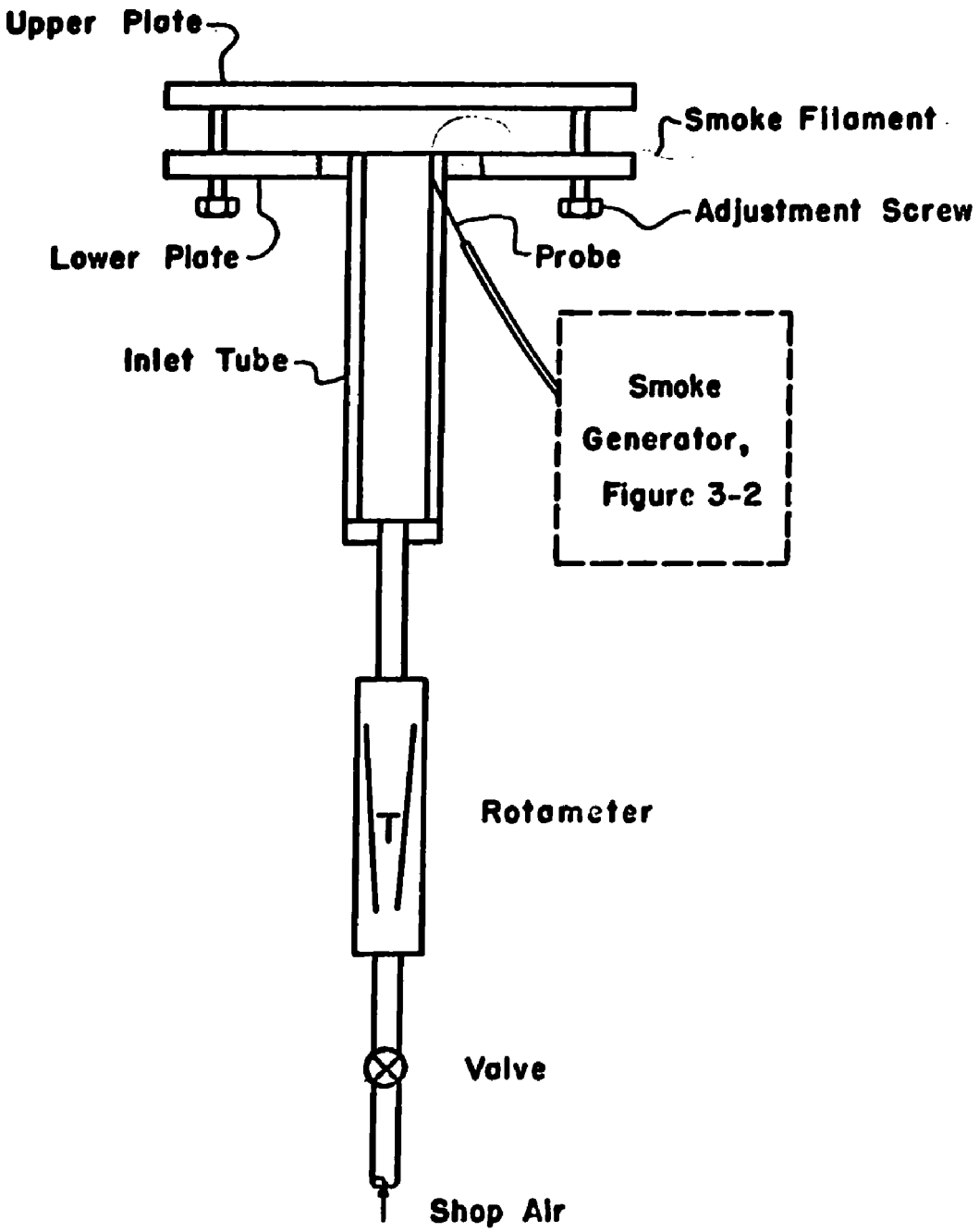


Figure 3-1. Schematic of Flow Apparatus.

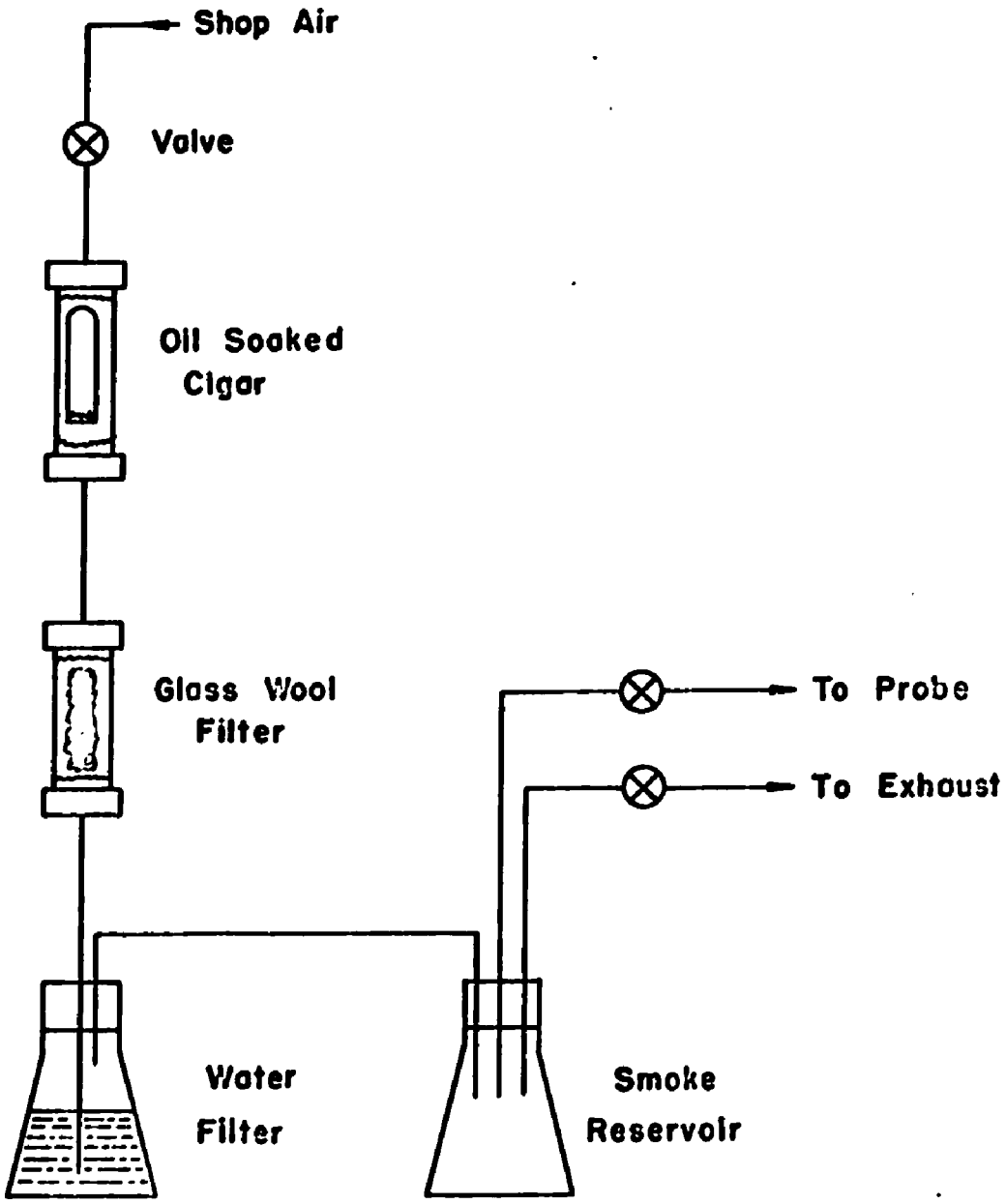


Figure 3-2. Schematic of Smoke Generator.

wall of the inlet tube upstream of the inlet corner via a length of .020 inch I.D. hypodermic tubing. The smoke flow rate is maintained at a level low enough that the smoke filament remains near the inside surface of the tube, becoming the separation streamline downstream of the inlet corner. A low voltage high intensity lamp is used to illuminate the smoke filament in the gap. All tests were run with the apparatus in a closed chamber for protection against drafts.

2. Procedure

For each of three different gap settings, the smoke filament was photographed for several different laminar flow rates. All photographs were taken with a Graphic camera using Polaroid Land Type 47 film (ASA 3000). The plane containing the smoke filament is referenced by two thin axial wires which are located on a common diametral line and cross the gap on either side of and far downstream from the inlet hole. This arrangement ensures that the focal plane of the camera coincides with that of the smoke filament and also provides the gap position for the subsequent analysis of the photographs. The photographs were taken within five minutes of the establishment of the smoke filament because smoke from the filament steadily diffuses into the primary vortex and obscures the filament.

3. Property Evaluation and Data Reduction

The inlet and diffuser Reynolds numbers were calculated for each photograph taken. Properties were evaluated at atmospheric temperature and pressure. The reattachment distance and maximum thickness of the primary vortex were scaled from each photograph. The scale factor between the dimensions in the photograph and the actual

dimensions was determined by measuring the outside diameter of the inlet tube.

4. Results and Comparison with Theoretical Analysis

The experimental data for the reattachment distance and maximum thickness of the primary vortex are presented in dimensionless form in Figures 3-3 and 3-4, respectively. The area ratio ranged from .75 to 1.88 and the inlet Reynolds number from 193 to 1422. Similar data taken from the photographs of McGinn [33] are also shown. The data correlate well with the diffuser Reynolds number, although there are systematic deviations which may be caused by the area ratio and which are especially evident in the data for the primary vortex thickness. The experimental data coincide fairly well with the theoretical distributions which are also shown in Figures 3-3 and 3-4. The latter are based on a one-parameter velocity field with the free parameter evaluated from the second perturbation solution, Equations (2-11), for area ratios much less than unity and from the numerical solution of Equations (2-12) for an area ratio of 1.15.

The smoke filament is very stable except at higher laminar flow rates where the filament disperses suddenly near the primary reattachment radius. The inlet Reynolds number at which this phenomenon occurs agrees with that found by McGinn [32] to produce transition to turbulent flow downstream of the secondary separation point which is given by Equation (1-2).

The circulation within the primary vortex was revealed by introducing smoke directly into the vortex. A secondary separation point was also observed visually although its reattachment could not be identified because the upper and lower surfaces of the diffuser region are rectangular resulting in asymmetric flow conditions far

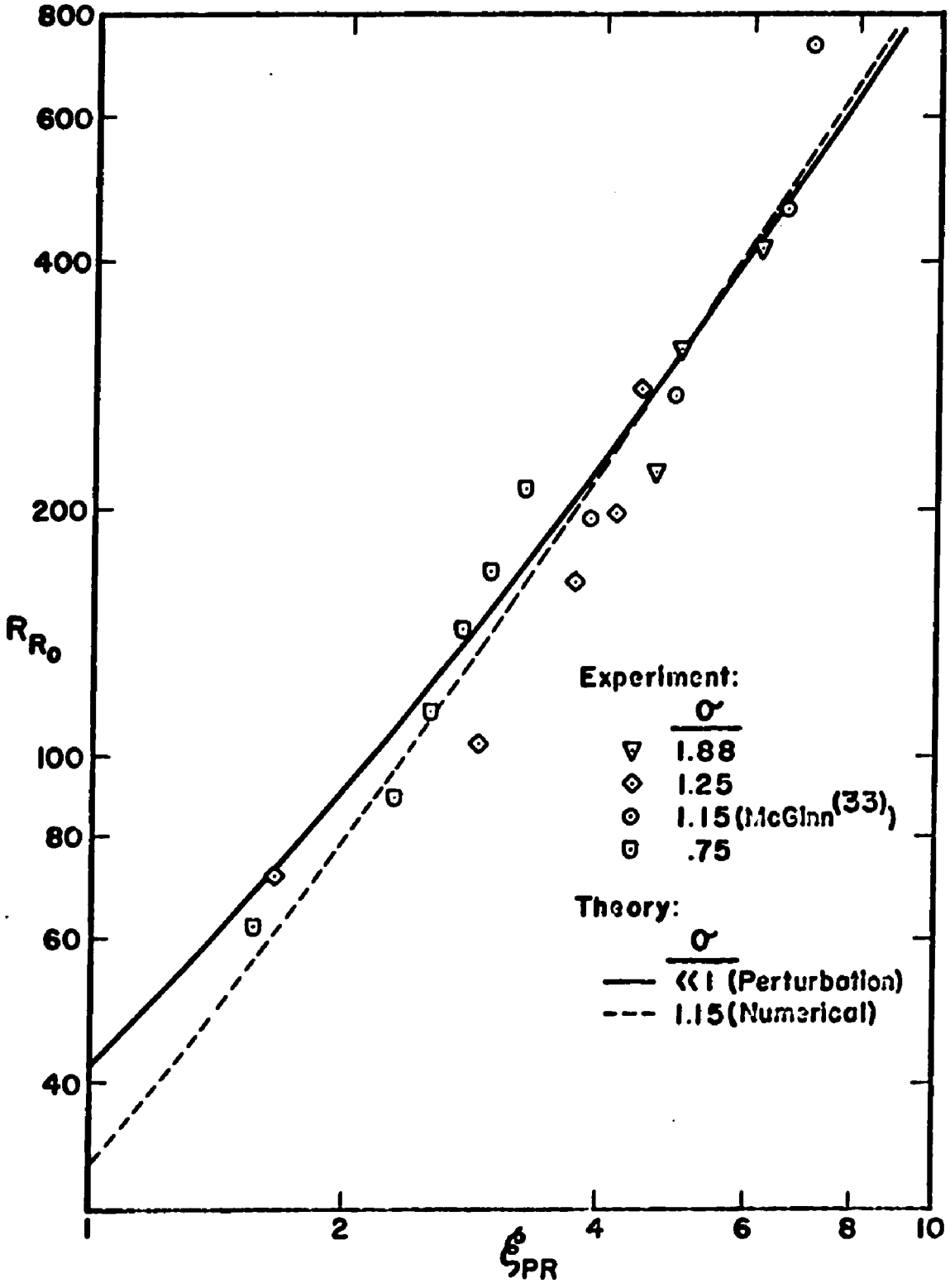


Figure 3-3. Primary Reattachment Radius vs Diffuser Reynolds Number.

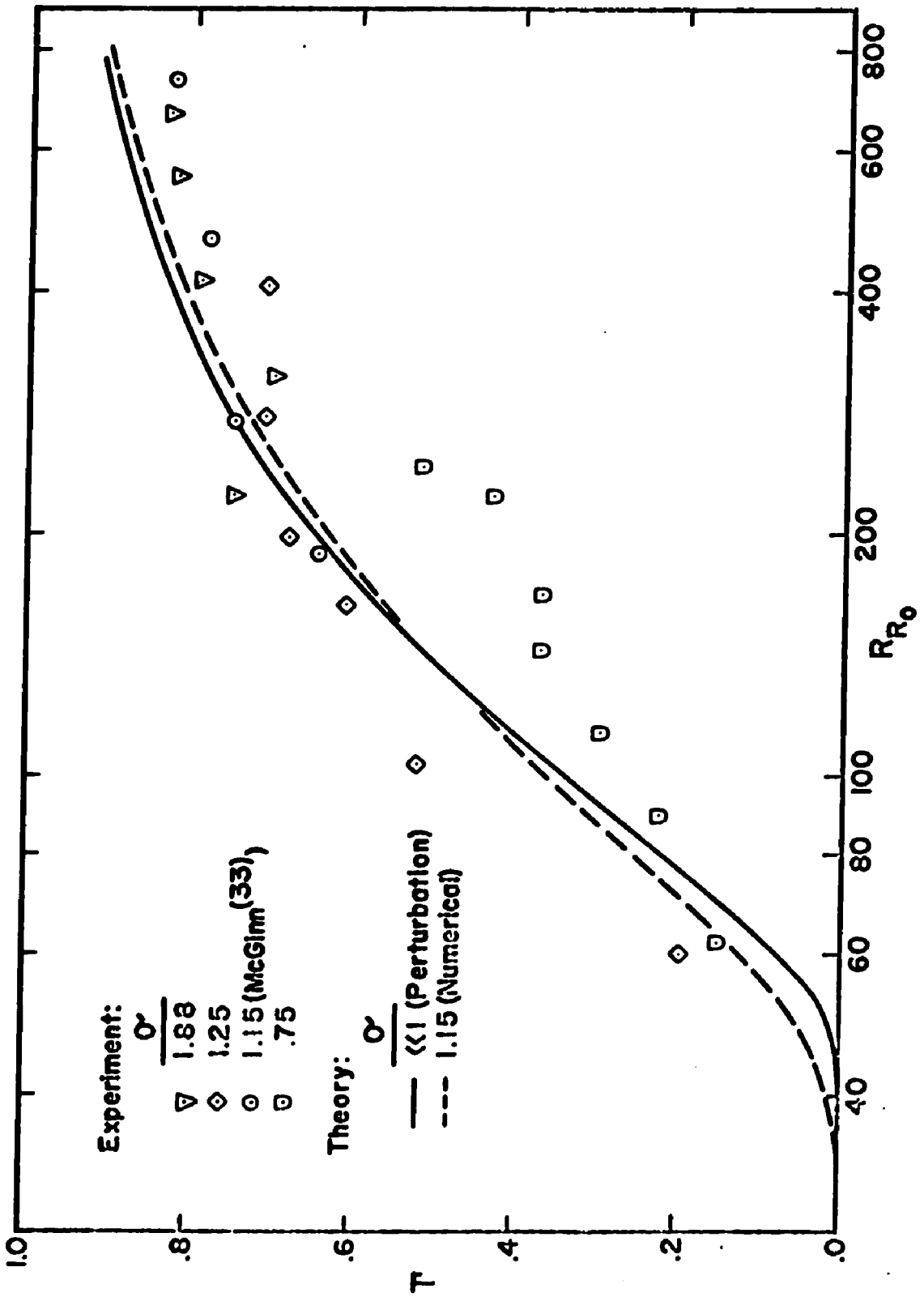


Figure 3-4. Primary Vortex Thickness vs Diffuser Reynolds Number.

downstream.

5. Experimental Uncertainty

If a quantity Q is evaluated from measured quantities by some functional relationship

$$Q = Q(q_1, q_2, q_3, \cdots q_i, \cdots)$$

then the uncertainty in Q is related to the uncertainties associated with the measured quantities by (9)

$$\Delta Q = \left(\sum_{i=1}^{n} \left[\frac{\partial Q_i}{\partial q_i} \Delta q_i \right]^2 \right)^{\frac{1}{2}} \qquad (3\text{-}1)$$

where Δ denotes the uncertainty of a quantity.

The greatest uncertainty in determining the inlet Reynolds number, Re, lies in determining the flow rate. The accuracy of the Brooks rotameter is 2% of full scale or .0446 SCFM. The flowmeter is, therefore, most accurate for high flow rates. The uncertainty associated with the inlet Reynolds number using Equation (3-1) approaches $\pm$ 7.0% for the high flow rates but increases to $\pm$ 30% at the low flow rates.

The maximum uncertainty in the measurement of the inlet radius, R_o, and the spacing between the surfaces, Z_o, is $\pm$ .001 in. and $\pm$ .005 in., respectively. The uncertainty in the area ratio, σ, varied from $\pm$ 2.7% for close spacings to $\pm$ 1.1% for large spacings.

The greatest uncertainty in determining the dimensionless reattachment radius, ξ_{PR}, is in estimating its dimensional counterpart, R_{PR}, in the photographs. The maximum uncertainty expected for the latter measurement is $\pm$ .050 in. The uncertainty in ξ_{PR} varies from $\pm$ .68% for the longest reattachment radius to $\pm$ 6.7% for the shortest one.

The uncertainty in the measurement of the maximum primary

vortex thickness, t, is $\pm$ .005 in. The corresponding uncertainty in the dimensionless maximum primary vortex thickness, T, varies from $\pm$ 5.9% to $\pm$ 18% for the smallest spacing and from $\pm$ 1.8% to $\pm$ 1.9% for the largest spacing.

Most length measurements were made with an engineering scale with graduations of .020 in.

C. Heat Transfer

1. Apparatus

A schematic diagram of the heat transfer apparatus is shown in Figure 3-5. It consists of supply, flow metering, and test sections, each of which is discussed individually in the following paragraphs. A photograph of the apparatus is shown in Figure 3-6. All temperatures were measured using 30 gauge copper-constantan thermocouples read by a Leeds and Northrup 8662 precision potentiometer.

In the supply section compressed shop air at 90 to 100 psia is admitted to the apparatus by the master valve and run through a pressure regulator followed by a filter and water trap.

The pressure in the metering section is usually maintained at 5 psia by a Fairchild Hiller precision pressure regulator. The flow rate is measured using a set of three complementary Brooks rotameters whose combined capacities vary from 0.014 to 18 SCFM. The temperature and pressure of the flow are measured downstream of the rotameter. The flow rate is controlled by a needle valve.

Details of the test section are shown in Figure 3-7. A photograph of the test section is shown in Figure 3-8. The inlet tube is a 0.490 inch I.D. seamless steel tube 122.4 diameters long,

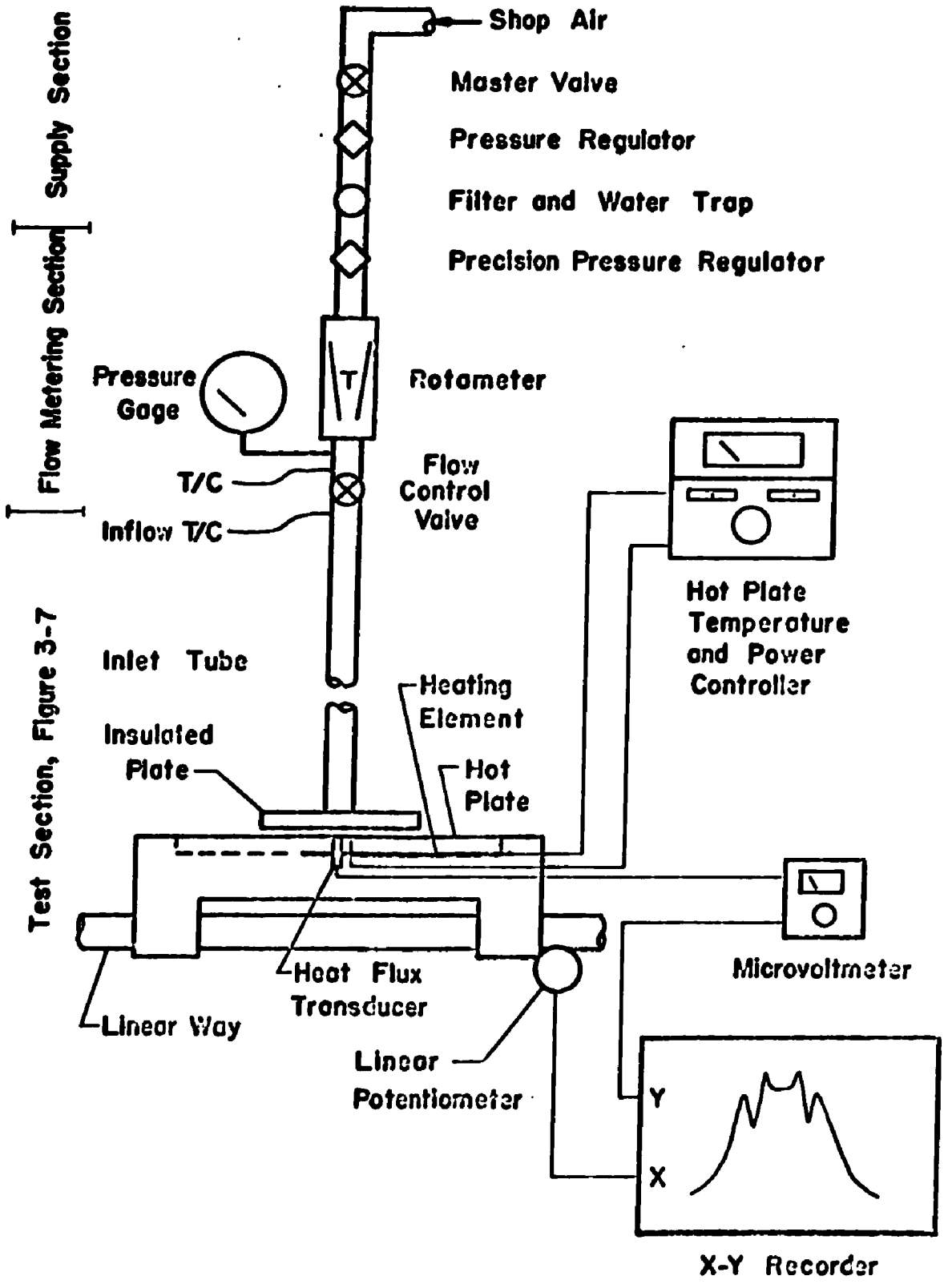


Figure 3-5. Schematic of Heat Transfer Apparatus.

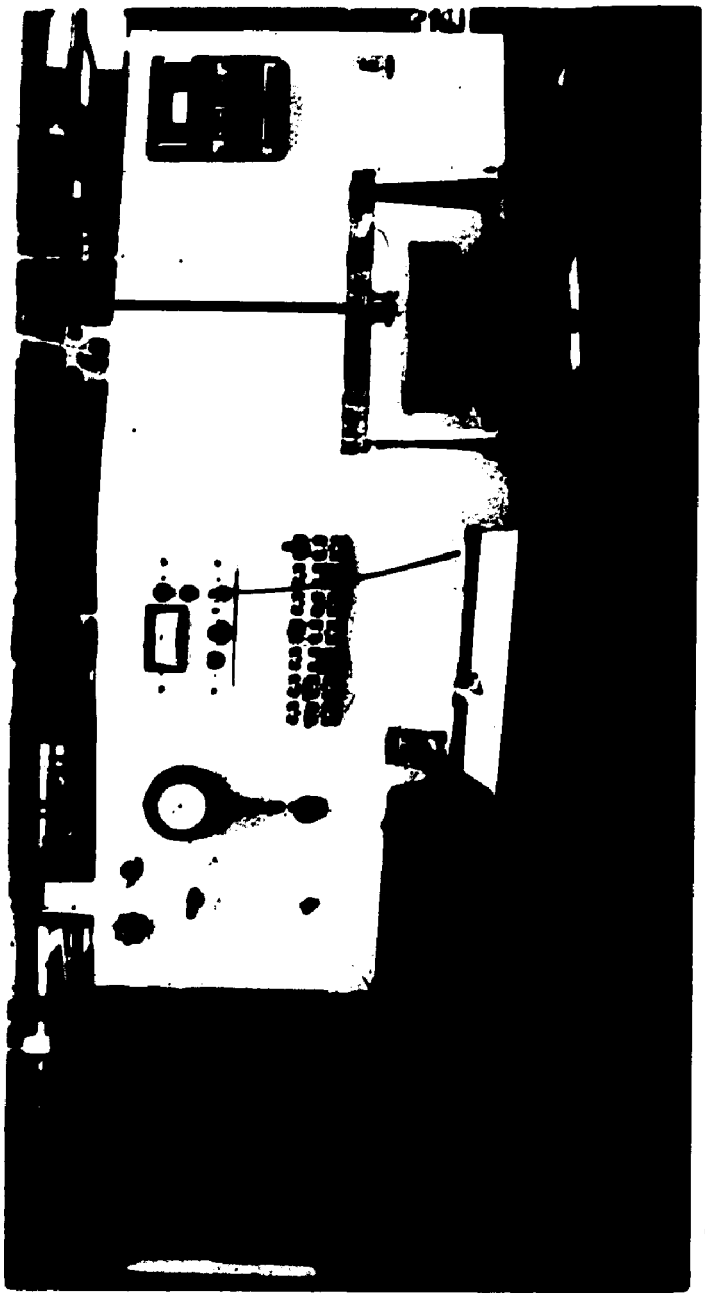


Figure 3-6. Photograph of Heat Transfer Apparatus.

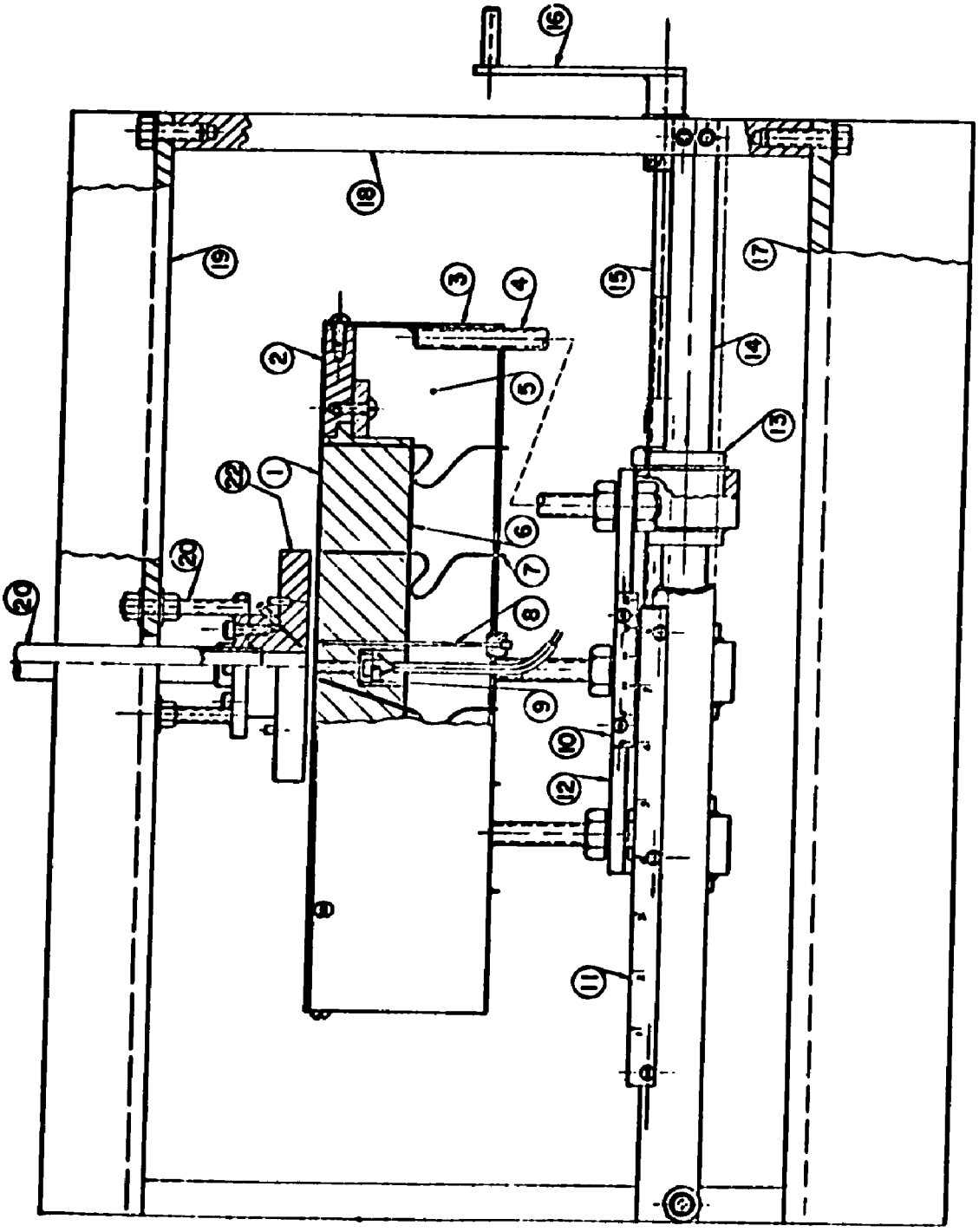


Figure 3-7. Detail Drawing of Test Section.

TABLE 3-I

TEST SECTION COMPONENTS

PART NO.	DESCRIPTION
1	Hot Plate
2	Hot Plate Support Disk
3	Hot Plate Housing
4	Hot Plate Assembly Adjustment Bolts
5	Insulation
6	Heater
7	Thermocouples
8	Pressure Tap
9	Heat Flux Transducer
10	Vernier Plate
11	Scale
12	Hot Plate Assembly Support Plate
13	Linear Ball Bearing
14	Linear Way
15	Positioning Screw
16	Crank Arm
17	Lower Support Frame
18	Uprights
19	Upper Support Frame
20	Inlet Tube
21	Upper Disk Adjustment Bolt
22	Upper Disk

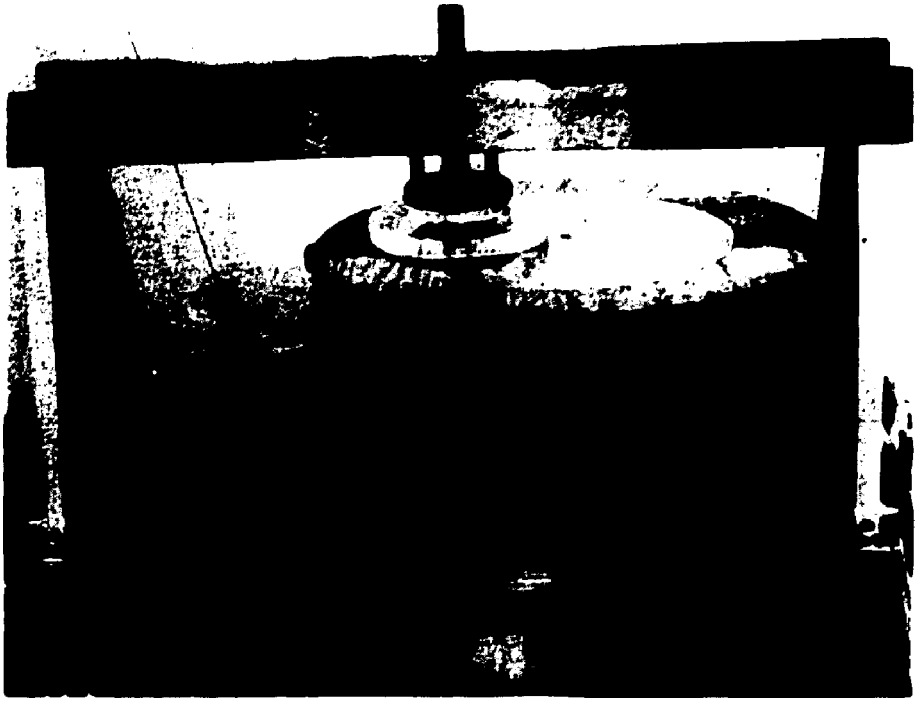


Figure 3-8. Photograph of Test Section.

a length sufficient to allow the velocity distribution to become swirlfree and fully developed for both turbulent and laminar flows [43], thus establishing a well defined velocity profile. Actually, the velocity profile is expected to be somewhat flatter than the fully developed profile near the end of the inlet tube because of the presence of the radial diffuser. The temperature of the inlet flow is measured slightly upstream of the inlet tube. The inlet tube is joined to the upper disk which is made of Plexiglass 4-1/4 inches O.D. The spacing is adjusted by moving the resulting unit vertically using the three adjustment screws. The hot plate is constructed of commercially pure aluminum 1-1/2 inches thick and 8 inches O.D. The thickness and high conductivity of this material ensure that the surface of the hot plate is nominally isothermal for the purposes of this study. A special Watlow electric resistance heater is bonded to the rear surface of the hot plate. The heater consists of small nichrome wires distributed to give a uniform heat flux and sandwiched between two layers of fiberglass cloth impregnated with silicone rubber. The resistance of the heater is about 12 ohms. Five thermocouples are distributed along a common diameter of the hot plate. The thermocouple junctions are placed within 1/32 inch of the surface. The leads of the thermocouples are glued to the heater before leaving the support housing to reduce conduction losses which might affect the thermocouple readings. The hot plate temperature was maintained at about 120°F using a Research Incorporated proportional temperature and power controller with a digital set point. The centermost thermocouple provides the feedback signal. At the center of the hot plate a foil type heat flux transducer similar to that of Gardon [13] is mounted flush with the surface. Although the transducer measures

the total heat transfer rate caused by radiation and convection the contribution of the former is negligible because of the small temperature difference between the hot plate and the surroundings - typically 40°F. The active diameter of the transducer is only 0.040 inch, consequently the transducer effectively measures the local heat transfer rate. The output of the transducer is on the order of 10 microvolts and is measured using a Keithley microvolt-ammeter. The hot plate is attached to the support housing by an insulating ring of five-ply plywood. Glass wool insulation fills the space between the hot plate and the support housing. The housing is mounted on a linear carrier actuated by a positioning screw. The upper disk is centered on a line through the heat flux transducer. In this way the heat flux transducer can be positioned along a diameter relative to the upper disk, thus measuring the local heat transfer rate. The position of the transducer is measured using either a vernier scale or a Humphrey 1500 ohm 6-1/2 inches stroke linear potentiometer. The outputs of the microvolt-ammeter and the potentiometer are fed to a Moseley X-Y recorder, thereby producing a complete record of the local heat transfer rate versus position. For these plots the carrier was driven at a speed of about 2-1/2 feet per hour by an electric gear motor driving the positioning screw. At this speed the results were identical for traverses made in opposite directions all other conditions being constant.

2. Procedure

For each of three different plate separations traverses were made for several different flow rates in both the laminar and turbulent regimes. A plot of the heat flux transducer output versus position was produced for each flow rate. The zero reference point

of the heat flux transducer is determined by placing a hollow aluminum cap over the active surface of the transducer, thus forming an isothermal enclosure with which no heat transfer occurs. The residual signal of about 1 microvolt is magnetically induced by ac machinery and power lines. When the gap is large enough to admit the cap the transducer zero is established before and after each traverse, otherwise it is established before and after every second traverse. The traverses are made from the outside edge to the center and vice versa for sequential flow rates. During each traverse the temperature is maintained within $\pm$ 0.15°F of the set point value. The hot plate, inlet air, and metered air temperatures are read at the beginning and end of each traverse. The average value is used in subsequent calculations. The flow rate and metered air pressure are read at the beginning of each traverse. The atmospheric pressure was determined at the end of each set of traverses.

Some studies were made of the stagnation point heat transfer rates in which case the above procedure was followed with no traverse.

3. Property Evaluation and Data Reduction

The inlet and diffuser Reynolds numbers were evaluated for each traverse based on the dynamic viscosity at the average film temperature, $T_f = (\bar{T}_o + \bar{T}_i)/2$, and the density at the inlet flow temperature, $\bar{T}_o$. The local heat transfer rate, $\dot{q}$, is calculated from the heat flux transducer output, e, in microvolts according to

$$\dot{q} = \frac{e}{17.77} \qquad \text{(Btu/ft.}^2\text{ - sec.)} \qquad (3\text{-}2)$$

which was derived from the calibration data for the heat flux transducer.

The Nusselt number based on the inlet diameter is

$$Nu = \frac{\dot{q}\,2R_o}{k\,\Delta T} \qquad (3\text{-}3)$$

where k is the thermal conductivity of the fluid at the film temperature and $\Delta T = \bar{T}_i - T_o$ is the temperature difference between the heated surface and the incoming fluid.

4. Results and Comparison with Analysis

Experiments were conducted for turbulent as well as laminar inflows. The area ratio usually ranged from .245 to 2.04 and the inlet Reynolds number from 15 to 53,300.

Plots of the heat flux transducer output versus radial position are shown in Figures 3-9, 3-10, and 3-11 for decreasing values of the area ratio. Plots for laminar and turbulent inlet flows occupy the left and right hand sides of each figure, respectively. The plots show a nominally 0.15 microvolt a-c signal superimposed on the main output signal. The a-c signal is generated by the firing of the SCR's in the power controller for the heater. Since the proximity of the heat flux transducer to the heater nullified attempts to eliminate the noise signal, the average value of the transducer output is used in subsequent calculations. Table 3-2 lists the information necessary to calculate the Nusselt number using Equations (3-2) and (3-3). In the following discussion the heat transfer phenomena at the stagnation point and in the stagnation and diffuser regions are considered individually.

a. Stagnation Point

Data for the stagnation point heat transfer rate versus flow rate are shown in Figure 3-12 for three different area ratios. The area ratio was varied by adjusting the spacing between the upper and lower surfaces. The data correlate well with the inlet

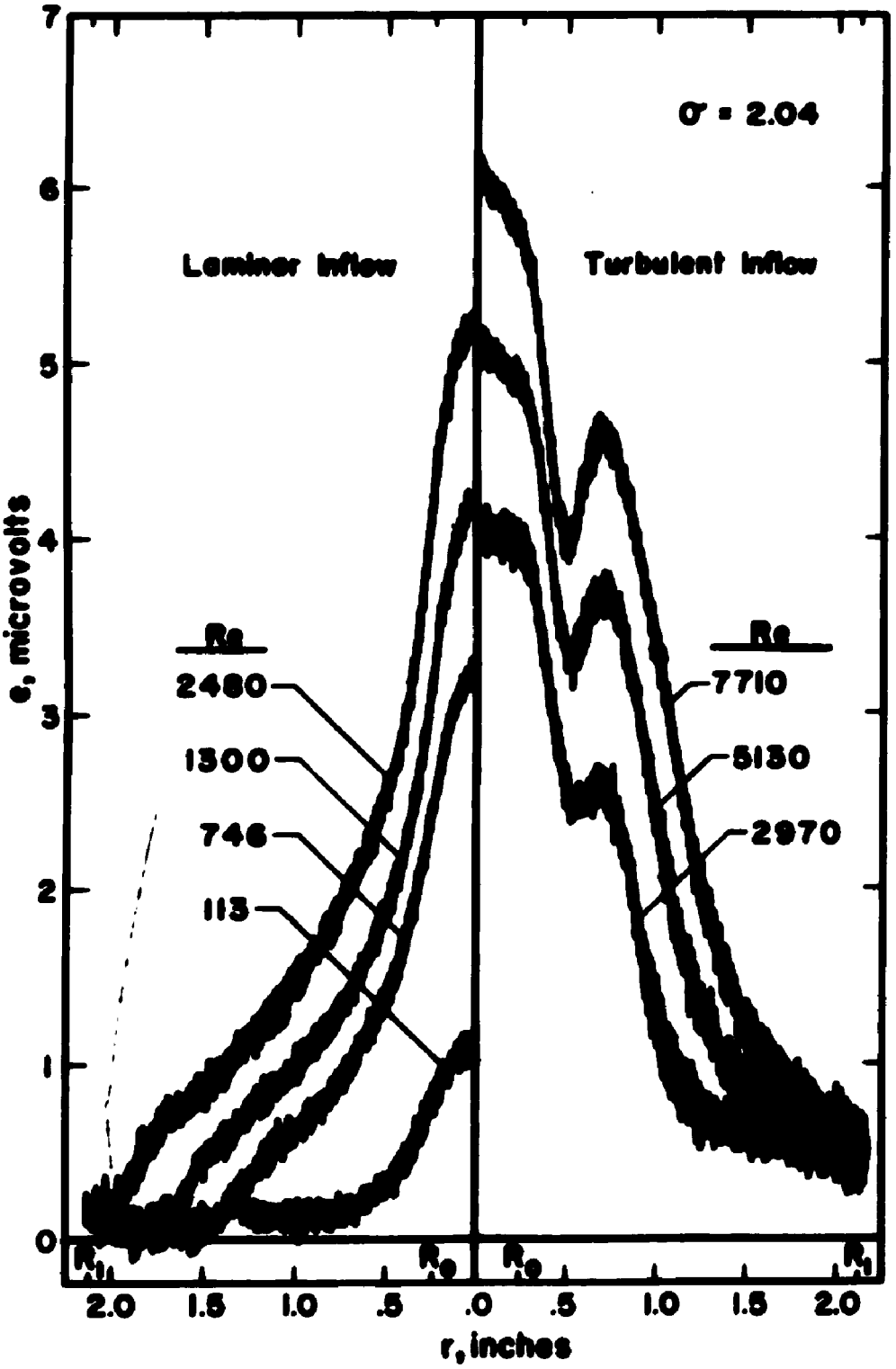


Figure 3-9. Heat Flux Distributions.

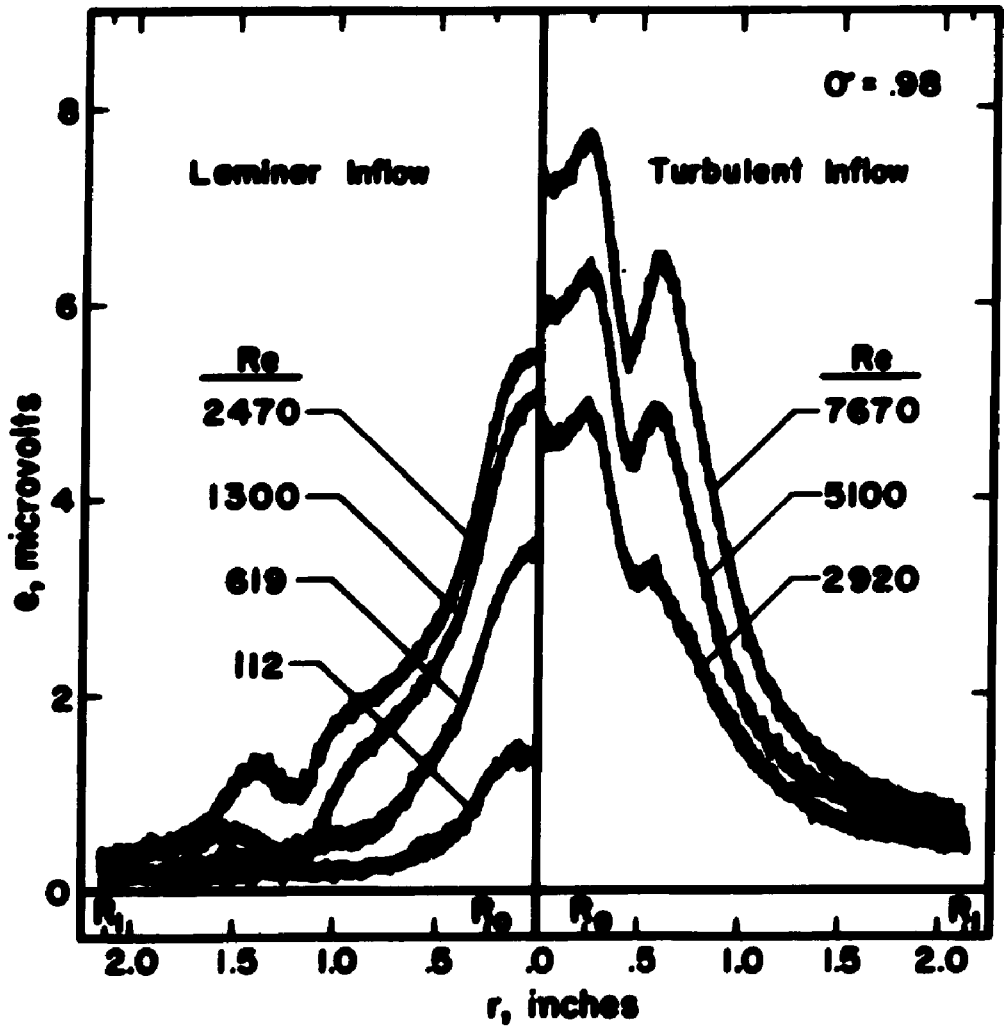


Figure 3-10. Heat Flux Distributions.

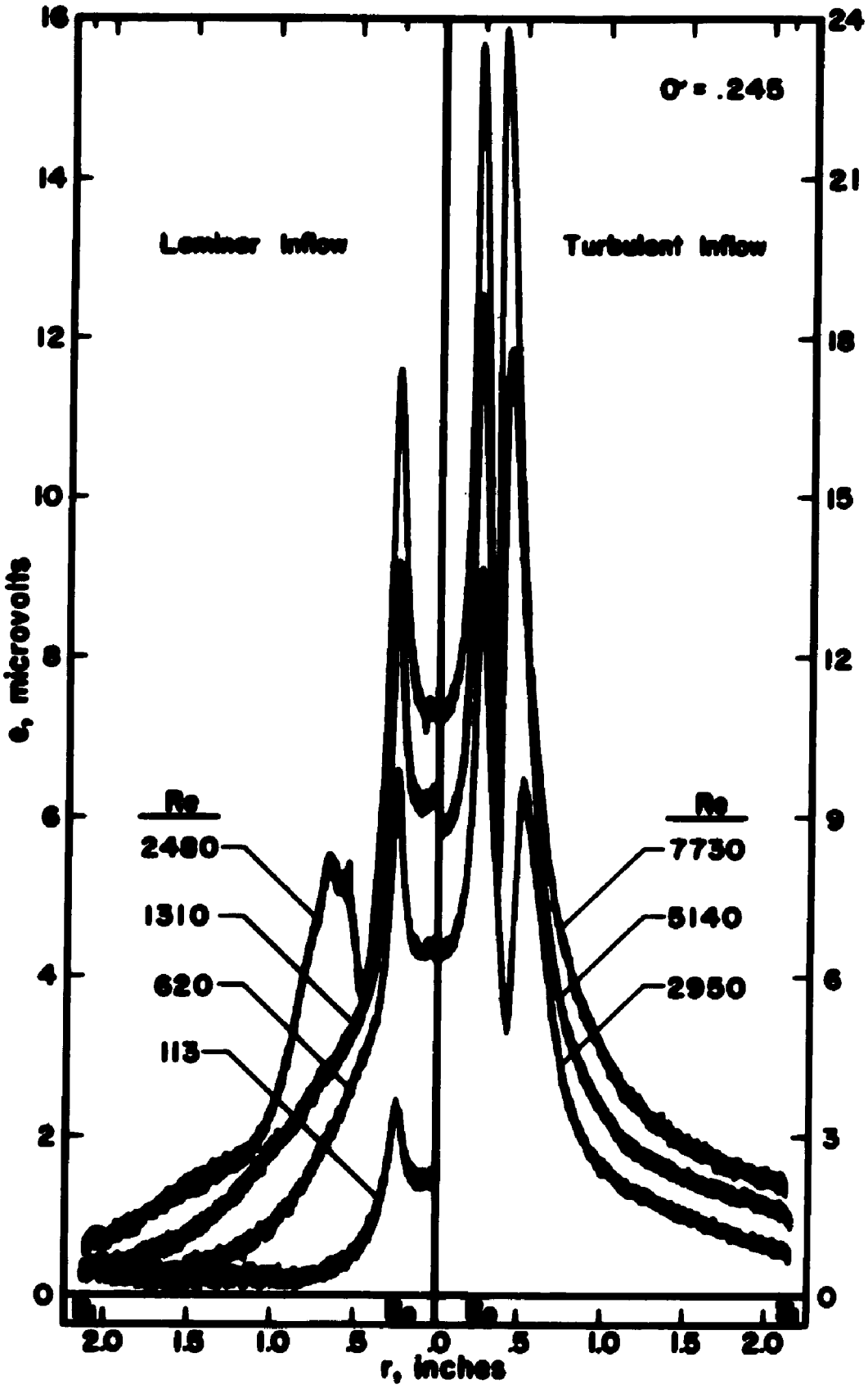


Figure 3-11. Heat Flux Distributions.

TABLE 3-2

EXPERIMENTAL DATA

FIGURE	Re	R_{R_o}	ΔT, °F	$\bar{T}_f$, °F	Nu_S	$\overline{Nu}$
3-9	113	58	36.5	99.3	16.1	2.44
	746	381	36.3	99.3	47.3	6.18
	1300	664	35.9	99.3	62.5	9.33
	2480	1260	35.6	99.3	77.4	15.10
	2970	1520	34.8	99.2	61.4	14.60
	5130	2620	34.6	99.1	77.7	21.90
	7710	3930	34.7	98.8	92.3	29.20
3-10	112	27	41.3	99.2	17.7	2.92
	619	152	41.4	99.0	45.0	5.99
	1300	319	40.7	98.7	65.2	10.50
	2470	605	36.3	99.3	79.7	16.90
	2920	715	35.5	99.3	69.1	17.10
	5100	1250	35.8	99.3	87.7	23.40
	7670	1880	36.0	99.1	106.0	30.70
3-11	113	7	44.8	98.8	16.9	3.75
	620	38	49.1	98.8	46.8	8.22
	1310	80	47.3	98.4	69.8	13.40
	2480	152	45.0	98.4	86.1	22.70
	2950	180	46.6	98.5	73.6	25.40
	5140	315	48.9	98.6	95.2	36.30
	7730	473	50.8	98.3	114.0	44.30

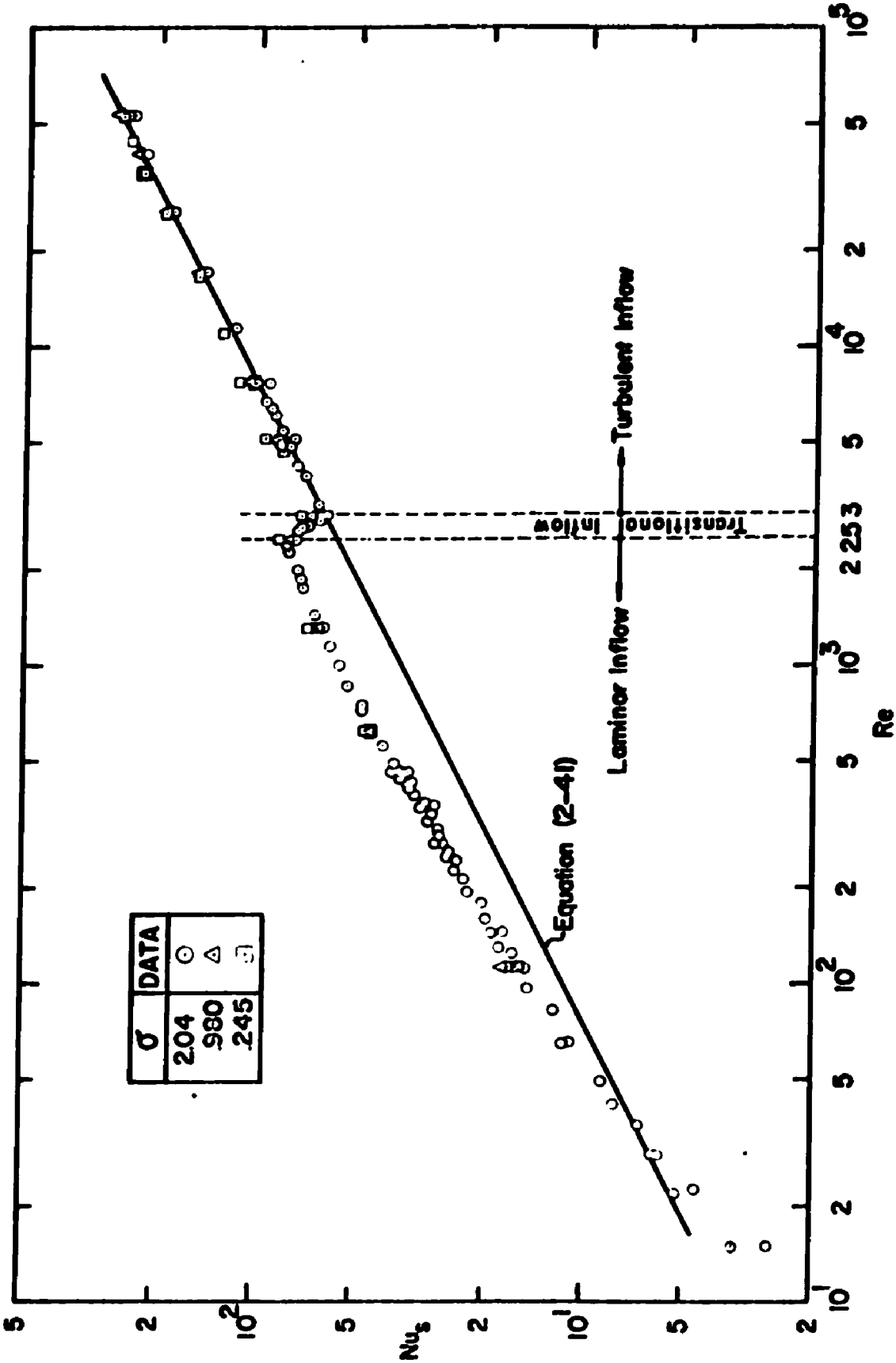


Figure 3-12. Stagnation Point Heat Transfer Rate vs Inlet Reynolds Number.

Reynolds number and are almost independent of the area ratios used. The stagnation point heat transfer rate always increases with increasing flow rate except for a decrease between the inlet Reynolds numbers of approximately 2500 and 3000 which corresponds to the transition regime of the inlet flow [43] .

The stagnation point heat transfer rate predicted by Equation (2-41) using a boundary layer analysis is also shown in Figure 3-12. Agreement with the experimental data is excellent for turbulent inflows, especially when the inlet Reynolds number exceeds 11,000. This is in agreement with the fact that the approaching pipe flow is turbulent and has no effect on the laminar stagnation point boundary layer calculation as long as the free stream turbulence is not strong enough to penetrate into the boundary layer. The data with a laminar inflow exceeding an inlet Reynolds number of 500 lie parallel to the theoretical line but are as much as 71% greater in magnitude. At lower inlet Reynolds numbers the effect of viscosity pervades the entire flow field and the boundary layer analysis which led to Equation (2-41) is no longer valid.

The flow and temperature fields at the stagnation point are functions of the approach velocity which corresponds to the centerline velocity of the inlet flow not the average velocity. The shape of the velocity distribution of the inlet flow near the centerline may also affect the stagnation point flow and temperature fields. Senecal and Rothfus [44] have experimentally observed that the flattening of the velocity profile of a transitional pipe flow occurs so rapidly as the flow rate increases that the centerline velocity actually decreases. Consequently, a plot of the centerline velocity versus the average velocity shows a drop off in the transition region.

This effect is also reflected in the heat transfer data of Figure 3-12, i.e., the stagnation point heat transfer rate rises and falls with the centerline velocity when correlated with an average velocity term like the inlet Reynolds number. The stagnation point heat transfer data of Figure 3-12 are correlated directly with the centerline Reynolds number, Re_ℓ, in Figure 3-13 using the experimental data of Senecal and Rothfus [44] and Knudsen and Katz [25] to relate the centerline velocity to the average velocity. The data now lie within $\pm$ 19% of the line representing Equation (2-41) for centerline Reynolds numbers between 220 and 65,000. The laminar data generally lie above the theoretical line and the turbulent data below, indicating that a complete correlation for laminar and turbulent flows must also account for the shape of the velocity profile as well as its centerline value.

The effect of varying the area ratio for constant flow rates is shown in Figure 3-14. The stagnation point heat transfer rate increases as the area ratio decreases reaching a plateau at an area ratio of approximately .2. This behavior is indicated theoretically by Equations (2-40) and (A-18) assuming that trends indicated by the latter equation for a two-dimensional flow are also pertinent to the axisymmetric case. As the area ratio is reduced below a value of .1 the stagnation point heat transfer rate diminishes because the flow no longer resembles a stagnation flow.

b. Stagnation Region

As shown in Figures 3-9 through 3-11, the stagnation region heat transfer rate distribution depends primarily on the area ratio. For large area ratios the heat transfer rate decreases from the stagnation point, while for small area ratios it increases

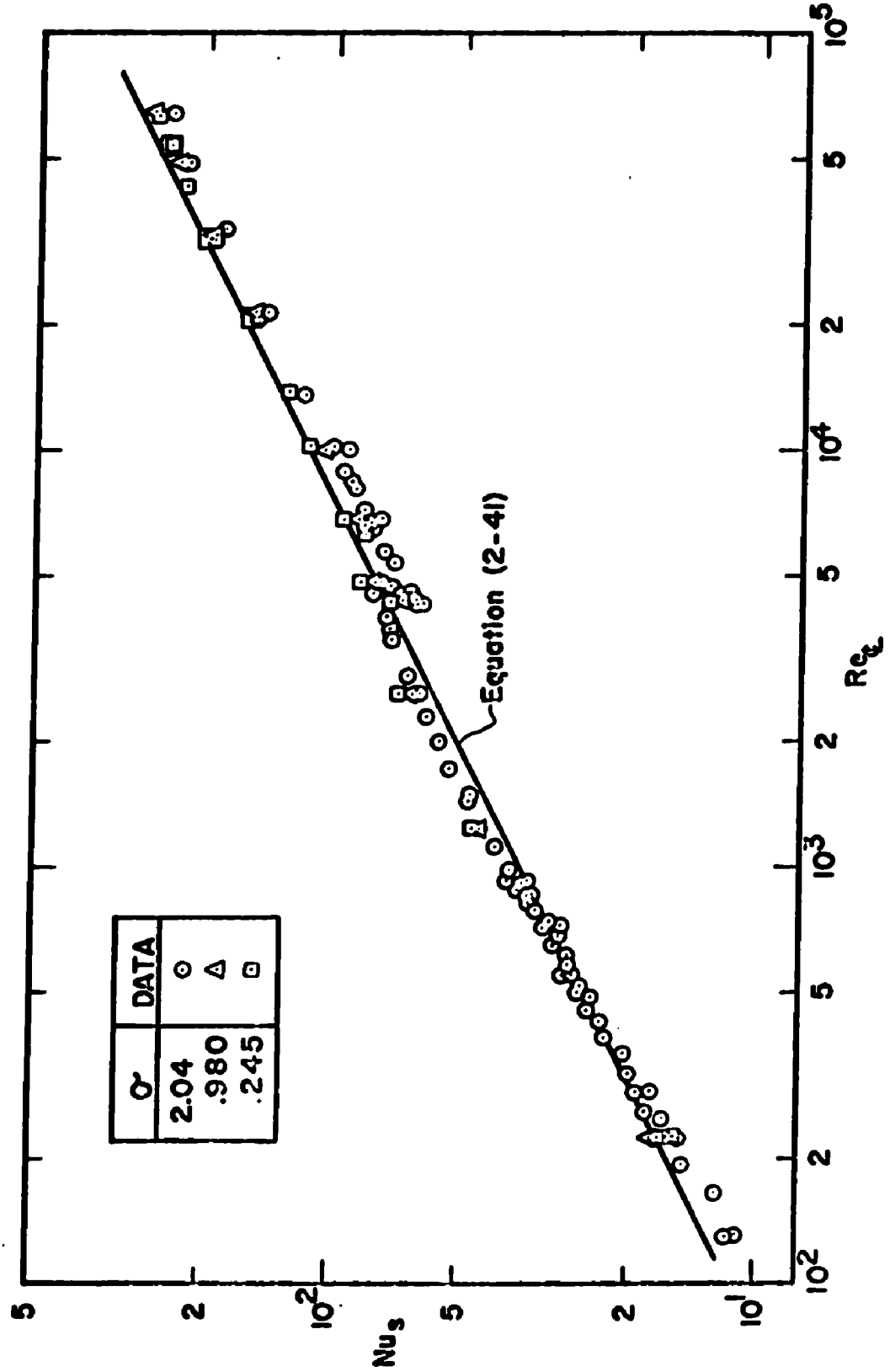


Figure 3-13. Stagnation Point Heat Transfer Rate vs Centerline Inlet Reynolds Number.

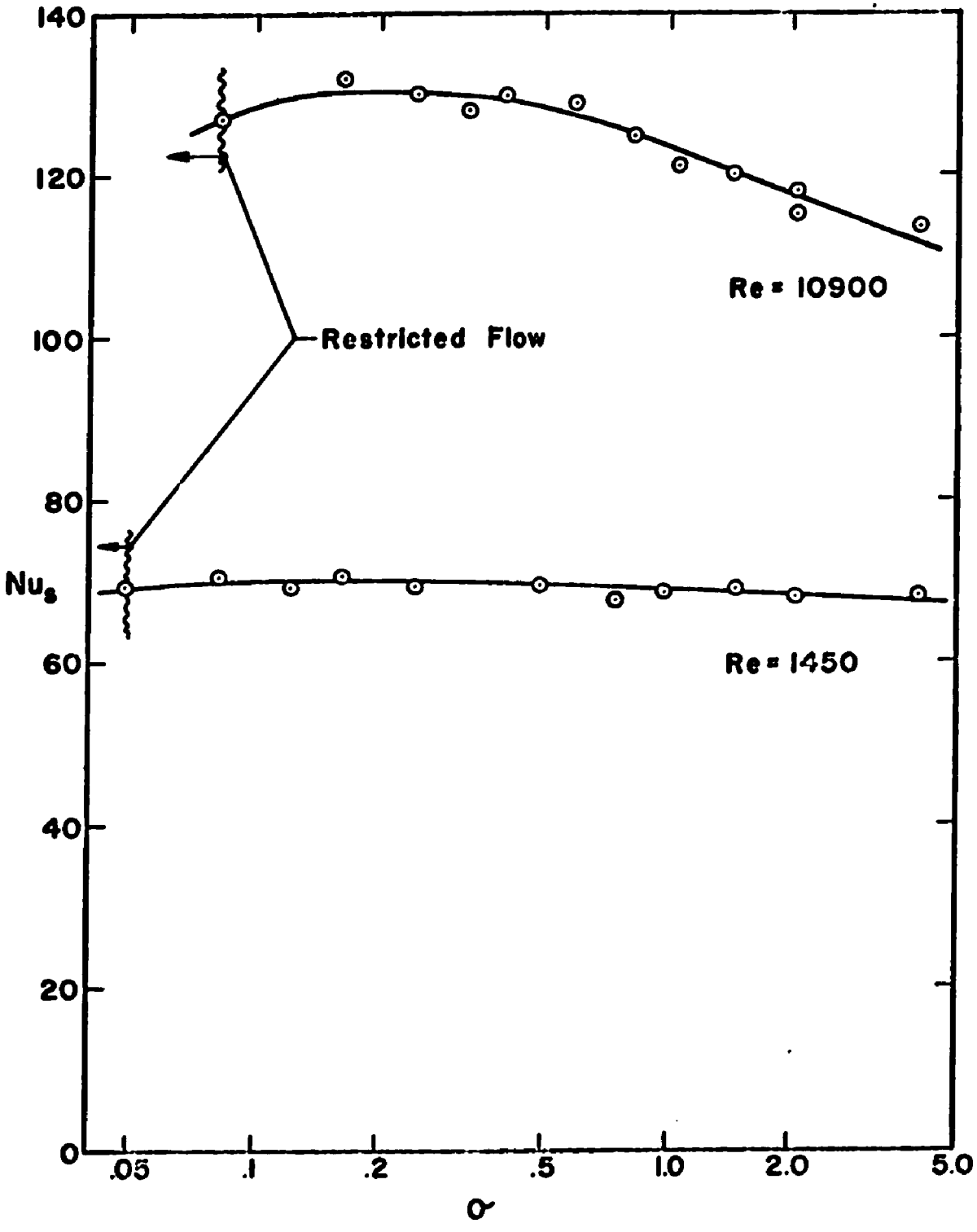


Figure 3-14. Stagnation Point Heat Transfer Rate vs Area Ratio.

reaching a maximum value at the inlet radius. The latter phenomenon becomes quite pronounced as the area ratio decreases, e.g., in Figure 3-11 the heat transfer rate at the inlet radius is approximately twice the stagnation point value for both laminar and turbulent inflows. The area ratio is the ratio of the stagnation region outflow and inflow areas. When the area ratio is less than unity the flow accelerates to the inlet radius, otherwise it decelerates. Correspondingly, the viscous and thermal boundary layers decrease and increase. The region of Hiemenz type flow, characterized by constant viscous and thermal boundary layer thicknesses, is limited to the immediate vicinity of the stagnation point. Similar results for invicid flow in a two-dimensional stagnation region are developed theoretically in APPENDIX IV.

c. Diffuser Region

Both the inlet flow and the area ratio affect the heat transfer rate distribution in the diffuser region. When the inlet flow is turbulent a secondary peak occurs in the heat transfer rate distribution downstream from the inlet radius. The magnitude of the secondary peak increases as the area ratio decreases and in Figure 3-11 it surpasses the peak at the inlet radius for the highest flow rate shown. The secondary peak indicates that the laminar boundary layer which has developed from the stagnation point has become turbulent. Similar phenomena have been observed for turbulent flows normal to cylinders [16], in the entrance region of a pipe [14], and in a two-dimensional confined corner [1].

The heat transfer rate with a laminar inflow decreases from the value at the inlet radius until the midpoint of the diffuser region is reached. Downstream of this point a dip in heat transfer

rate occurs sometimes followed by a secondary peak as shown in Figure 3-15. The variation in position of the local minimum in heat transfer rate at the dip in Figure 3-15 with inlet Reynolds number is shown in Figure 3-16. The position of the dip increases until an inlet Reynolds number of about 2140 is reached whereupon the position of the dip drops slightly and then rises again only to fall sharply at an inlet Reynolds number of 2780 after which it remains essentially constant. Up to the critical inlet Reynolds number given by Equation (1-1) the positions of the dip and the theoretical primary reattachment point behave similarly and have about the same value. This coupled with the fact that the secondary separation point lies upstream of the primary reattachment point indicates that the secondary vortex causes the dip by deflecting the main flow away from the hot surface. A secondary peak follows the dip at flow rates above the critical value because the flow becomes turbulent downstream of the secondary separation point. The sudden drop in position of the dip and the secondary peak midway through the transition region of the incoming flow indicates that the primary vortex has contracted because it has become turbulent.

In Figure 3-17 experimental and theoretical heat transfer rate distributions for the diffuser region are compared for laminar inflows and an area ratio of 0.245. The theoretical distributions are calculated from Equations (2-44) with the free parameter evaluated according to the second perturbation solution of Equations (2-11). The heat transfer rates at the inlet radius, R_o, are determined from the experimental results of Figure 3-11. The theoretical results exhibit the same characteristics as the experimental data, although the numerical values become significantly

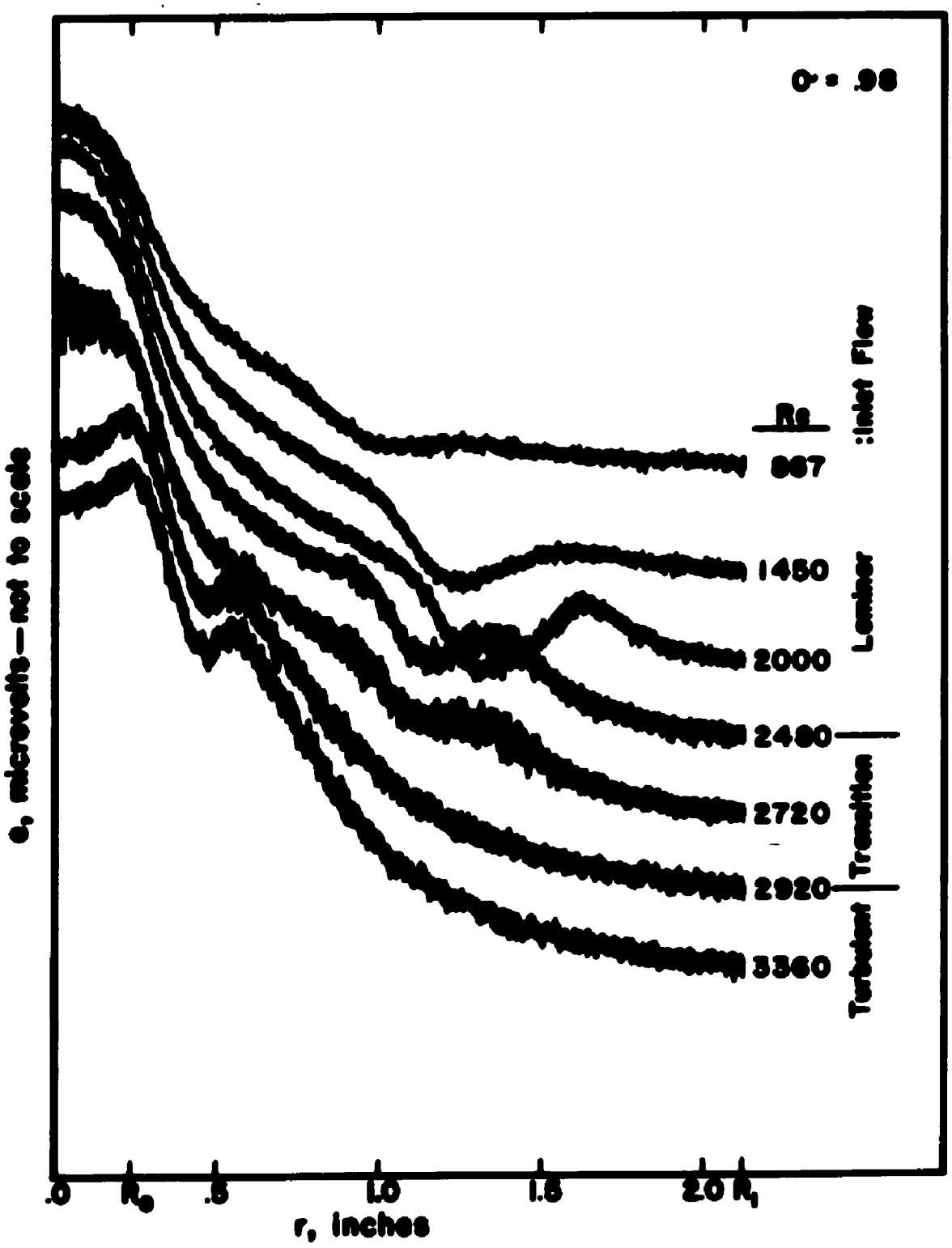


Figure 3-15. Heat Flux Distributions.

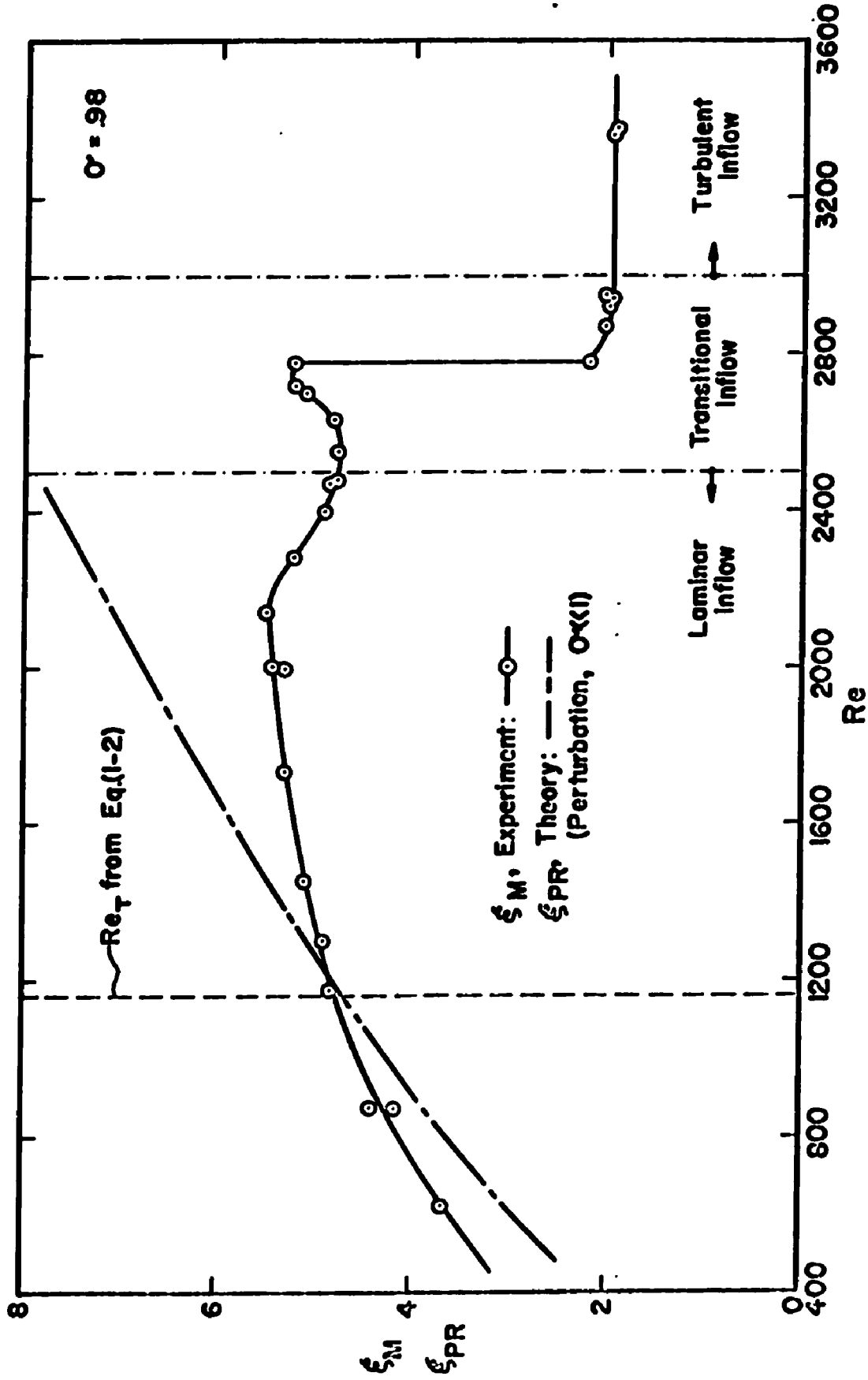


Figure 3-16. Position of Local Minimum in Heat Transfer Rate vs Inlet Reynolds Number.

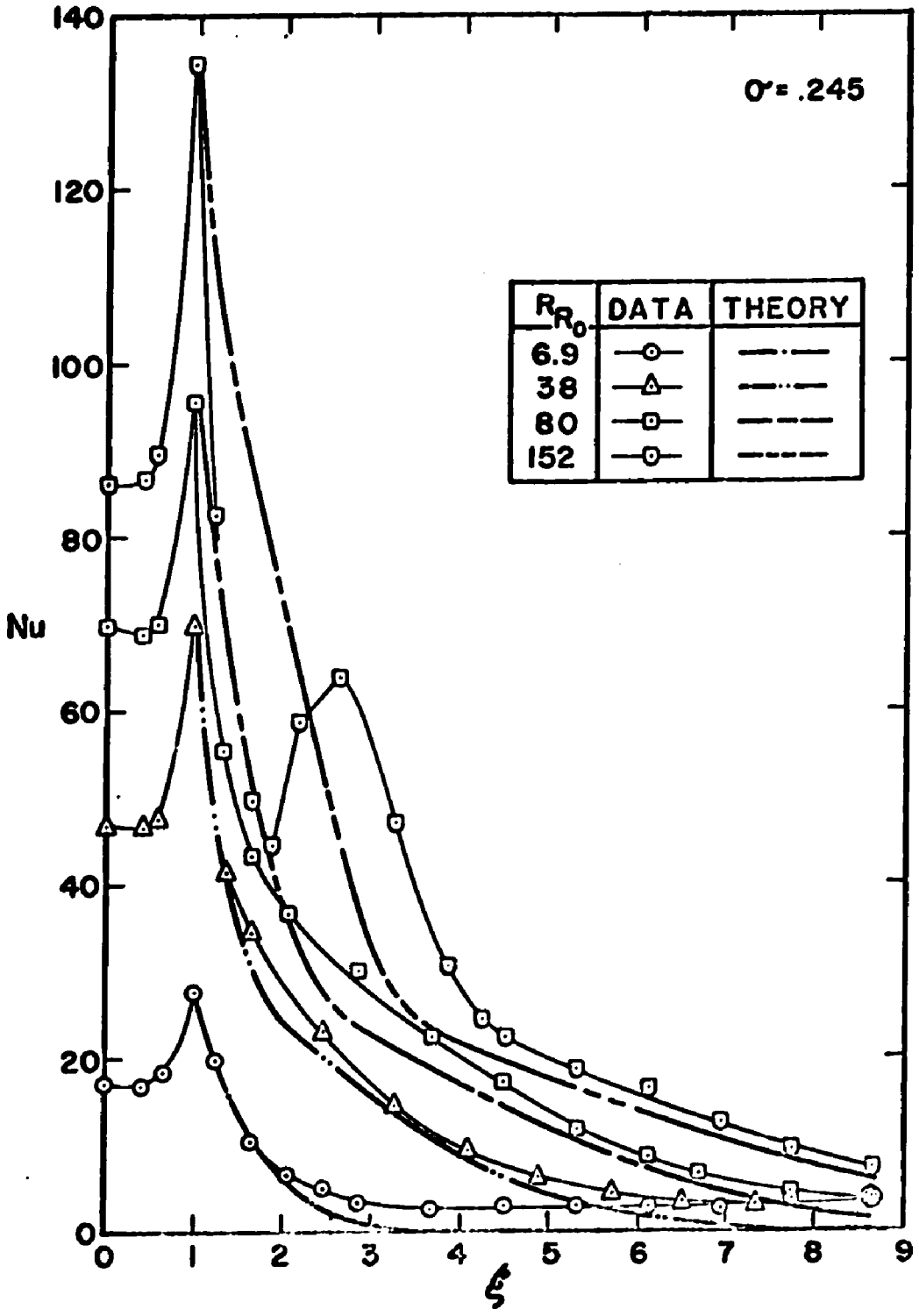


Figure 3-17. Heat Transfer Rate Distributions.

larger near the inlet radius for the two highest diffuser Reynolds numbers. This is not unexpected since the velocity and temperature profiles used in the theoretical analysis are only approximations of those which actually occur. At the highest flow rate a secondary peak occurs in the experimental data, indicating that the laminar boundary layer has become turbulent. Retransition occurs at a radius, ξ, of about 4.5, a consequence of the fact that the average flow rate varies inversely with the radius.

The experimental data of Figure 3-17 tend to approach a common value as the flow rate decreases in the radial direction indicating that natural convection effects become dominant. The theoretical analysis did not consider this effect. McAdams [31] recommends the following equation to approximate the heat transfer rate by free convection from a square heated plate facing upwards in air:

$$\dot{q} = .27 \Delta T^{\frac{3}{4}} L^{-\frac{1}{4}} \quad \text{(Btu/ft.}^2\text{ - hr.)} \qquad (3\text{-}4)$$

where L is the side dimension and ΔT is the difference between the hot plate and ambient air temperatures. Using the diameter of the hot plate as the length, the estimated natural convection heat transfer rate for the present case corresponds to a Nusselt number of about 2. This value compares well with the experimental value of about 3 in Figure 3-17. Figures (3-9) through (3-11) show that natural convection heat transfer becomes important only at the lowest inlet Reynolds number and/or at large radii.

d. Average

The average heat transfer rate from the isothermal surface from r=0 to $r=R_1$, is shown in Figure 3-18 with the inlet

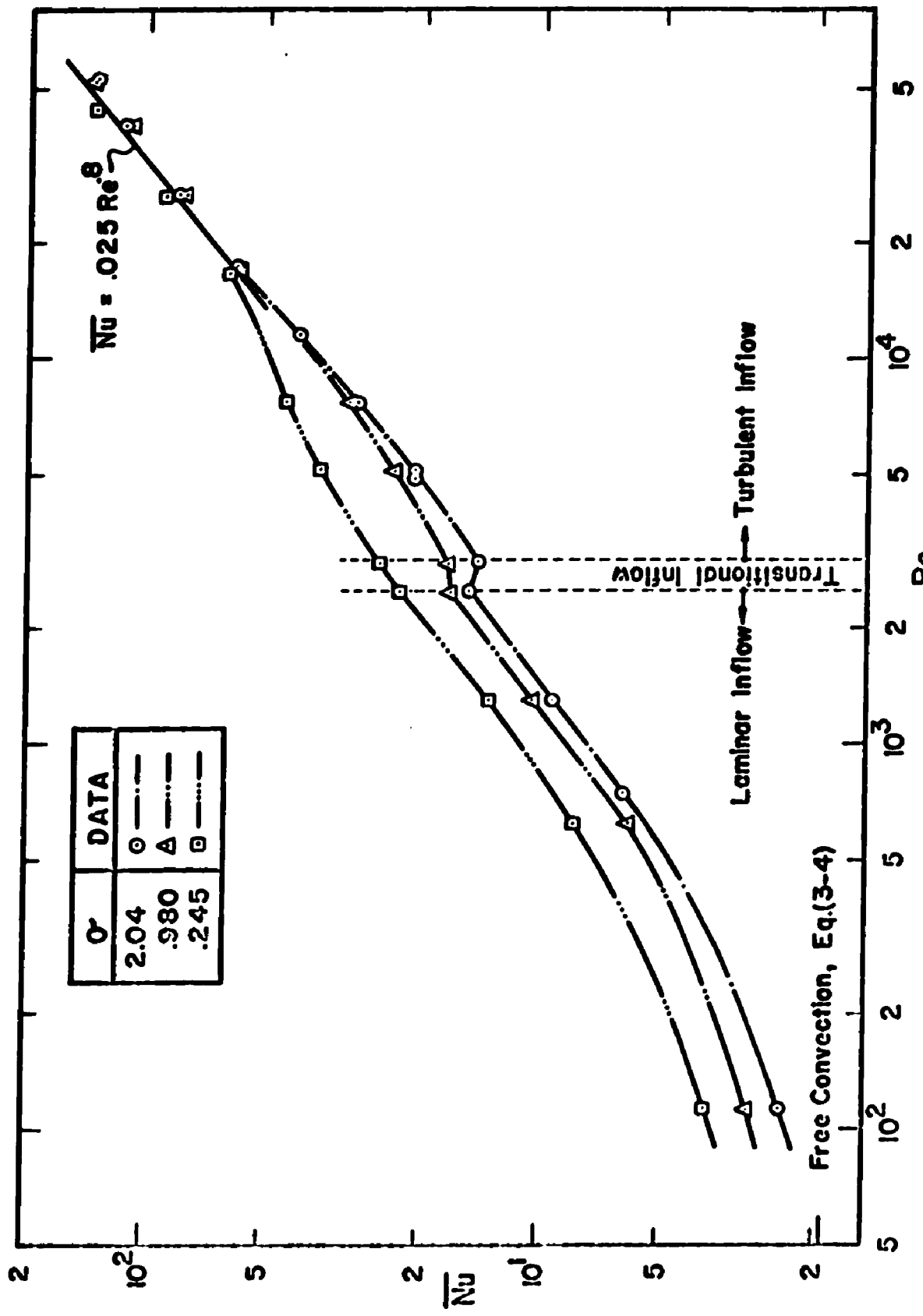


Figure 3-18. Average Heat Transfer Rate vs Inlet Reynolds Number.

Reynolds number, Re, and the area ratio, σ, as parameters. The averages were calculated by numerically integrating a finite number of points from the experimental heat flux distributions of Figures 3-9 through 3-11, as well as other distributions made a higher flow rates, from r=0 to r=R_1, i.e.,

$$\overline{Nu} = \frac{1}{\pi R_1^2}\int_0^{R_1} Nu\, 2\pi r dr$$

or, in dimensionless form,

$$\overline{Nu} = 2\left(\frac{R_2}{R_1}\right)^2\int_0^{\xi_1} Nu\,\xi\, d\xi \qquad (3\text{-}5)$$

where the Nusselt number, Nu, is evaluated from Equations (3-3) and (3-2).

In Figure 3-18 the average Nusselt number for inlet Reynolds numbers below 17,000 depends strongly on the area ratio, increasing as the area ratio decreases. For a particular area ratio the average Nusselt number increases with increasing flow rate except in the transition region where a drop off occurs for the largest area ratio. Apparently the heat transfer phenomenon in the stagnation region, which depends primarily on the area ratio, significantly affects the average heat transfer rate. Although the stagnation region occupies only 1.4% of the total area, πR_1^2, it contributes as much as 10% to the average Nusselt number because of the high average heat transfer rate there. Moreover, the initial heat transfer rate in the diffuser region depends on what happens in the stagnation region. Referring to Figures 2-9 through 2-11, a peak in heat transfer rate appears at the inlet radius as the area ratio decreases. The magnitude of this peak relative to that at the stagnation point increases with decreasing area ratio, thus causing

the average heat transfer rate to increase. The secondary peak behaves in a similar fashion. The effect of these peaks is so strong that for the smallest area ratio no drop off in heat transfer rate occurs in the transition region and the subsequent turbulent values are significantly above those for the other two area ratios. For inlet Reynolds numbers above 17,000, however, the area ratio is no longer very significant and the average heat transfer rate data correlate with the inlet Reynolds number as

$$\overline{Nu} = .025\, Re^{.8} \tag{3-6}$$

to within $\pm$ 7%. At very low flow rates the average heat transfer becomes primarily dependent on natural convection and the average Nusselt number approaches a natural convection value of about 2 indicated on the ordinate axis as calculated from Equation (3-4).

The data in Figure 3-18 for laminar flows exceeding an inlet Reynolds number of 600 bear the same power law relationship to the inlet Reynolds number as the turbulent flows of Equation (3-6). In the theoretical analysis of heat transfer in the diffuser region for laminar flows of CHAPTER II the local Nusselt number is a function of the area ratio, σ, and the diffuser Reynolds number, R_{R_o}. The latter parameter is

$$R_{R_o} = \frac{\rho \dot{V} Z_o}{\mu \pi R_o^2} = \frac{\rho \bar{U}_{Z_o} Z_o}{\mu}$$

and may be considered as a Reynolds number based on the average inlet velocity, $\bar{U}_{Z_o}$, and the separation between the surfaces, Z_o. Since the characteristic length used in the dimensionless flow and heat transfer

parameters must be the same [43], a new Nusselt number based on Z_o is defined as

$$Nu_{Z_o} = \frac{\dot{q} Z_o}{k \Delta T} = \frac{\alpha}{4} Nu$$

The data of Figure 3-18 is replotted in Figure 3-19 in terms of Nu_{Z_o} and R_{R_o}. For laminar flow rates exceeding an inlet Reynolds number of 600 the data correlate with the diffuser Reynolds number as

$$\overline{Nu}_{Z_o} = .026\, R_{R_o}^{.8} \qquad (3\text{-}7)$$

to within $\pm$ 5%. For laminar flow rates below an inlet Reynolds number of 600 the data no longer correlate with Equation (3-7) because natural convection heat transfer becomes important. This corresponds with the fact that the heat flux distributions of Figures (3-9) through (3-11) from which the averages are calculated are predominantly natural convective only for the lowest inlet Reynolds number which was about 113. For turbulent flow rates the data bear the same power law relationship to the diffuser Reynolds number as found for the laminar correlation of Equation (3-7) except that the magnitude of the constant decreases with decreasing area ratio. If the diffuser Reynolds number is based on the centerline velocity of the inlet flow, the data as shown in Figure 3-20 correlate with the centerline diffuser Reynolds number, $R_{R_{o,\ell}}$, as

$$\overline{Nu}_{Z_o} = .013\, R_{R_{o,\ell}} \qquad (3\text{-}8)$$

to within $\pm$ 6.8% for laminar inlet Reynolds numbers above 600 and to within $\pm$ 20% for turbulent inlet Reynolds numbers below 53,000 for the area ratios tested.

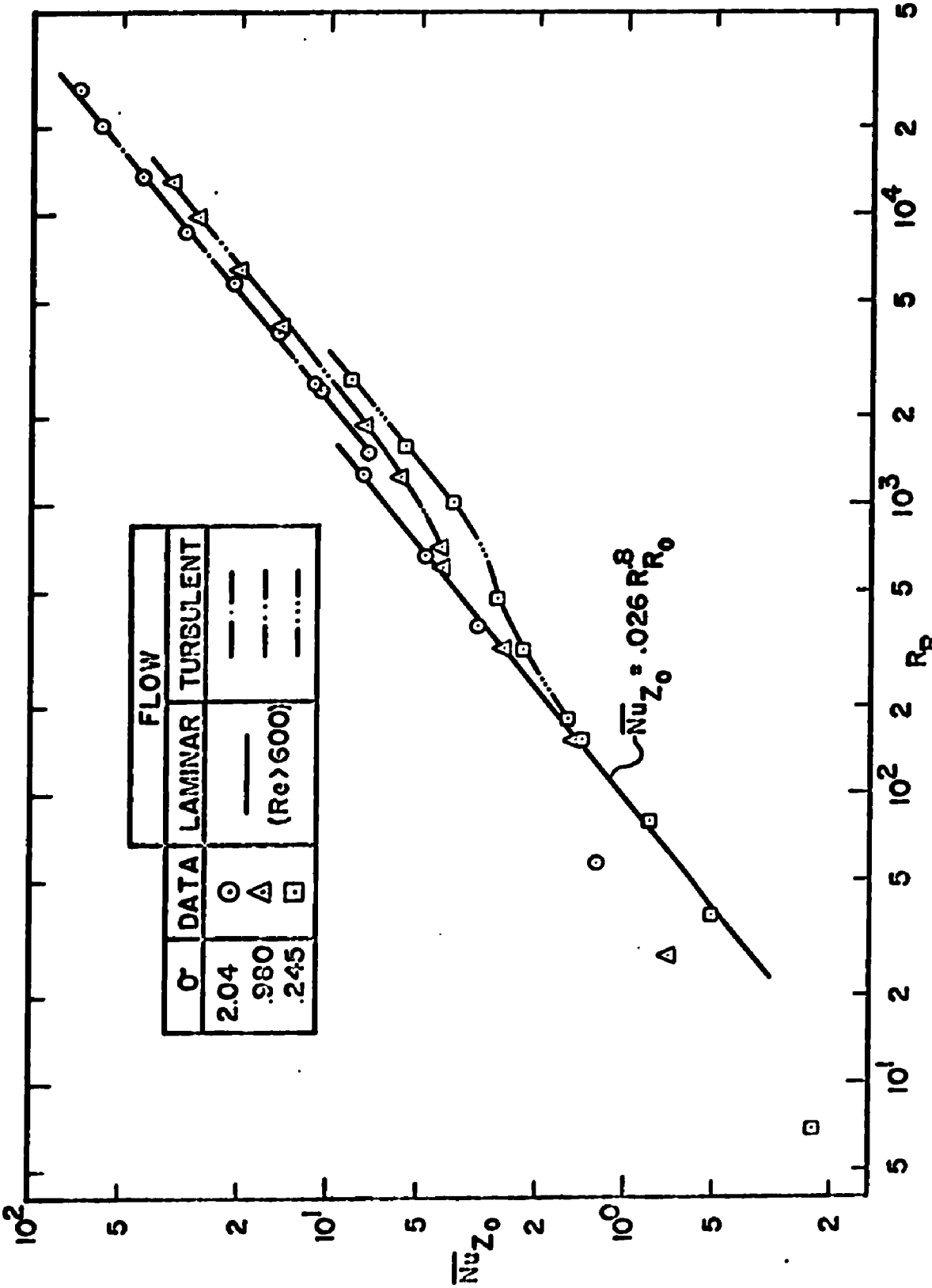


Figure 3-19. Average Heat Transfer Rate vs Diffuser Reynolds Number.

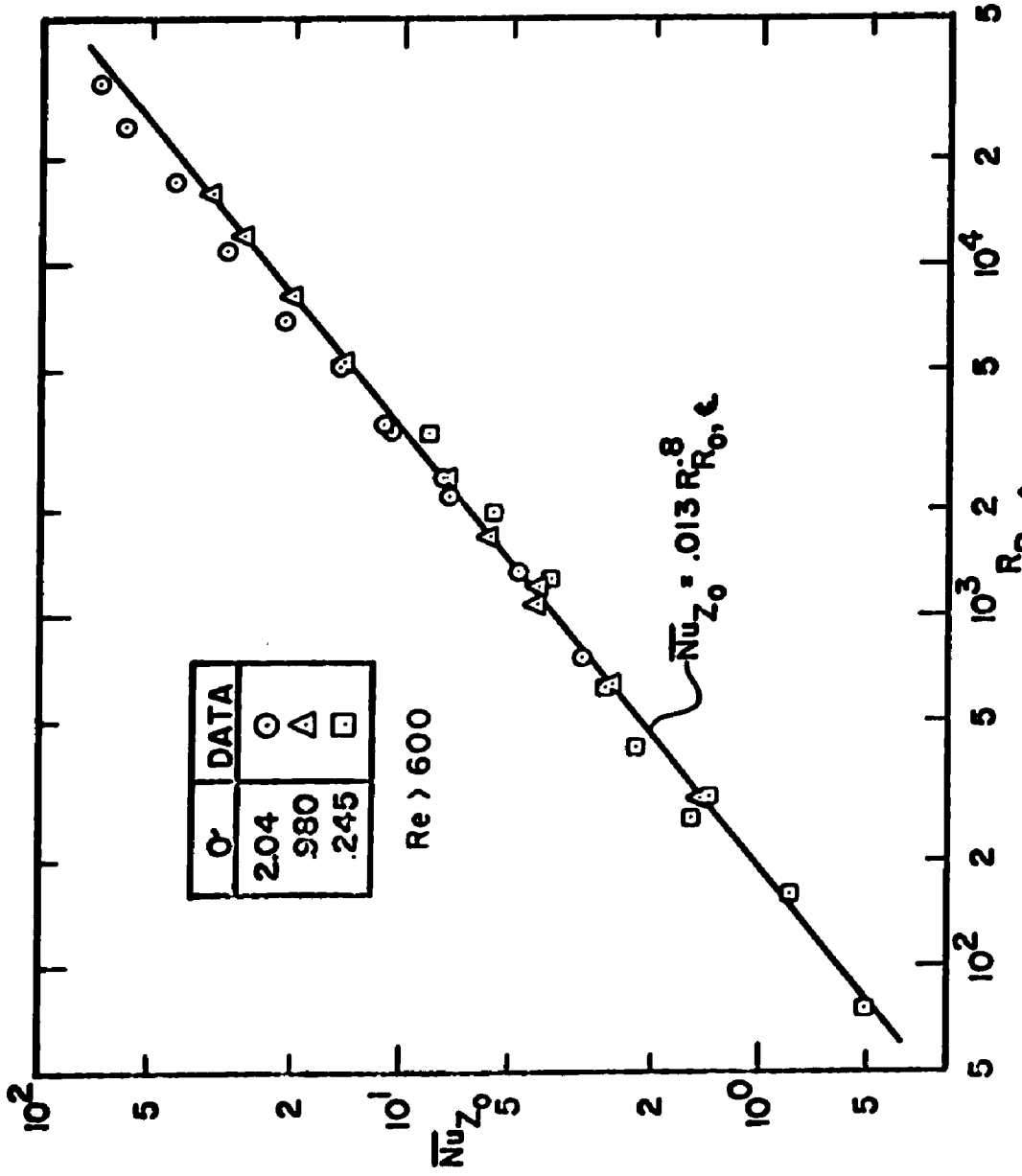


Figure 3-20. Average Heat Transfer Rate vs Centerline Diffuser Reynolds Number.

The fact that the average heat transfer rate data correlate with a Reynolds number to the same power for both laminar and turbulent flows must be ascribed to the geometry of the radial diffuser and the resulting influence of stagnation region heat transfer phenomenon on the average heat transfer rate which was discussed above. No other forced convective heat transfer system, internal or external, exhibits this characteristic.

The exponent value of .8 which appears in Equations (3-6) through (3-8) has previously been observed by Kreith [28] in mass transfer experiments simulating the present heat transfer problem for turbulent flows. Kreith's data are correlated with a form of diffuser Reynolds number and do not show a dependence on the area ratio as do the present data as shown in Figure (3-7). The laminar heat transfer data of Kreith also correlate with a form of diffuser Reynolds number to a power but the exponent is not the same as that for the turbulent data as in the present case. This discrepancy may be caused by the fact that Kreith eliminated the stagnation region in his experiments by covering it with an impervious coating and used a rounded inlet corner.

5. Experimental Uncertainty

Using Equation (3-1), the greatest uncertainty in determining the inlet Reynolds number lies in determining the flow rate. The accuracy of the Brooks rotameter used in a majority of the tests is 2% of full scale or .0446 SCFM. The flowmeter is, therefore, most accurate for high flow rates. The uncertainty associated with the inlet Reynolds number, Re, approaches $\pm$ 2.1% at the highest flow rates used, rising to $\pm$ 25% at the lowest.

The greatest uncertainty in determining the Nusselt number lies in determining the heat transfer rate. The accuracy of the heat flux transducer, microvolt-ammeter, and x-y recorder are $\pm$ 2.93% of reading, $\pm$ 1% of full scale, and $\pm$ .2% of full scale respectively. For laminar inlet flows the maximum uncertainty in the Nusselt number, Nu, was $\pm$ 9.3% while for turbulent flows it was $\pm$ 4.1%. The gap between the surfaces, Z_o, was set to within $\pm$ .0005 in. using gage blocks. The inlet radius, R_o, and the outlet radius, R_1, were measured by a vernier caliper to within $\pm$ .001 in. The uncertainty in the area ratio, σ, usually varied from $\pm$ .56% for the largest gap to $\pm$ 3.3% for the smallest gap.

CHAPTER IV

SUMMARY OF RESULTS

In Chapter II the flow and heat transfer problems for laminar flow in a radial diffuser were stated and approximate solutions derived for the velocity and temperature fields at the stagnation point and in the diffuser region using integral techniques. The pertinent dimensionless parameters were the inlet Reynolds number, the ratio of the stagnation region exit to inlet area or area ratio, the diffuser Reynolds number, and the Prandtl number. The diffuser Reynolds number is the product of the inlet Reynolds number and the area ratio and was significant in describing the flow in the diffuser region.

The heat transfer rate at the stagnation point was derived using the momentum integral technique with a fourth-order Kármán-Pohlhausen velocity profile. The solution depends on the ratio of the dimensionless free stream velocity gradient at the stagnation point to the area ratio as well as the inlet Reynolds number. The preceding ratio was investigated for a two-dimensional stagnation region, since invicid flow in an axisymmetric stagnation region cannot be treated analytically, and asymptotically approaches a constant value as the area ratio becomes much less than unity. Similar behavior should obtain for the axisymmetric case.

No solution for the heat transfer distribution in the stagnation region was attempted because of the above mentioned difficulty in solving the invicid flow problem which is necessary to

determine the free stream velocity.

In the diffuser region the flow field included a primary vortex which extended downstream from the sharp inlet corner. The velocity field was derived using the Galerkin method of weighted residuals with a one-parameter stream function. For area ratios less than .32 the free parameter was adequately represented by a perturbation solution to the second approximation. Criteria were developed for the inception of the primary vortex and its subsequent growth in length and thickness with increasing diffuser Reynolds number. The radial pressure distribution was evaluated and is significantly affected by the presence of the primary vortex, especially at high flow rates. Theoretical radial pressure distributions agreed better with experimental results by other authors when a primary vortex was included in the flow field than when it was not. The heat transfer rate was derived using the energy integral technique with the one-parameter velocity field. An experimental value was required as an initial condition because no analytical value was available from the stagnation region, as outlined in the preceding paragraph.

In Chapter III the experimental apparatus were described for the flow and heat transfer investigations which were conducted separately. The fluid in both cases was air.

The flow field was studied by flow visualization using smoke filaments. The area ratio ranged from .75 to 1.88 and the inlet Reynolds number from 193 to 1422. The length and thickness of the primary vortex were measured from photographs of the smoke filaments systematically taken for different inlet Reynolds numbers and area ratios. The analytical flow solution adequately described the

inception of the primary vortex and its subsequent growth in length and thickness with increasing diffuser Reynolds number although there appeared to be a secondary area ratio effect not accounted for in the analysis.

The heat transfer investigation was carried out using a foil type heat flux transducer imbedded in and flush with the isothermal surface. Experiments were conducted for turbulent as well as laminar inflows. The area ratio ranged from .245 to 2.04 and the inlet Reynolds number from 15 to 53,500. When correlated with an inlet Reynolds number based on the centerline velocity in the inlet tube, the experimental results for the stagnation point heat transfer rate agreed with the theoretical equation within $\pm$ 19% for centerline Reynolds numbers from 220 to 65,000. The heat transfer rate distributions in the diffuser region were adequately described by analysis for an area ratio of .245. Below an area ratio of approximately 1 the heat transfer rate in the stagnation region for both laminar and turbulent flows rises from the stagnation value to a maximum at the inlet radius instead of falling, i.e. the maximum heat transfer rate shifts from the stagnation point to the inlet radius. With a laminar inflow above a critical value the flow becomes turbulent near the primary reattachment radius causing a secondary peak in the heat transfer rate distribution. When the inflow becomes turbulent the secondary peak moves to a position slightly downstream of the inlet radius. For an area ratio of .245 the primary peak at the inlet corner and the secondary peak are roughly the same in magnitude which is about twice the stagnation point value. The average heat transfer rate data, calculated by numerically integrating the heat transfer rate

distributions, correlate with the centerline diffuser Reynolds number as

$$\overline{Nu}_{Z_e} = .013\, R_{R_e,\ell}^{.8}$$

to within $\pm$ 6.8% for laminar inlet Reynolds numbers above 600 and to within $\pm$ 20% for turbulent inlet Reynolds numbers below 53,000. The correlation of both laminar and turbulent flows to a Reynolds number with the same exponent was ascribed to the fact that the heat transfer phenomenon in the stagnation region exerts a strong influence on the average heat transfer rate.

APPENDICES

APPENDIX I

COORDINATE PERTURBATION SOLUTION OF EQUATION (2-2-a) FAR DOWNSTREAM

Far downstream in the diffuser region, i.e. for $\mathcal{F} \gg 1$, a power series solution in terms of the coordinate perturbation parameter $\epsilon = \frac{1}{\mathcal{F}}$ is assumed for the stream function of the form

$$\Psi = \sum_{n=0}^{\infty} \epsilon^n \Psi_n = \Psi_0 + \epsilon \Psi_1 + \epsilon^2 \Psi_2 + \cdots ; \quad \Psi_n = \Psi_n(\eta) \qquad \text{(A-1)}$$

Substitution of Equation (A-1) into Equation (2-2-a) and arranging in terms of ϵ^n, the first two approximations are

First Approximation, ϵ^0:

$$\Psi_0^{IV} = 0$$

$$\Psi_0(0) = \Psi_0^{I}(0) = 0 ; \quad \Psi_0(1) = 1 , \Psi_0^{I}(1) = 0$$

Second Approximation, ϵ^1:

$$\Psi_1^{IV} + R_{R_0} \Psi_0^{I} \Psi_0^{II} = 0$$

$$\Psi_1(0) = \Psi_1^{I}(0) = 0 ; \quad \Psi_1(1) = \Psi_1^{I}(1) = 0$$

Clearly the solution of the first approximation is

$$\Psi_0 = 3\eta^2 - 2\eta^3$$

While the solution of the second approximation becomes

$$\Psi_1 = \frac{9}{5} R_{R_0} \left(\frac{1}{42}\eta^2 - \frac{1}{14}\eta^3 + \frac{1}{6}\eta^5 - \frac{1}{6}\eta^6 + \frac{1}{21}\eta^7 \right)$$

The radial velocity field is

$$u(\xi,\eta) = \frac{1}{\xi}\frac{\partial}{\partial\eta}(\psi_0 + \epsilon\psi_1)$$
$$= \frac{6}{\xi}(\eta-\eta^2) + \frac{3}{70}\frac{R_{R_o}}{\xi^3}(2\eta-9\eta^2+35\eta^4-42\eta^5+14\eta^7) \qquad \text{(A-2)}$$

to the second approximation, where $\xi = x^{\frac{1}{2}}$.

The first term on the right of Equation (A-2) is the well known parabolic profile, while the second term represents a profile symmetric about the plane at $\eta = \frac{1}{2}$. The resulting velocity profile is flatter than a parabolic profile. However, when $\xi > .378 R_{R_o}^{\frac{1}{2}}$ the velocity profile is within 10% of being parabolic. In most cases considered in this study $R_{R_o} \geq 42$, hence when $\xi > 2.45$ a parabolic profile should prevail. Undoubtedly this limit represents a minimum value because the effect of the primary vortex and the higher approximations are not considered. Nevertheless, according to the above analysis a parabolic profile is approached far downstream.

APPENDIX II

COORDINATE PERTURBATION SOLUTION OF EQUATION (2-6-a) NEAR THE INLET RADIUS

Near the inlet radius let the free parameter, F, be written as a power series expansion in the coordinate perturbation parameter $\epsilon = \mathcal{Y} - 1$:

$$F = \sum_{n=0}^{\infty} \epsilon^n F_n = F_0 + \epsilon F_1 + \epsilon^2 F_2 + \cdots ; \quad F_n = F_n(\sigma, R_{R_0}) \qquad \text{(A-3)}$$

Then the derivatives of F with respect to the radial coordinate $\mathcal{Y}$ are

$$F^{I} = F_1 + 2\epsilon F_2 + \cdots$$
$$F^{II} = 2F_2 + \cdots$$

At the inlet radius, $\epsilon \to 0$ and the free parameter F and its derivatives become

$$F(1) = 3 = F_0 ; \quad F^{I}(1) = F_1 ;$$
$$F^{II}(1) = 2F_2 ; \quad \cdots$$

Substituting Equation (A-3) into Equation (2-6-a) and arranging in terms of ϵ^n gives

$$\epsilon^0: \; 11F_1 - 88\frac{\sigma^2}{R_{R_0}}F_2 - \sigma^2\left(15 - 22\frac{\sigma^2}{R_{R_0}}\right)F_3 + 44\frac{\sigma^4}{R_{R_0}}F_4 + \cdots = 22\left(1 - \frac{42}{R_{R_0}}\right)F_0$$

$$\epsilon^1: \; 11\left(\frac{84}{R_{R_0}} - 1\right)F_1 + 22\left(1 - 8\frac{\sigma^2}{R_{R_0}}\right)F_2 - 2\sigma^4\left(15 + \frac{132}{R_{R_0}} - 22\frac{\sigma^2}{R_{R_0}}\right)F_3 - 20\sigma^2\left(3 - 11\frac{\sigma^2}{R_{R_0}}\right)F_4 + \cdots = -\frac{924}{R_{R_0}}F_0$$

$$\epsilon^2: \; \frac{924}{R_{R_0}}F_1 + \frac{44}{R_{R_0}}(21 - 2\sigma^2)F_2 + \left\{33 - \sigma^2\left[15 + 22(24 - \sigma^4)/R_{R_0}\right]\right\}F_3 - 4\sigma^2\left[30 + 11(12 - 7\sigma^2)/R_{R_0}\right]F_4 + \cdots = 0$$

$$\epsilon^3: \; \frac{924}{R_{R_0}}F_2 + 11\left[1 + 12(7 - 2\sigma^2)/R_{R_0}\right]F_3 + 4\left\{11 - 3\sigma^2\left[5 + 11(8 - \sigma^2)/R_{R_0}\right]\right\}F_4 + \cdots = 0 \qquad \text{(A-4)}$$

...

For the asymptotic case where the area ratio, σ, is much less than unity, the solution of Equations (A-4) give the first two derivatives of the free parameter at the inlet corner as

$$F^{I}(1) = 6(1 - \frac{42}{R_{R_e}}) \qquad \text{(A-5-a)}$$

$$F^{II}(1) = 6(1 - \frac{168}{R_{R_e}} + \frac{3528}{R_{R_e}^2}) \qquad \text{(A-5-b)}$$

As the order of the approximating function of Equation (A-3) is increased the solutions converge for higher values of the area ratio. Whether the convergence is to the exact solution is, of course, unknown. The results for a fourth-order solution of Equations (A-3) and (A-4) are shown in Figure A-1 for the first two initial derivatives, $F^{I}(1)$ and $F^{II}(1)$. $F^{I}(1)$ has converged for $\sigma^2 \leq .1$ but $F^{II}(1)$ has not yet achieved convergence for this area ratio. Both initial derivatives asymptotically approach a value of 6 as the diffuser Reynolds number increases. Initial derivatives evaluated in this manner are approximate and limited to area ratios less than unity, but so is the governing equation solved numerically in Chapter II, where Equation (A-5-a) is utilized.

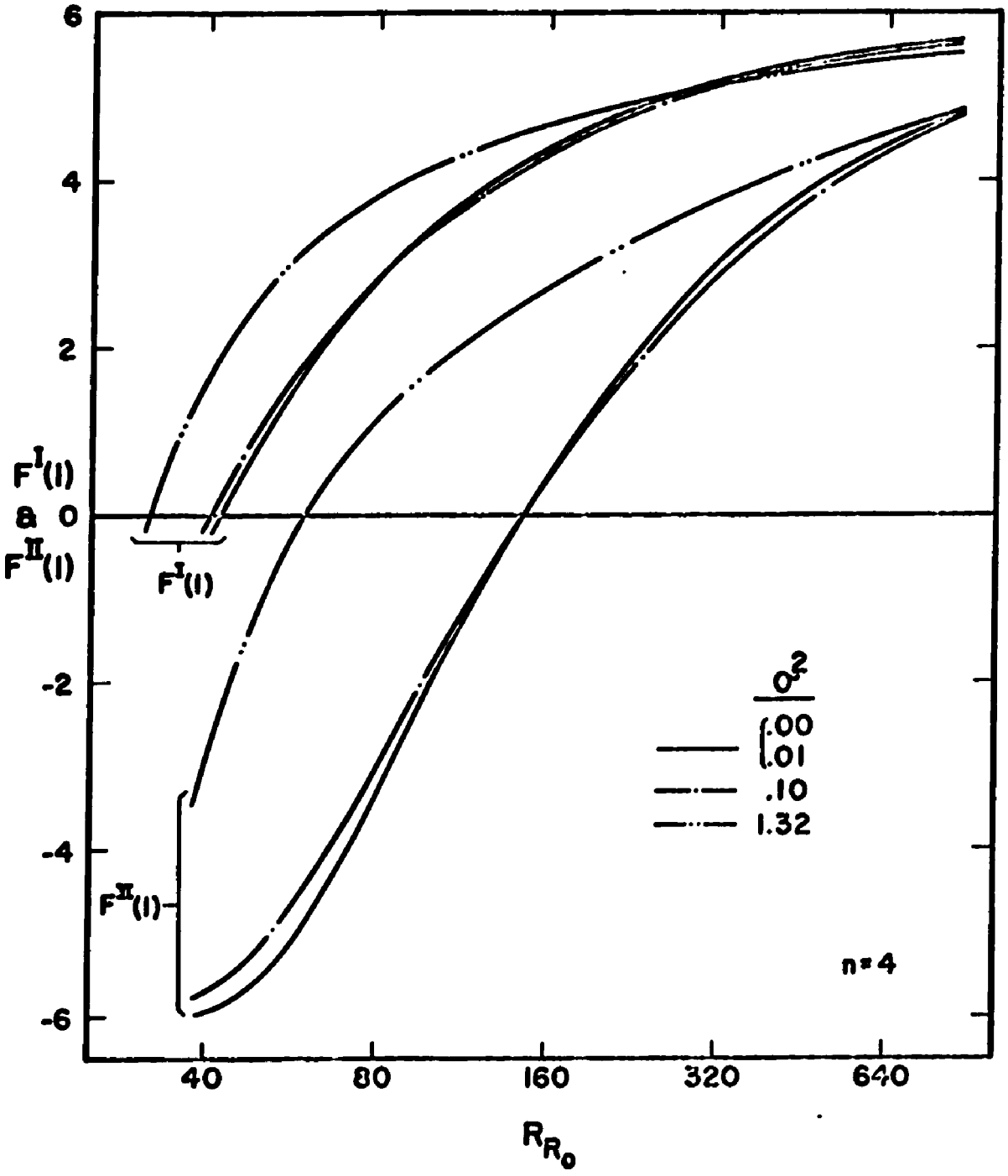


Figure A-1. Derivatives of Free Parameter at Inlet Radius.

APPENDIX III

RELATIONSHIP BETWEEN SEPARATION STREAMLINE AND FREE PARAMETERS

As shown in Figure 2-1, the primary vortex is bounded by the upper surface and the separation streamline. A relationship between the axial position of the separation streamline, η_p, and the free parameters F_1 and F_2 may be derived by evaluating Equation (2-1-a) for the separation streamline, whence

$$\psi(\xi,\eta_p) = 1 = 3\eta_p^2 - 2\eta_p^3 + (\eta_p^2 - 2\eta_p^3 + \eta_p^4)F_1 + (2\eta_p^2 - 3\eta_p^3 + \eta_p^5)F_2 \qquad \text{(A-6)}$$

where $\eta_p = \eta_p(\xi)$. The relationship between the derivatives of F_1, F_2, and η_p are found by differentiating Equation (A-6) with respect to ξ, giving

$$\eta_p^I = -\frac{(\eta_p - 2\eta_p^2 + \eta_p^3)F_1^I + (2\eta_p - 3\eta_p^2 + \eta_p^4)F_2^I}{6(1-\eta_p) + 6(1-3\eta_p+2\eta_p^2)} \qquad \text{(A-7)}$$

When a primary vortex exists the separation streamline must leave the upper surface at the inlet corner which requires that the slope of the separation streamline be less than zero, i.e.

$$\eta_p^I(1) < 0; \quad \eta_p(1) = 1 \qquad \text{(A-8-a)}$$

which is satisfied, according to Equation (A-7), when

$$F_1^I(1) + 3F_2^I(1) > 0 \qquad \text{(A-8-b)}$$

If only one free parameter is used Equation (A-8-b) reduces to

$$F^{I}(l) > 0 \qquad \text{(A-8-c)}$$

This condition is necessary and sufficient to establish the existence of a primary vortex.

APPENDIX IV

NOMENCLATURE

The following symbology is used in this appendix and is distinct from that used elsewhere in this thesis in most cases.

Roman

a	position of upstream source, A, in ζ - plane
c	position of downstream sink, C, in ζ - plane
A,B,C, D,E,F	significant mapping points in Figure A-2
G	dimensionless stagnation point velocity gradient
h_o	upstream channel width
h_1	downstream channel width
q	fluid velocity
Q	log of complex conjugate velocity
U_o	upstream velocity
U_1	downstream velocity
V	velocity along surface BC_{oo} in Figure A-2-a
v	dimensionless velocity along surface BC_{oo} in Figure A-2-a, V/U_1
x	horizontal physical coordinate
y	vertical physical coordinate
y	dimensionless vertical physical coordinate, y/h_o
z	complex physical coordinate, $x+iy$

Greek

ζ	complex half-plane mapping function, $\xi + i\eta$

η	imaginary part, complex half-plane mapping function
θ	inclination of streamline
ξ	real part, complex half-plane mapping function
σ	ratio of downstream area to upstream area, h_1/h_o
v	complex conjugate velocity
ϕ	potential function
ψ	stream function
ω	complex potential function, $\phi+i\psi$

APPENDIX IV

INVICID FLOW IN A TWO-DIMENSIONAL ENCLOSED CORNER

It has been seen that the flow in the stagnation region of a radial diffuser can not be treated analytically. A qualitative idea of the nature of the flow can be realized by analyzing the invicid flow in the stagnation region of the two-dimensional confined corner of unit depth shown in Figure A-2-a. It consists of a channel of width h_o perpendicular to a channel of width h_1. The flow is uniform at A_{oo} and C_{oo} having a magnitude of U_o and U_1, respectively. This configuration can be considered as half of the flow in a T-shaped slot obtained by reflecting Figure A-2-a about the x-axis. A stagnation point occurs at the origin of coordinates.

The invicid flow field is determined using a conformal mapping scheme involving the three planes shown in Figures A-2-b, A-2-c, and A-2-d. Setting the stream function, Ψ, to zero on $C_{oo}DA_{oo}$ and to Uh on $A_{oo}B\ C_{oo}$, the complex potential, $\omega = \phi + i\Psi$, is mapped onto the upper half of the ζ- plane using the Schwarz-Christofel transformation (34)

$$\frac{d\omega}{d\zeta} = -\frac{Uh}{\pi}\left(\frac{1}{\zeta+a} - \frac{1}{\zeta-c}\right) \qquad \text{(A-9)}$$

Next, the conjugate velocity

$$\nu = u - iv = qe^{i\theta} = -\frac{d\omega}{dz} \qquad \text{(A-10)}$$

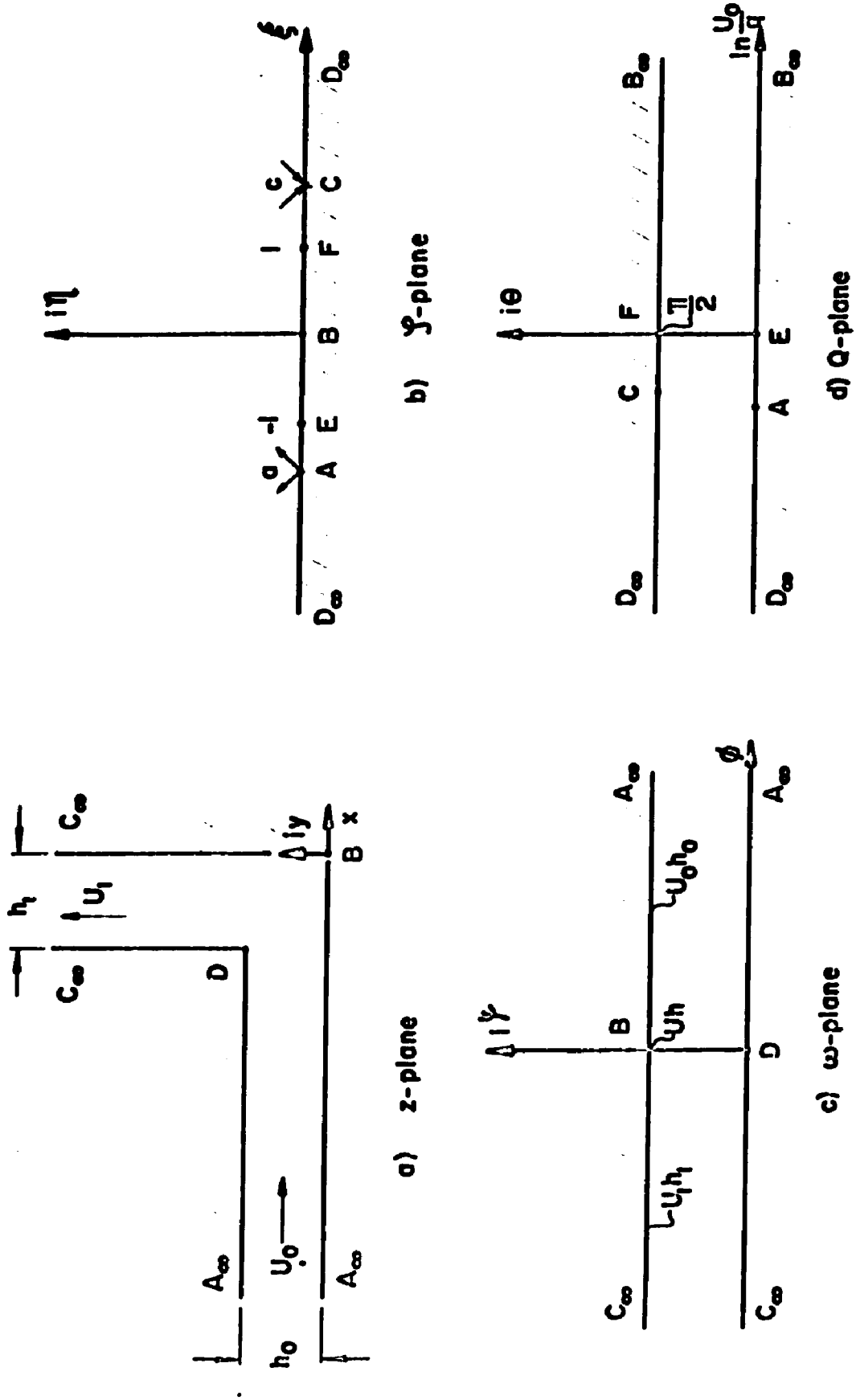


Figure A-2. Physical and Conformal Mapping Planes.

is transformed onto the upper half of the ζ - plane in terms of the log conjugate velocity

$$Q = \ln \frac{U_0}{\nu} = \ln \frac{U_0}{q} + i\theta \qquad \text{(A-11)}$$

using the Schwarz-Christofel transformation

$$\frac{dQ}{d\zeta} = \frac{Const.}{\zeta} \qquad \text{(A-12)}$$

subject to the conditions $Q=0$ at E and $Q=i\frac{\pi}{2}$ at F. The solution of Equation (A-12) gives the conjugate velocity as

$$\nu = -iU_0 \zeta^{\frac{1}{2}} \qquad \text{(A-13)}$$

Dividing Equation (A-9) by Equation (A-13) gives

$$\frac{dz}{d\zeta} = i\frac{h_0}{\pi}\zeta^{-\frac{1}{2}}\left(\frac{1}{\zeta-a} - \frac{1}{\zeta-c}\right) \qquad \text{(A-14)}$$

subject to the condition $\zeta=0$ at B. Evaluating Equation (A-13) at A and B gives the constants a and c as 1 and $(h_0/h_1)^2$, respectively. The solution of Equation (A-14) gives the complex position as

$$\frac{z}{h_0} = i\frac{2}{\pi}\left(\sigma \tanh^{-1}\sigma\zeta^{\frac{1}{2}} + \tan^{-1}\zeta^{\frac{1}{2}}\right) \qquad \text{(A-15)}$$

where $\sigma = h_1/h_0$ is the ratio of the exit area to the inlet area.

Equations (A-13) and (A-15) represent the conjugate velocity and complex position transformed to the upper half of the ζ - plane. The velocity along the surface BC_{oo} in the stagnation region is, in dimensionless terms,

$$\gamma = \frac{v}{U_1} = \sigma\xi^{\frac{1}{2}} \qquad \text{(A-16)}$$

The corresponding dimensionless position is

$$\gamma = \frac{x}{K_0} = \frac{2}{\pi}(\sigma \tanh^{-1}\sigma\xi^{\frac{1}{2}} + \tan^{-1}\xi^{\frac{1}{2}}) \qquad \text{(A-17)}$$

The stagnation surface velocity distribution from Equations (A-16) and (A-17) are shown in Figure A-3 as a function of σ.

The dimensionless stagnation point velocity gradient is

$$G = \frac{d\gamma}{d\psi} = \frac{\pi}{2}/(\sigma + \sigma^{-1}) \qquad \text{(A-18)}$$

and is shown in Figure A-4 as a function of σ.

The ratio G/σ is required to calculate the stagnation point heat transfer rate and is, from Equation (A-18),

$$\frac{G}{\sigma} = \frac{\pi}{2}/(\sigma^2 + 1) \qquad \text{(A-19)}$$

and is shown in Figure A-5 as a function of σ.

The free stream velocity distribution along the lower surface in the stagnation region is shown in Figure A-3 as calculated from Equations (A-16) and (A-17) for different area ratios. The area ratio exerts a strong influence: for $\sigma \geq 1$ the velocity decelerates from the stagnation point, while for $\sigma < 1$ the velocity accelerates to $\xi = (\sigma^{-2}+1)/2$ and decelerates thereafter. The maximum velocity gradient occurs near $\psi = 1$ for small area ratios. The velocity distribution is linear only near the stagnation point, i.e., $\psi \leq .15$. The maximum stagnation point velocity gradient occurs for $\sigma = 1$ in Figure A-4 and has a value less than unity. The ratio G/σ asymptotically approaches a value of $\frac{\pi}{2}$ in Figure A-5 as $\sigma \to 0$.

The observations of the preceding paragraph, while for a two-dimensional stagnation flow, should be qualitatively correct for

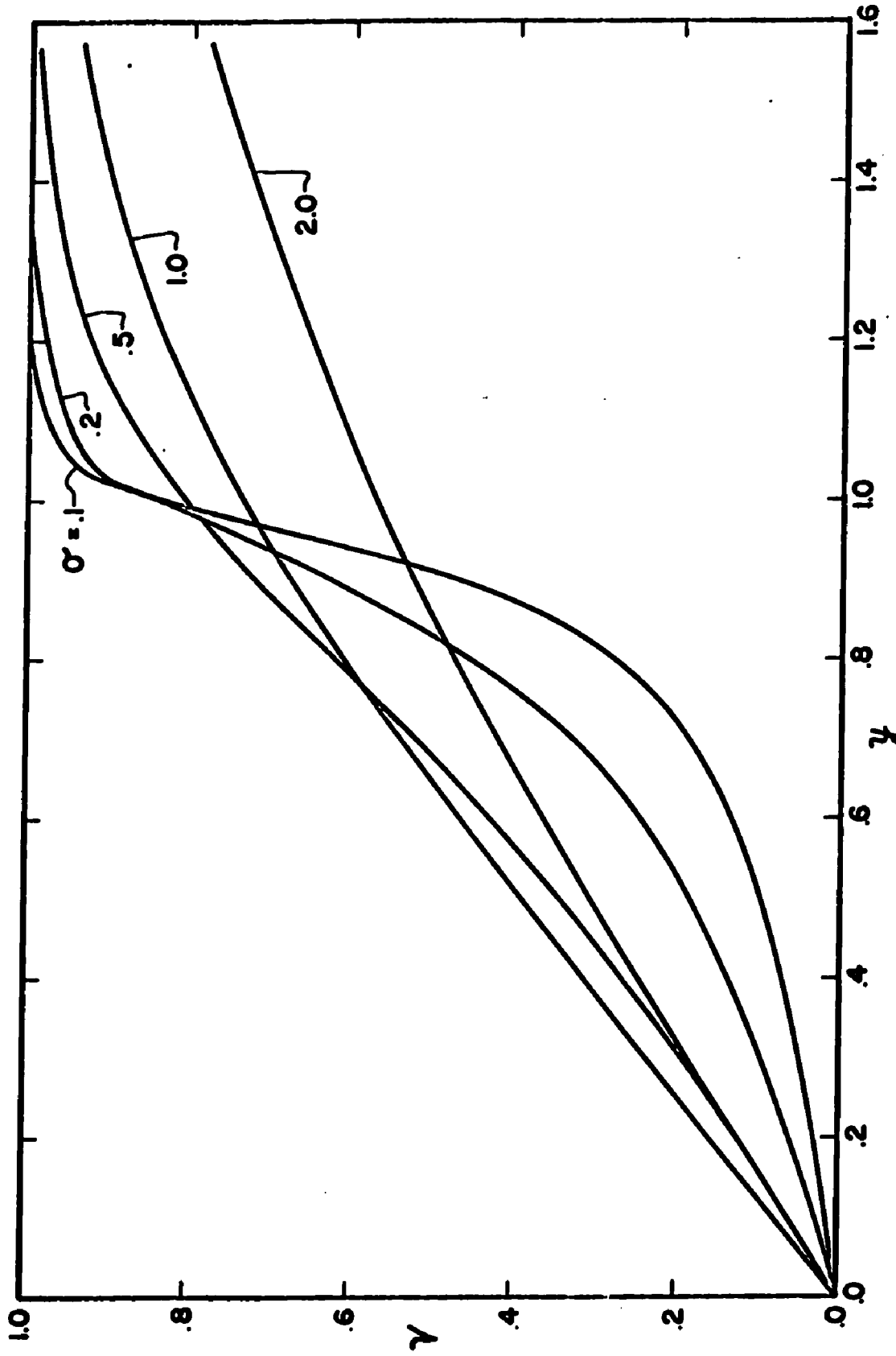


Figure A-3. Free Stream Velocity Distribution in Stagnation Region.

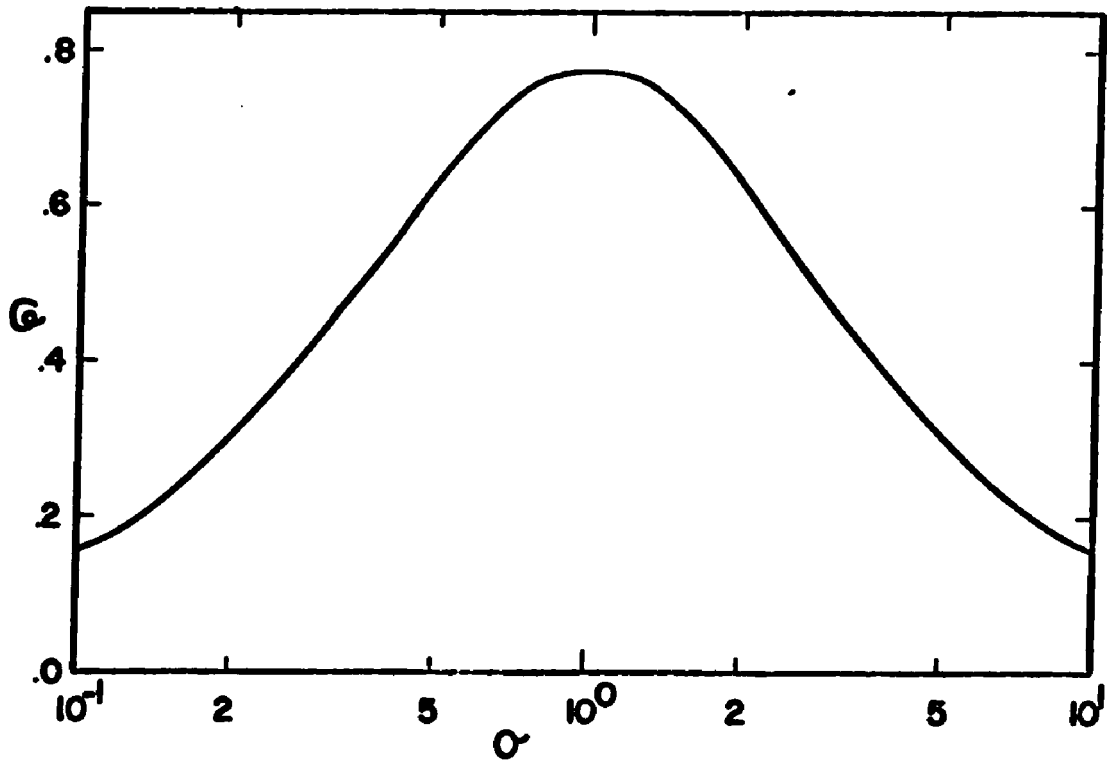


Figure A-4. Stagnation Point Velocity Gradient vs Area Ratio.

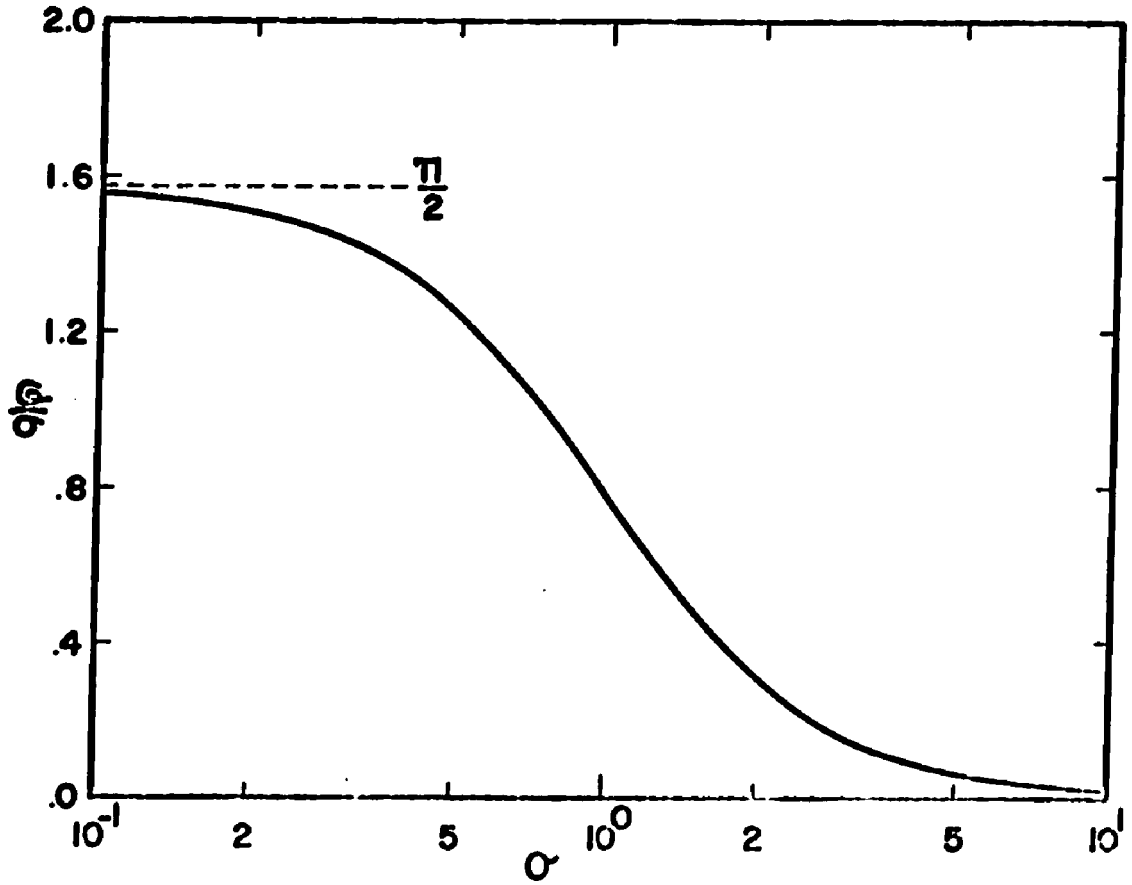


Figure A-5. Ratio G/σ vs Area Ratio.

the stagnation flow in a radial diffuser. The velocity distribution for $\sigma = .2$ in Figure A-3 agrees well with the theoretical results of Parmet and Saibel [39] for a radial diffuser under similar conditions, i.e. same area ratio and uniform inlet and exit velocity profiles. The effect of separation at the inlet corner has been analyzed by Strand [46] for a two-dimensional jet. The free stream velocity distribution in the stagnation region is strongly affected when the area ratio becomes less than 2.

BIBLIOGRAPHY

1. Akfirat, J.C. "Transfer of Heat from an Isothermal Flat Plate to a Two-Dimensional Wall Jet." Proceedings of Third International Heat Transfer Conference, Chicago, August, 1966.

2. Andreeva, E.A. "Calculation of Static Characteristics of "Nozzle-Baffle" Elements." Automation and Remote Control, 21, No. 7 (1960), 691-700. (Translation from Automatika i Telemekhanika).

3. Benenson, D. and Bott, J.F. "2-Dimensional Laminar Boundary Layer Flow Within a Radial Diffuser." ASME-61-WA-193, 1961.

4. Blankenship, V.D. "The Influence of Transverse Harmonic Oscillations on the Heat Transfer from Finite and Infinite Vertical Plates in Free Convection." Ph.D. Thesis, The University of Michigan, 1962.

5. Chen, C. and Peube, J.L. "Sur l' écoulement Radial Divergent d'un Fluide Visqueux Incompressible Entre Deux Parallel Plans." L'Academie des Sciences, Paris, Comptes Rendus, 258, No. 22 (1964), 5353-5355.

6. Chen, C. "Contribution à l'étude Experimentale de l'écoulement Radial d'un Fluide Visqueux Incompressible Entre Deux Disques Paralleles." J. de Mécanique, 5, No. 2 (June 1966), 245-259.

7. Comolet, M.R. "Nombre de Reynolds Critique d'un Ecoulement Visqueux, Radial Divergent Entre Deux Plans Parallèles." L'Academie des Sciences, Paris, Comptes Rendus, 244, No. 7 (1957), 849-852.

8. Constantinescu, V.N. Discussion of Mori [37], J. Basic Eng., 85, No. 2 (1963), 309-310.

9. Doebelin, E.O. Measurement Systems: Application and Design. McGraw-Hill, 1966.

10. Elkouh, A.F. "Inertia Effect in Radial Flow." Int. J. Mech. Sci., 9 (May 1967), 253-255.

11. Finlayson, B.A. and Scriven, L.E. "The Method of Weighted Residuals and Its Relation to Certain Variational Principles for Analysis of Transport Processes." Chem. Eng. Science, 20 (1965), 395-404.

12. Finlayson, B.A. and Scriven, L.E. "The Method of Weighted Residuals - A Review." Appl. Mech. Reviews, 19, No. 9 (1966), 735-748.

13. Gardon, R. "A Transducer for the Measurement of Heat Flow Rate." J. of Heat Transfer, Trans. ASME, Series C, 82 (1960), 396-398.

14. Gebhart, B. Heat Transfer. McGraw-Hill, 1961.

15. Geiger, D., Fara, H.D., and Street, N. "Steady Radial Flow Between Parallel Plates." J. of Appl. Mech., 31, No. 2 (1964), 354-355.

16. Giedt, W.H. "Investigation of Variation of Point Unit - Heat - Transfer Coefficient Around a Circular Cylinder Normal to an Air Stream." Trans. ASME, 71 (1949).

17. Hagiwara, T. "Studies on the Characteristics of Radial-Flow Nozzles. (First Report, Theoretical Analysis of Outward Flow)." Bul. JSME, 5, No. 20 (1962), 656-663.

18. Hagiwara, T. "Studies on the Characteristics of Radial-Flow Nozzles (Third Report, Experimental Results)." Ibid, 668-675.

19. Hunt, J.B. and Torbe, I. "Characteristics of a Hydrostatic Thrust Bearing." Int. J. of Mech. Sci., 4 (1962), 503-516.

20. Ishizawa, S. "The Axi-Symmetric Laminar Flow in an Arbitrarily Shaped Narrow Gap (1st Report, Theoretical Analysis for the Inlet Region)." Bul. JSME, 8, No. 31 (1965), 353-367.

21. Ishizawa, S. "The Axi-Symmetric Laminar Flow in an Arbitrarily Shaped Narrow Gap (2nd Report, Theoretical Analysis for the Downstream Region)." Bul. JSME, 9, No. 33 (1966), 86-103.

22. Jackson, J.D. "Laminar Radial Flow Between Parallel Plates." - Discussion of Savage [42], J. Appl. Mech., 32, No. 3 (1965), 715-716.

23. Jackson, J.D. and Symmons, G.R. "An Investigation of Laminar Radial Flow Between Two Parallel Discs." Appl. Sci. Res., Sect. A, 15 (1965), 59-75.

24. Jackson, J.D. and Symmons, G.R. "Pressure Distribution in Hydrostatic Thrust Bearings." Int. J. Mech. Sci., 7, No. 4 (1965), 239-42.

25. Knudsen, J.G. and Katz, D.L. Fluid Dynamics and Heat Transfer. McGraw-Hill, 1958.

26. Kreith, F. "Transfert de Chaleur dans un Ecoulement Radial Divergent d'un Fluide Visqueux Incompressible Entre Deux Plans Parallèles." L'Academie des Sciences, Paris, Comptes Rendus, 260 (1965), 62-65.

27. Kreith, F. "Reverse Transition in Radial Source Flow Between Two Parallel Planes." Phys. of Fluids, 6, No. 6 (1965), 1189-90.

28. Kreith, F. "Transfert de Chaler et de Masse Dans un Ecoulement Radial Entre Deux Disques Parallèles Fixes on Tournant à la Meme Vitesse." Int. J. Heat Mass Trans., 9 (1966) 265-282.

29. Kreyszig, E. Advanced Engineering Mathematics. Wiley, 1962.

30. Livesey, J.L. "Inertia Effects in Viscous Flows." Int. J. Mech. Sci., 1 (1960), 84-88.

31. McAdams, W.H. Heat Transmission. McGraw-Hill, 1954.

32. McGinn, J.H. "An Experimental Study of Radial Flow Between Parallel Plates." Ph.D. Thesis, Lehigh University, 1952.

33. McGinn, J.H. "Observations on the Radial Flow of Water Between Fixed Parallel Plates." Appl. Sci. Res., Sect. A, 5 (1955), 255-264.

34. Milne-Thompson, L. Theoretical Hydrodynamics. Macmillan, 1960.

35. Moller, P.S. "Radial Flow Without Swirl Between Parallel Discs." Aero. Quart., 14 (1963), 163-186.

36. Morgan, P.G. and Saunders, A. "An Experimental Investigation of Inertia Effects in Viscous Flow." Int. J. Mech. Sci., 2, Nos. 1 and 2 (1960), 8-12.

37. Mori, H. "A Theory of an Externally Pressurized Circular Thrust Gas Bearing With Consideration of the Effects of Lubricant Inertia." J. Basic Engin., 85, No. 2 (1963), 304-310.

38. Parmet, I.L. and Saibel, E. "The Flow of Perfect and Viscous Fluids in a Radial Diffuser." ZAMM, 45, No. 6 (1965), 409-418.

39. Parmet, I.L. and Saibel, E. "Flow and Boundary Layer Development in a Radial Diffuser." Mécanique Appliqué, 11, No. 2 (1966), 275-284.

40. Peube, J.L. "Sur l'écoulement Radial Permanent d'un Fluide Visqueux Incompressible Entre Deux Plans Parallèles Fixes." J. Mécanique, 2, No. 4 (1963), 377-395.

41. Robertson, J.M. Hydrodynamics in Theory and Application. Prentice-Hall, 1965.

42. Savage, S.B. "Laminar Radial Flow Between Parallel Plates." J. Appl. Mech., 31 (1964), 594-596.

43. Schlichting, H. Boundary Layer Theory. McGraw-Hill, 1960.

44. Senecal, V.E. and Rothfus, R.R. "Transition Flow of Fluids in Smooth Tubes." Chem. Eng. Prog., 49, No. 10 (Oct. 1953), 533-538.

45. Sherba, M. "Flow Separation: Visualization in a Radial Diffuser." ME 490 Project, Mechanical Engineering Department, The University of Michigan, 1968.

46. Strand, T. "Invicid-Incompressible-Flow Theory of Static Two-Dimensional Solid Jets in Proximity to the Ground." J. Aerospace Sci., 29, No. 2 (1962), 170-173, 184.

47. Takenaka, T., Yamane, R., and Iwamizu, T. "Thrust of the Disc Valves." Bul. JSME, 7, No. 27 (1964), 558-566.

48. Thomas, R.A. and Cobble, M.H. "Radial Flow Heat Transfer." J. Heat Trans., 85 (1963), 189-191.

49. Woolard, H.W. "A Theoretical Analysis of the Viscous Flow in a Narrowly Spaced Radial Diffuser." J. Appl. Mech., 24 (1957), 9-15 and 644-646.